National Library of Canada
Ottawa, Canada
K1A 0N4

Bibliothèque nationale
du Canada

32

TC – 66165

ISBN 0-315-18256-3

CANADIAN THESES ON MICROFICHE SERVICE – SERVICE DES THÈSES CANADIENNES SUR MICROFICHE

PERMISION TO MICROFILM – AUTORISATION DE MICROFILMER

• Please print or type – Écrire en lettres moulées ou dactylographier

AUTHOR – AUTEUR

Full Name of Author – Nom complet de l'auteur: Christopher Joseph Peters

Date of Birth – Date de naissance: April 23, 1954

Canadian Citizen – Citoyen canadien: ☒ Yes / Oui ☐ No / Non

Country of Birth – Lieu de naissance: Canada

Permanent Address – Résidence fixe:
44 Glen Road, Apt. 70
Hamilton, Ontario.
L8S 4N2

THESIS – THÈSE

Title of Thesis – Titre de la thèse: Physical Adsoprtion of Simple Linear Moelcules on Graphite

Degree for which thesis was presented / Grade pour lequel cette thèse fut présentée: Ph.D.

Year this degree conferred / Année d'obtention de ce grade: 1985

University – Université: McMaster

Name of Supervisor – Nom du directeur de thèse: Dr. J.A. Morrison

AUTHORIZATION – AUTORISATION

Permission is hereby granted to the NATIONAL LIBRARY OF CANADA to **microfilm** this thesis and to **lend** or **sell copies of the film.**

The author reserves other publication rights, and neither the thesis nor extensive extracts from it may be printed or otherwise reproduced without the author's written permission.

L'autorisation est, par la présente, accordée à la BIBLIOTHÈQUE NATIONALE DU CANADA de **microfilmer** cette thèse et de **prêter** ou de **vendre des exemplaires du film.**

L'auteur se réserve les autres droits de publication; ni la thèse ni de longs extraits de celle-ci ne doivent être imprimés ou autrement reproduits sans l'autorisation écrite de l'auteur.

ATTACH FORM TO THESIS – VEUILLEZ JOINDRE CE FORMULAIRE À LA THÈSE

Signature: Chris Peters

Date: February 12, 1985.

NL-91 (r. 84/03)

Canada

PHYSICAL ADSORPTION
OF SIMPLE LINEAR MOLECULES ON GRAPHITE

By

Christopher Joseph Peters, B.Sc., M.Sc.

A Thesis
Submitted to the School of Graduate Studies
in Partial Fulfilment of the Requirements
for the Degree
Doctor of Philosophy

McMaster University
© (November 1984)

PHYSICAL ADSORPTION ON GRAPHITE

DOCTOR OF PHILOSOPHY (1984)

McMASTER UNIVERSITY
Hamilton, Ontario

TITLE: Physical Adsorption of Simple Linear Molecules on Graphite

AUTHOR: Christopher Joseph Peters, B.Sc. (McGill University)
M.Sc. (Queen's University)

SUPERVISOR: Professor J.A. Morrison

NUMBER OF PAGES: xii, 136

ABSTRACT

Some properties of the small linear molecules N_2, CO and C_2H_2, physically adsorbed on a graphite surface, are investigated in experiments and computer simulations.

Acetylene, physically adsorbed on graphite, is known to have two solid phases, but no clear indication of liquid-gas and liquid-solid coexistence has been observed. Vapour pressure isotherms of C_2H_2 on exfoliated graphite are measured revealing the two solid phases and also both coexistence phases.

At high temperatures Henry's Law constants of C_2H_2 and CO on graphite are measured and used to refine the parameters of potential models. For CO, it is found that a 10-4 model is easily fit to the data, but in the case of C_2H_2 no realistic parameters in a 10-4 model resulted in an acceptable fit. A qualitative explanation, invoking an image force, is offered but quantitative attempts fail as the large quadrupole moment of C_2H_2 causes the model for the image interaction to break down.

Monte Carlo calculations of the two solid structures are presented which disagree with the proposals in the literature but are in agreement with diffraction data.

X-ray and LEED studies of monolayer densities of CO and N_2 adsorbed on graphite have revealed the low temperature structure to be a $1\times\sqrt{3}$ herringbone and to change to an incommensurate herringbone

structure at slightly greater densities. Orientational order-disorder transitions occur at both densities but the character of the transitions is different in N_2 than in CO.

Classical Monte Carlo calculations of the integral heat of adsorption vs. coverage are presented for several potential models and are compared to experimental measurements. The best of these models are used in Monte Carlo simulations of the orientational order-disorder transition in N_2 and CO. The results for N_2 compare well with experiment but in the case of CO the agreement is not as good as the potential model seems to correspond to a molecule which is too small.

ACKNOWLEDGEMENTS

I would like to thank Dr. J.A. Morrison for demonstrating to me the scientific approach to research and for his assistance in the experimental aspects of this work.

I would also like to express my appreciation to Dr. M.L. Klein for his assistance in the simulations and for sharing his knowledge of intermolecular potentials and physical adsorption.

But perhaps the most important assistance was that offered to me by Kerstin Stockman. She put up with my antics and her presence filled in most of the depressions. She also typed and corrected what was known as the final version of this thesis.

for my father

TABLE OF CONTENTS

Page

DESCRIPTIVE NOTE ii

ABSTRACT iii

ACKNOWLEDGEMENTS v

CHAPTER 1 - INTRODUCTION 1

CHAPTER 2 - EXPERIMENTAL 12

2.1 Materials 12

2.2 Pressure Measurement 13

2.3 Sample Cell 13

2.4 Temperature Measurement and Control 16

2.5 Graphite Sample 18

2.6 Gas Sample 20

2.7 Measurement of Relevant Volume and Gas Quantities 20

2.8 Cryogenics 21

2.9 Typical Procedure 21

CHAPTER 3 - RESULTS I 23

3.1 Low Temperature Isotherms 23

3.2 Absolute Area 27

3.3 Isotherm at High Temperature 35

Page

3.4 Low Density Isotherms 35

3.5 Carbon Monoxide Isotherms 44

CHAPTER 4 - INTRODUCTION TO INTERMOLECULAR POTENTIALS 48

4.1 Ab Initio Calculations 48

4.2 Additivity 54

4.3 Molecule Surface Interaction 58

4.4 N_2 Models 61

4.5 Hydrocarbon Models 64

4.6 Acetylene Model 66

4.7 Carbon Monoxide Models 69

4.8 Molecule-Surface Interactions 73

CHAPTER 5 - RESULTS II 76

5.1 Monte Carlo Methods and Techniques 76

5.2 Size Effects 78

5.3 Surface Effects 78

5.4 Interaction Range 78

5.5 Sampling 79

5.6 Methods 80

5.7 Henry's Law Constants 80

5.8 The Solid Phases of Adsorbed Acetylene 86

5.9 Low Density Solid 87

5.10 High Density Solid 94

5.11 Integral Heats of Adsorption 101

5.12 Orientation Order-Disorder Transition in N_2 and CO 106

Page

CHAPTER 6 - SUMMARY AND CONCLUSIONS 130

REFERENCES 132

LIST OF TABLES

Page

1.1 Properties of C_2H_2, CO, N_2. 7

4.1 Atom-Atom Nitrogen Potential Models 63

4.2 Atom-Atom Acetylene Potential Models 67

4.3 Atom-Atom Carbon Monoxide Potential Models 71

4.4 Atom-Atom Molecule/Graphite 6-12 Parameters 75

5.1 Henry's Law Constants and Isosteric Heat of Adsorption 83

5.2 Fitted Values of 10-4 Parameters 84

5.3 Neutron Diffraction Data 88

5.4 Low Density Structural Fits to the Neutron Data 96

5.5 High Density Structural Fits to the Neutron Data 99

LIST OF FIGURES

		Page
1.1A	The phase diagram for a film of spherical molecules adsorbed on graphite	3
1.1B	The $1\times\sqrt{3}$ structure	3
1.2	A sketch of a typical series of isotherms for spherical molecules adsorbed on graphite	4
2.1	A diagram of the isotherm apparatus	14
2.2	A sketch of a piece of Grafoil	19
3.1	Isotherms of C_2H_2/graphite between 109 K and 122 K	24
3.2	Isotherms of C_2H_2/graphite between 117 K and 160 K	25
3.3	Isotherm of Xe/graphite at 111 K	29
3.4	Previously proposed solid structures of C_2H_2/graphite	31
3.5	Isotherms of C_2H_2/graphite beyond 1 monolayer	33
3.6	Isotherms of C_2H_2/graphite between 117 K and 130 K	36
3.7	Isotherms of C_2H_2/graphite between 135 K and 183 K	37
3.8	Isotherms of C_2H_2/graphite at low coverages	38
3.9	Isosteric heat of adsorption vs. coverage for C_2H_2/graphite	39
3.10	Isosteric heat of adsorption vs. coverage for CO/graphite	41
3.11	Henry's Law constant vs. temperature for C_2H_2/graphite	43
3.12	Isotherms for CO/graphite between 58 K and 64 K	45
3.13	Phase diagram for CO/graphite	46
3.14	Henry's Law constants vs. temperature for CO/graphite	47

		Page
4.1	The 6-12 potential form	53
4.2	The geometry for the substrate screened interaction	57
5.1	The unit consisting of 4 molecules which was replicated to form a solid cluster	81
5.2	A snapshot of a low density C_2H_2/graphite simulation	89
5.3	A snapshot of a low density C_2H_2/graphite simulation	90
5.4	A snapshot of a low density C_2H_2/graphite simulation	92
5.5	A snapshot of a low density C_2H_2/graphite simulation	93
5.6	The P_{2gg} unit cell	95
5.7	A snapshot of a high density C_2H_2/graphite simulation	98
5.8	The calculated and experimental integral heats of adsorption vs. coverage for CO/graphite	103
5.9	The calculated and experimental integral heats of adsorption vs. coverage for N_2/graphite	104
5.10	The commensurate $1x\sqrt{3}$ herringbone structure for N_2/graphite at 10 K	108
5.11	X-ray scattering data for the commensurate phases of CO and N_2 adsorbed on graphite	110
5.12	X-ray scattering data for the incommensurate phases of CO and N_2 adsorbed on graphite	111
5.13	An incommensurate pinwheel structure	113
5.14	The results of the simulation of the orientational order-disorder transition in the commensurate phase of N_2/graphite	116
5.15	The results of the simulation of the orientational order-disorder transition in the incommensurate phase of N_2/graphite	118
5.16	A snapshot of the simulated structure of incommensurate N_2/graphite	120

Page

5.17 A snapshot of the simulated structure of commensurate CO in a glass-like state 123

5.18 The results of the simulation of the orientational order-disorder transition in the commensurate phase of CO/graphite 124

5.19 The results of the simulation of the orientational order-disorder transition in the incommensurate phase of CO/graphite 126

CHAPTER I

INTRODUCTION

Current research on physical adsorption has recently been concentrated in two areas: two dimensional matter and interaction potentials.

The relative mean square displacements of the adsorbed molecules in a direction normal to the surface is often sufficiently small so that the film can be considered as pseudo-two dimensional (2D). These 2D films exhibit all of the phases found in three dimensional (3D) matter: gas, liquid, solid and hypercritical fluid. Phase transitions in lower dimensional systems (< 3) have been extensively studied theoretically and adsorbed films provide systems in which to test some of the theories. With regard to the surface there is a possible complication. The ideal surface for such a study would be perfect, flat and continuous, providing only a retaining field. This ideal surface does not exist; as all surfaces are composed of atoms and will contain imperfections also.

The most studied systems have been the rare gases (1,2) on a graphite surface. The interaction between rare gases is, to a good approximation, spherically symmetric, which greatly simplifies the theoretical analysis. The basal plane of graphite is easily cleaned and, in an exfoliated form, offers a large, reasonably homogeneous surface. A sketch of a typical phase diagram for a rare gas adsorbed on graphite is shown in Figure 1.1A. The molecules form two kinds of adsorbed solids, labelled "commensurate" and "incommensurate" in the phase diagram. By "commensurate" one means that the adsorbed solid has at least one reciprocal lattice vector in common with the substrate. The basal plane of graphite has a simple hexagonal structure and, for many adsorbed molecules including CH_4, Xe and Kr, the commensurate structure is known as the $1x\sqrt{3}$ triangular lattice depicted in Figure 1.1B. CH_4 and Kr molecules are of such a size that their close packed arrangement is almost a $1x\sqrt{3}$ commensurate lattice. The Xe molecule is larger and pressure must be applied to produce a commensurate layer.

Phase diagrams, such as Figure 1.1A, are pieced together from a variety of experiments. A vapour pressure isotherm is often the first experiment performed on a new system. An isotherm is a plot of the surface density of adsorbed molecules vs. the pressure of the gas exposed to the surface at a constant temperature. In favourable cases, it is possible to obtain a phase diagram from a series of isotherms. A sketch of such results is shown in Figure 1.2. The shaded regions represent the different phases. The boundaries are drawn with consideration of the fact that a vertical segment is an indication of two surface phases coexisting with the vapour or gas phase.

Proof

Systems in thermodynamic equilibrium have equal chemical potentials. In this case, there are 3 phases: 2 surface phases and the gas phase in equilibrium at a temperature T. This implies:

Figure 1.1A. Typical phase diagram for a film of spherical molecules adsorbed on a graphite surface.

Figure 1.1B. Diagram of the $1\times\sqrt{3}$ structure for a spherical molecule adsorbed on a graphite surface. The dashed rectangular box represents the P_{2gg} unit cell. The lengths of the unit cell vector are in the ratio $1:\sqrt{3}$.

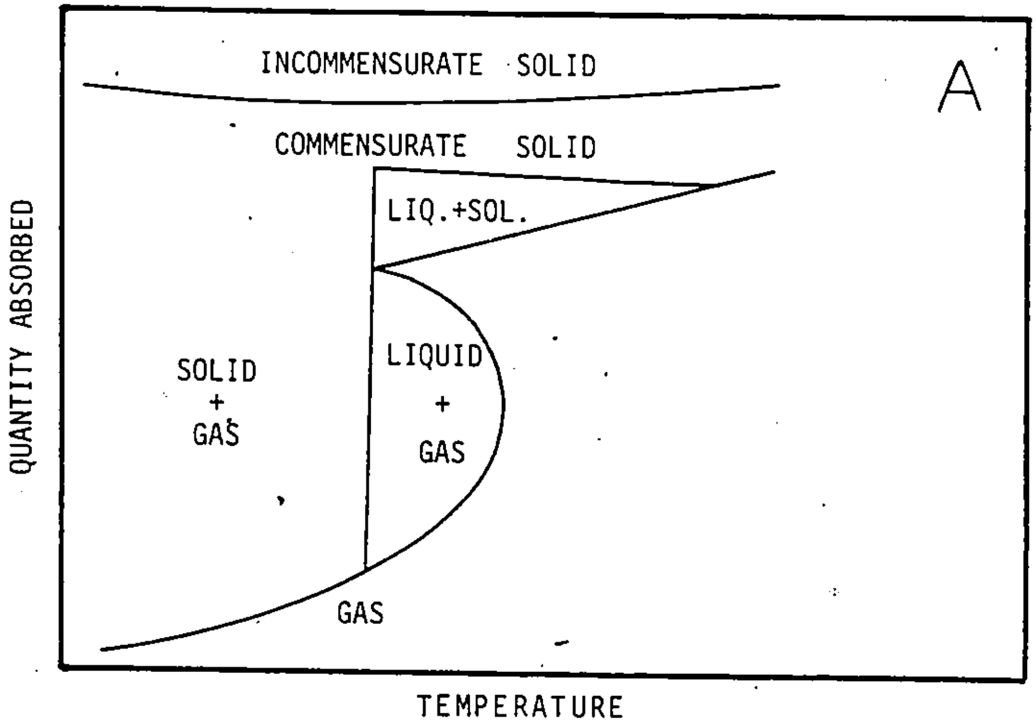
INCOMMENSURATE SOLID
COMMENSURATE SOLID
LIQ.+SOL.
LIQUID + GAS
SOLID + GAS
GAS
A
QUANTITY ABSORBED
TEMPERATURE

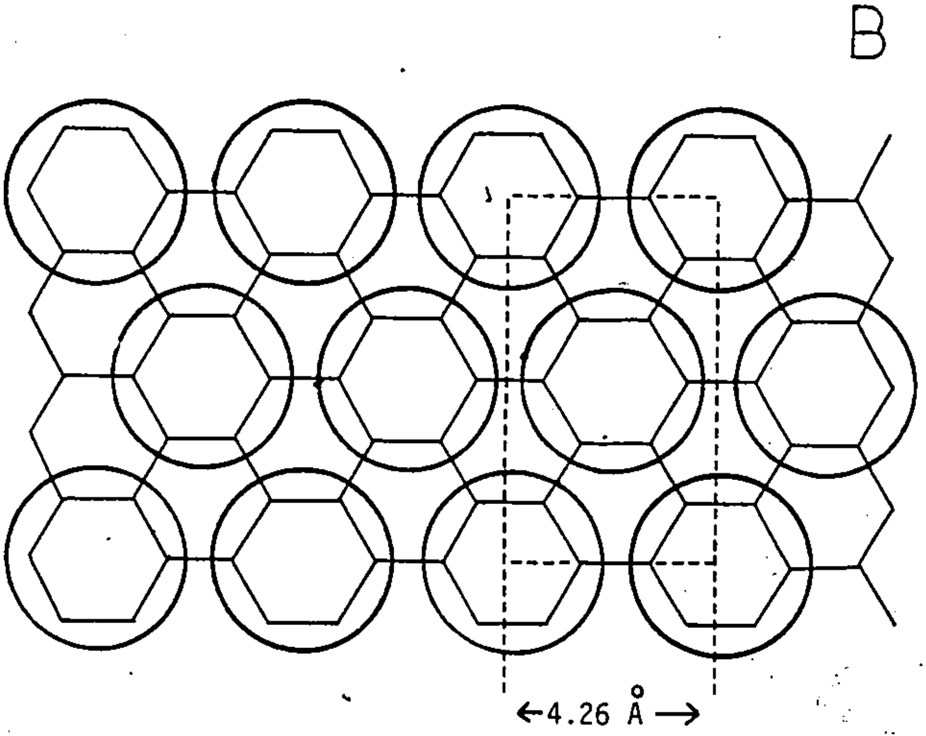
B
4.26 Å

Figure 1.2. A sketch of a typical series of isotherms for spherical molecules adsorbed on a graphite surface. Also shown are the phase boundaries.

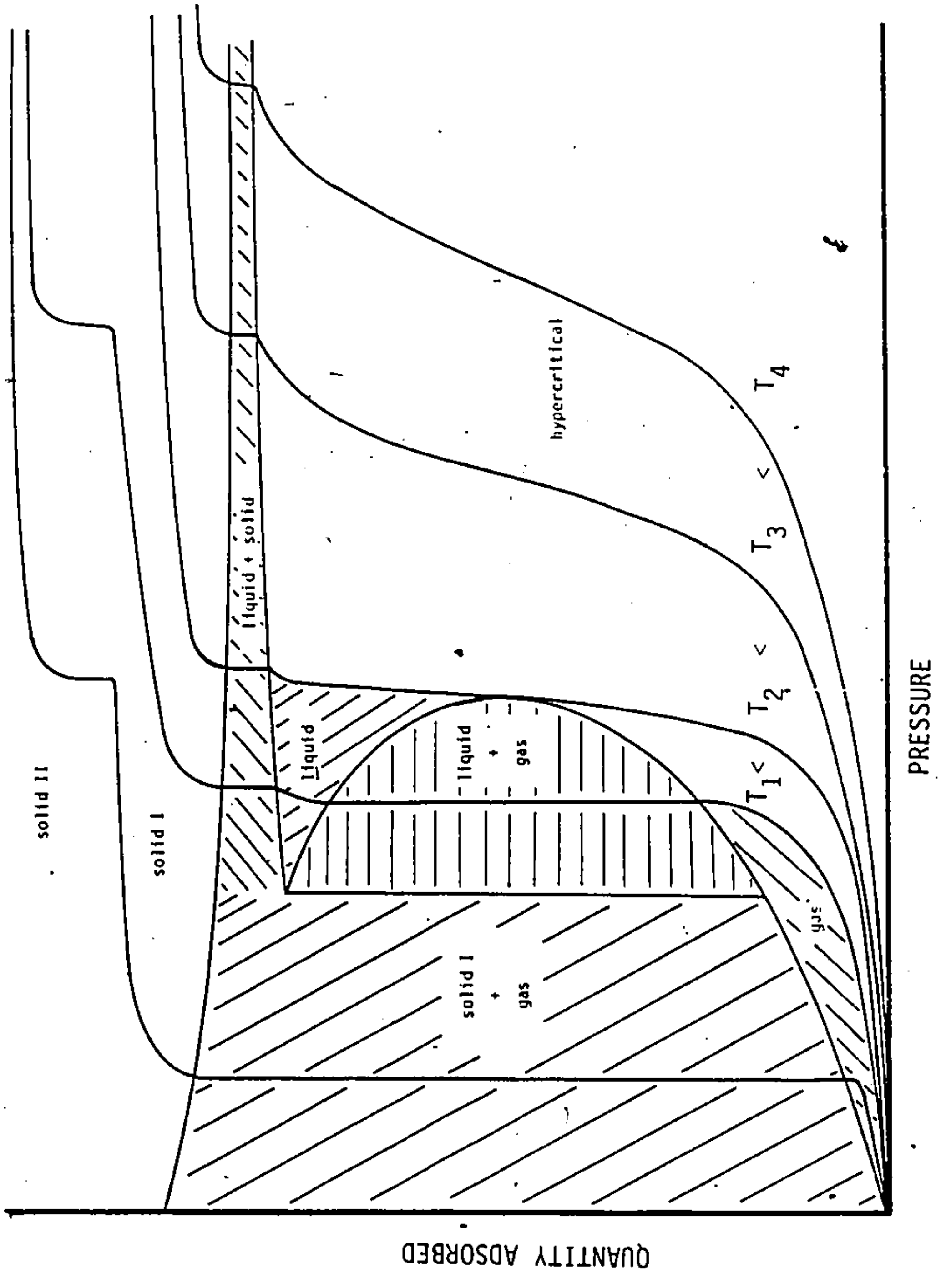
QUANTITY ADSORBED
PRESSURE
solid II
solid I
liquid + solid
liquid
liquid + gas
solid I + gas
gas
hypercritical
$T_1 < T_2 < T_3 < T_4$

$$\mu_{s1}(T,\phi,P) = \mu_{s2}(T,\phi,P) = \mu_g(T,P), \qquad (1.1)$$

where the subscripts refer to the surface phases (s1, s2) and the ideal gas phase (g), ϕ is the 2D pressure, P is the gas pressure which is a measured quantity.

From eq. (1.1), two of the three variables (ϕ,P) can be eliminated leaving only:

$$\mu_{s1}(T) = \mu_{s2}(T) = \mu_g(T), \qquad (1.2)$$

so that the chemical potential is independent of the number of particles. For an ideal gas, the chemical potential depends only on the temperature, which is externally fixed and therefore the pressure is independent of the number of particles.

Scattering experiments with x-rays, neutrons, and electrons (LEED) can often yield useful results in the study of both the statics and dynamics of adsorbed films. A difficulty with the first two techniques is that the scattering cross sections are often very small thus requiring long runs or high flux machines (synchrotron or scintillation sources) to obtain adequate sensitivity and accuracy. LEED examines only one layer and is not subject to the same difficulty. However, LEED data are much more difficult to analyse.

Thus far, only spherical or nearly spherical molecules have been discussed. Linear molecules are potentially more interesting but more difficult to study theoretically. The approximation of 2D matter is not as good here because the molecules can tilt from the surface. The interactions between adsorbed linear molecules are also anisotropic and this introduces orientational structure within the centre of mass lattice. For example, adsorbed N_2 has a commensurate $1\times\sqrt{3}$ centre of mass lattice with a herringbone orientational structure. The orientational structure has its own order-disorder transition which may be different from the centre of mass transitions.

Theoretical endeavours to understand the behaviour of adsorbed linear molecules has been hampered by insufficient knowledge of the molecule-molecule and molecule-surface interaction potentials. Up to the present the vast majority of the effort on intermolecular potentials has been concerned with 3D phases. These potentials are often assumed to be transferrable to the adsorbed systems.

In adsorption studies, the molecule-surface interactions are as important as molecule-molecule interactions. The behaviour of a single molecule on a surface is difficult to study experimentally. A series of isotherms in the limit of zero coverage can be used to obtain the average energy of adsorption and the phase space available to the molecule. These quantities are calculable and can be used to refine potential models. Molecular beam scattering can also be used to study the interaction potential but, this method is limited to very simple systems such as Helium or Hydrogen.

This thesis is concerned with the physical adsorption of the linear molecules N_2, CO, and C_2H_2 on graphite. Attention is focussed on the orientational order and the interaction potentials. The remainder of this introduction will outline some relevant facts about these three molecules both in 3D and adsorbed on graphite. Many properties are listed in Table 1.1.

Table 1.1

Properties of C_2H_2, CO, N_2

	C_2H_2	CO	N_2
Molecular Properties			
Nuclear separations (Å)	C-C = 1.203(2) C-H = 1.059	1.128(3)	1.098(4)
Mass (amu)	26	28	28
Electric multipole moments (eÅ)			
dipole	0(5)	-0.089(6)	0
quadrupole	1.53	-0.420	-0.29(7)
octopole	0	0.577	0
hexadecapole	4.54	-0.751	-0.58(8)
Lennard-Jones Parameters (9)			
ε(K)	185	110	91.5
σ(Å)	4.22	3.59	3.68
3D Structural Properties			
Low temperature structure lattice constants	Acam(10) a = 6.193 b = 6.005 c = 5.551	P213(11) a = 5.646	Pa3(12) a = 5.644
High temperature structure lattice constants (Å)	Pa3(12) a = 6.091	P63 a = 4.140 b = 6.723	P63 a = 4.050 b = 6.604
Transition temperature (K)	133(10)	61.55(14)	35.61(4)
Triple point (K)	192.5(2)	68.01(14)	63.15(4)
Critical point (K)	308.2	132.9	126.2

Acetylene has a large static quadrupole moment which should lead to strong orientational order in the 2D film. Bulk C_2H_2 undergoes a structural phase transition at 133 K from an orthorhombic to a cubic structure. The cubic structure is common to many linear molecules in which the quadrupole interaction is important such as N_2, CO, and H_2. Attempts to develop an intermolecular potential for acetylene have concentrated on fitting the sublimation energies and lattice dynamics of both solid structures simultaneously. It has proved difficult to stabilize the orthorhombic phase over the cubic phase at low temperature. A few C_2H_2-C_2H_2 potentials have been proposed (15,16,17) but only one model has been partially successful in fitting these properties. Lattice dynamics and cohesive energies do not uniquely determine a potential as they sample only a few relative distances and orientations of the molecules. For non-bonded interactions, the concept of a general potential should be reasonable, but if bonds are important, the mathematical description of the interactions becomes much more complicated. In the orthorhombic phase, the molecules in the "ab" plane form a 'tee' structure with a nearest C-H distance of only 2.73 Å, which is somewhat smaller than that in other hydrocarbon solids. Recent SCF calculations (18) have shown that there is the possibility of a weak hydrogen bond stabilizing the T-shape for the dimer.

There have been only three sets of experiments on the C_2H_2/graphite system. The first was a gas chromatography (84) experiment. This was an indirect measurement of the limiting slope of an isotherm and was used to calculate energy of adsorption. The second was a series of isotherm measurements (19) which indicated the possibility of two solid structures. The third was a neutron scattering (20) study of C_2D_2/graphite which verified the existence of two different solid structures. The latter two research groups proposed structures which will be shown later to be not the most likely based on the current knowledge of C_2H_2-C_2H_2 intermolecular potentials.

There has been less work done on the molecule-surface interaction and it is therefore not as well understood. For instance it is only recently that the effects of two molecule-surface forces have been tested (substrate mediated and image forces), although they have been known theoretically for some time. In part, the delay in understanding is due to the lack of experimental data. Part of this thesis will be concerned with describing experimental and theoretical evidence for the image forces and their effect on the C_2H_2-graphite potential.

A series of isotherm experiments and classical Monte Carlo calculations was performed to test and refine the molecule-surface and molecule-molecule interaction potentials and to determine the nature of the two solid structures of C_2H_2 on graphite.

Nitrogen adsorption is the most studied of all of the systems of linear molecules on graphite. In 3D, much effort has gone into acquiring an understanding of the intermolecular potential and considerable success has been achieved. Potentials have been developed which describe reasonably the statics and dynamics of the bulk solid and which have been recently applied to the adsorbing system.

Carbon monoxide is isoelectronic with nitrogen. The two molecules have many properties in common such as size, mass, quadrupole moment and 3D solid structure (Table 1.1). The 3D structure of both is fcc with the molecules oriented along the four <111> directions. Both solids undergo a phase transition to a hcp structure in which the molecules rotate freely. It has long been known that the orientational order of nitrogen is dominated by the quadrupole-quadrupole interaction. The quadrupole moment of CO is 40% larger than that of N_2. Since the energy varies as the square of the quadrupole moment, one would expect the orientational order-disorder transition temperature to be in a ratio of $1.4^2 = 1.96$. This simple scaling is close to being obeyed as:

$$\frac{T_c(CO)}{T_c(N_2)} = \frac{61.55}{35.61} = 1.73.$$

The difference between the two molecules lies in the charge and mass asymmetry of carbon monoxide. CO has an octopole and a small dipole moment, whereas N_2 has no odd multipoles. The dipole moment could, in principle, lead to a head to tail ordering in the solid phase. Calorimetric measurements down to 0.8 K (21) have shown the Pa3 solid to have considerable orientational disorder. Recent NQR measurements (22) have shown this solid to be in a metastable state with reorientational times $\sim 5.0\text{x}10^{13}$ hrs. at 10 K. It appears that the octupole and dipole moments are not sufficiently strong to create a completely ordered state at low temperatures, because the disordered state freezes in.

Given these similarities in 3D one might expect to observe similar behaviour when the molecules are adsorbed on graphite. Recent x-ray (23) and LEED (24) experiments have shown this not to be the case, particularly with respect to the orientational order-disorder transition.

To help to understand the similarities and differences between N_2 and CO adsorbed on graphite, Monte Carlo calculations of N_2 and CO were performed. The results of the simulations compared favourably with those from experiments for N_2. Such close agreement was not achieved for CO adsorption.

The outline of the thesis is as follows: the isotherm experiments are described in Chapter 2 and the results and analysis in Chapter 3. A more detailed discussion of intermolecular potentials is presented in Chapter 4. A brief description of Monte Carlo methods and the results of the classical Monte Carlo simulations on C_2H_2, CO and N_2 are analysed in Chapter 5.

CHAPTER 2

EXPERIMENTAL

The measurement of an adsorption isotherm is conceptually a simple experiment. A substrate is placed in a cell of known volume and measured quantities of gas are added to the cell. Some (amount depending on the temperature) is adsorbed onto the surface leaving a number of molecules in the gas phase; the pressure in the cell is measured. An isotherm is a plot of the amount of gas adsorbed against the pressure in the cell at constant temperature.

Isotherms of carbon monoxide and acetylene were measured in a temperature range from 58 K to 185 K. A detailed description of the apparatus and a typical procedure follows.

2.1 Materials

Acetylene is a hazardous substance. It reacts with aluminum, mercury, copper and silver - with the latter three to form explosive acetylide compounds. The metals with high thermal conductivity, copper and aluminum, could not be used in the construction of the adsorption apparatus. It was necessary to bake out the gas handling system, but high temperature silver solder could not be used. Therefore, the entire gas handling system and sample cell were constructed of stainless steel tubing, welded joints and bellows valves. Some other parts of the system, e.g., for the gas supply, were made of glass with greased stopcocks. A diagram of the entire gas handling system and sample cell is shown in Figure (2.1).

The tubing was 1/4" O.D. stainless steel except for a piece of 3/16" O.D. cupronickel which extended from the top of the Dewar to approximately 8" above the cell. Alloys of less than 60% copper, such as cupronickel and brass, are safe to use because acetylide formation is confined to the first layer.

2.2 Pressure Measurement

Pressures between 1.2 and 300 Torr were measured with a Texas Instruments spiral quartz gauge (TI gauge) with an accuracy of .02 Torr. This gauge was calibrated by the manufacturer and again by the author against a mercury manometer to an accuracy of ± 0.5%. At pressures up to 1.2 Torr the gauge was calibrated against a Baratron capacitance manometer which had a precision of 1.0×10^{-4} Torr. The TI gauge was primarily used for the measurement of the quantity of gas added to the cell. Only a few adsorption equilibrium pressures were measured with it.

The majority of the data was taken with a MKS Baratron capacitance manometer, calibrated by the manufacturer to a precision of 1×10^{-4} Torr. Its range was from 1.0×10^{-4} to 1.2 Torr, with a digital output in units of 1.0×10^{-4} Torr. There was a zero drift of $\sim 1.0\times10^{-4}$ Torr/day. Thus, the zero was checked and adjusted periodically - occasionally after every measurement.

2.3 Sample Cell

The cell was designed to help reduce the effects of thermal

Figure 2.1. A diagram of the cryostat, sample cell and gas handling system.

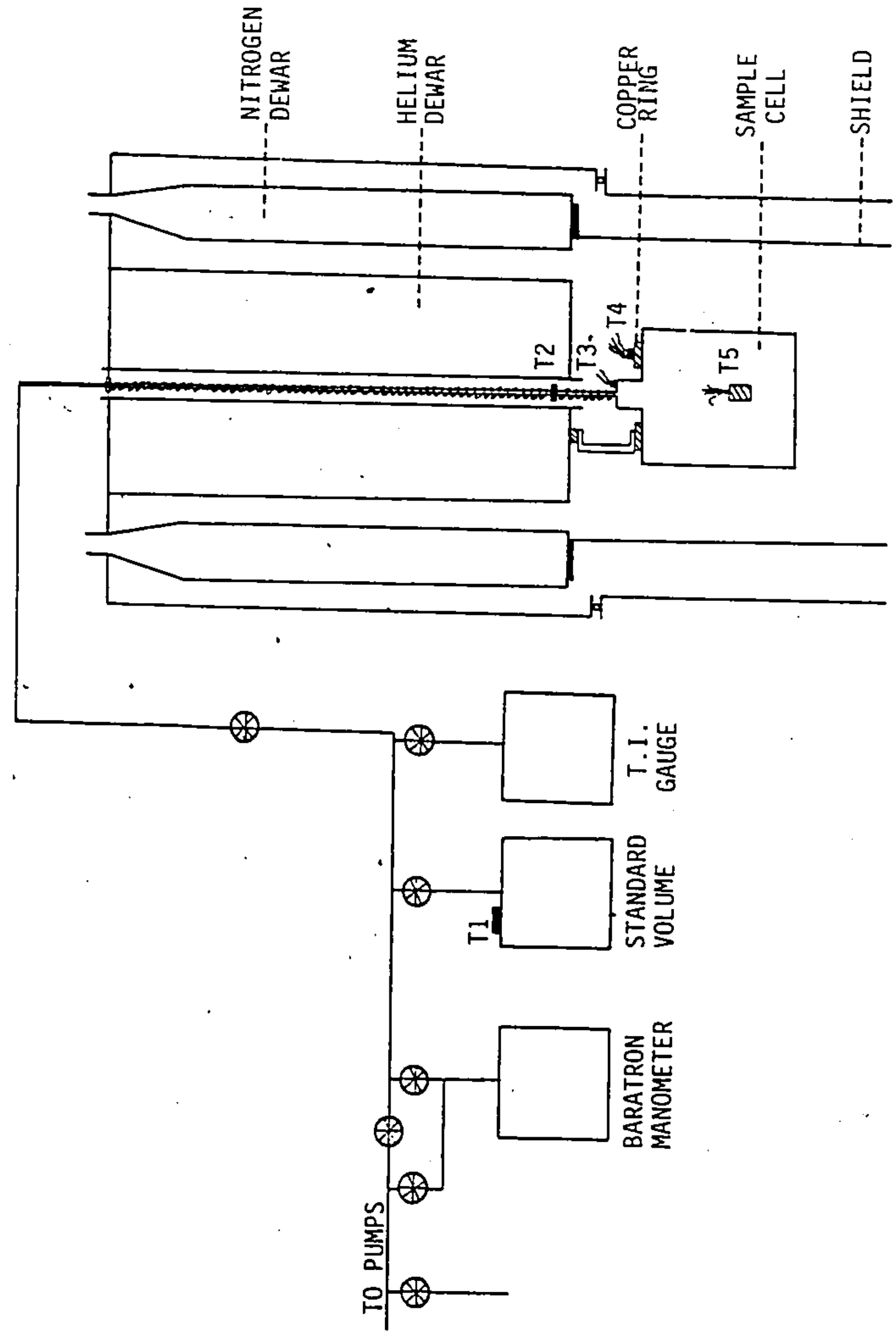
NITROGEN DEWAR
HELIUM DEWAR
COPPER RING
SAMPLE CELL
SHIELD
T2
T3
T4
T5
T.I. GAUGE
STANDARD VOLUME
T1
BARATRON MANOMETER
TO PUMPS

transpiration. Thermal transpiration is a non-equilibrium steady state effect whereby a pressure gradient will exist in a tube along which there is a temperature gradient. The size of the effect for a particular gas depends on the tube diameter, the mean free path of the gas molecules, and the temperatures of the ends of the tube. Thermal transpiration has been measured for many gases including C_2H_2 (25) and CO (26) and the results fitted to the equations:

$$\frac{P_1}{P_2} - 1 = \left[\sqrt{\frac{T_1}{T_2}} - 1\right]\frac{1}{(A\cdot x^2+B\cdot x+1)} \qquad (2.1)$$

for C_2H_2 where $A = 1.6\text{x}10^8$, $B = 3.9\text{x}10^4$, $C = 0.9$, $T = (T_1+T_2)/2$, $x = P_2 dT^{-(.5+C)}$, d = tube diameter

and $$\frac{P_1}{P_2} - 1 = \left[\sqrt{\frac{T_1}{T_2}} - 1\right]\frac{1}{(A\cdot x^2+B\cdot x+C\sqrt{x}+1)} \qquad (2.2)$$

for CO where $A = 10\text{x}10^5$, $B = 2000$, $C = 8$, $T = (T_1+T_2)/2$, $X = P_2d/T$, d = tube diameter

in units of Torr, millimeters and Kelvin. For both equations P_2 is the measured pressure and P_1 is the actual pressure.

The Baratron pressure gauge and the sample are at different temperatures, see Figure 2.1. The larger the tube diameter at a constant temperature gradient the smaller are the thermomolecular pressure effects.

To reduce the effects, one should ensure that the temperature gradient occurs in the tube with the largest diameter. In the present system, this was the 3/4" O.D. tube which extended 1½" above the cell. The top of the tube was kept at as high a temperature as possible through the following procedure. The tube extending through the liquid He^4

Dewar was wrapped with heater wire, then many layers of superinsulation and maintained at room temperature. Another heater was used between the joint in the cupronickel tube (pt. T4 in Figure 2.1, where the first heater stopped) and the top of the 3/4" O.D. tube (pt. T3 in Figure 2.1) to keep the temperature there as high as possible and still to be able to control the temperature of the cell.

2.4 Temperature Measurement and Control

The temperature of the system was monitored at 5 positions which are shown in Figure (2.1) as T1 through T5. Five different thermometers were employed. These will be described in order from the lowest to highest temperatures.

At the low end, there was a calibrated platinum resistance thermometer, about 1 mm in diameter and 1/2" long (Lake Shore Cryotronics (Pt-103)). It was greased (APIEZON N) and placed in a hole drilled into a piece of brass which was silver soldered to the side of the sample cell (pt. T1 in Figure 2.1). The platinum thermometer monitored the temperature of the graphite sample.

The temperature was controlled with a Lake Shore Cryotronics temperature controller (DTC-500) (T2 in Figure 2.1). The diode was attached with G.E. Glyptal varnish to a 1 cm thick copper ring which was fastened to the top of the cell with Wood's metal. The temperature of the diode could be controlled to ± ∿1 mK with a heater wound around the copper link extending between the ring and the bottom of the helium Dewar. Changes in the cooling rate were made by altering the dimensions of the copper link.

The third sensor was 10 K ½ Watt carbon resistor that was attached to the top of the 3/4" O.D. diameter tube with Glyptal (pt. T3 in Figure 2.1). It was calibrated against the silicon diode between 300 K and 77 K and was used only for the purpose of calculating thermal transpiration corrections.

The fourth sensor was a copper-constantan differential thermocouple extending between the joint in the sample line (pt. T4 in Figure 2.1) and a position near the platinum thermometer. It was used to ensure that the sample line was maintained at a chosen temperature: room temperature in the case of the experiments with C_2H_2.

The fifth thermometer was a mercury in glass thermometer placed on the calibrated volume (pt. T5 in Figure 2.1). Knowledge of this temperature was necessary for calculating both the thermal transpiration correction and the quantity of gas added to the cell.

Although the temperature at the silicon diode could be controlled very well (± 1 mK), the poor conductivity of stainless steel meant that the control at the platinum thermometer was only approximately ± 50 mK, but this was much better than what was required.

An irreproducible temperature gradient of up to 1 K existed between the silicon diode and platinum thermometers. Fortunately, variations in the magnitude of the gradient had no effect on the reproducibility of the data. The gradient was most probably between the copper ring and the top portion of the cell and did not extend down to the Grafoil sample, the top of which was about 3/4" below the top of the cell.

2.5 Graphite Sample

The substrate was a commercial exfoliated graphite known as Grafoil (type GTA, Union Carbide).

Exfoliation is typically done by intercalating graphite with a substance such as $FeCl_3$ and heating it quickly to approximately 2000°C. This blows the structure apart and increases the specific surface dramatically. The $FeCl_3$ is then pumped away and the remaining sponge-like material is compressed and rolled flat. The resulting substance is sketched in Figure 2.2. The graphite sheets are broken into platelets of well correlated graphite approximately 110 Å in dimension, as revealed by x-ray diffraction. The full width at half maximum of the distribution of tilt angles from parallel is 27°. Some of the graphite platelets are separated by large gaps into which the gas can diffuse. The adsorption surface available in Grafoil is approximately 22 m^2/g.

A rectangular sample of Grafoil was scored with parallel lines, 1-2 mm apart, on both sides to aid the diffusion of gas into the structure. The treatment was unlikely to cause significant damage to the platelets. The total surface area of the sample was estimated to be 770 m^2. The details of the area determination will be described later. The sample was rolled up gently to fit into the cell. The top was then welded on under vacuum.

The cell containing the Grafoil sample was soldered into the system and baked out under vacuum to remove surface impurities. The temperature was raised to 600°C over a period of two days and held there for 12 hrs., after which the pressure was steady at 2×10^{-6} Torr.

Figure 2.2. Sketch of a piece of grafoil. The small circles represent adsorbed molecules.

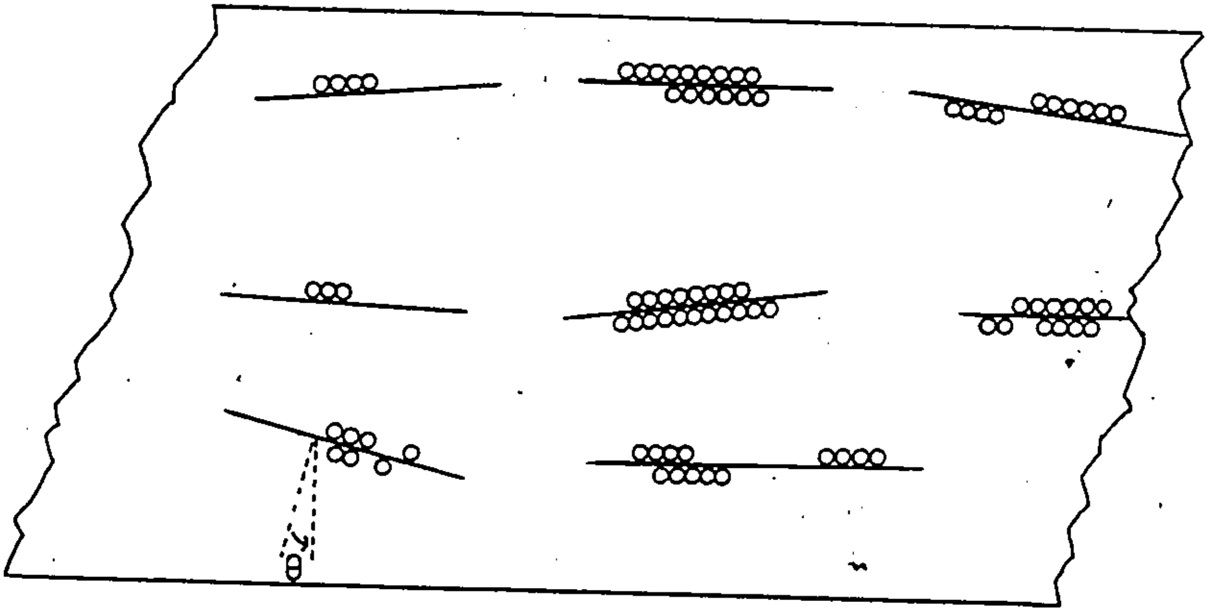
θ

2.6 Gas Sample

The two gases used in the experiments, carbon monoxide (CO) and acetylene (C_2H_2), were obtained from Matheson Co. The acetylene was 99.8% pure, the major impurities being N_2 and O_2. The other impurities, Cl_2 and phosphine, accounted for a maximum of .01%. To remove the O_2 and N_2, the gas specimen was condensed into a glass trap at 77 K and the volatile gases pumped away with a diffusion pump. The procedure was repeated several times. Finally, the gas was condensed slowly into the trap, held at a temperature only slightly below the triple point (191 K), to form a clear solid and then pumped on for a short time (∿ 2 min.). It will be evident from the adsorption data obtained at the lowest temperature (109 K) that the purification procedure was effective.

The carbon monoxide gas was of research purity (99.99%) with the stated impurities: hydrogen (∿ 2 ppm), N_2 (∿ 21 ppm), O_2 (∿ 1 ppm), CH_4 (3.8 ppm), CO_2 (21 ppm). However, during the first experiments, it became apparent that the analysis could not be correct as an appreciable amount of the gas would not adsorb on the graphite at 60 K. The impurity (probably H_2) was removed by alternate adsorption and pumping of the gas over the graphite at 50 K until the apparent vapour pressure was constant.

2.7 Measurement of Relevant Volumes and Gas Quantities

The volumes of the parts of the adsorbing system were calibrated by expansion of helium gas from a known volume. The volumes were measured to an accuracy of ± 0.1%.

The amount of gas added to the cell was measured in the dead space of the TI gauge and associated connecting tubing. Deviations from the ideal gas law were estimated to be ± 0.2% for C_2H_2 and ± .05% for CO up to the highest pressure used (∿ 250 Torr).

The quantity which remained in the gas phase at equilibrium was subtracted from the amount added to the cell to obtain the quantity of gas adsorbed. The unadsorbed gas was in the sample cell and the lines leading directly back to the Baratron gauge. Since the equilibrium pressures were always low, the ideal gas law could be used throughout.

2.8 Cryogenics

A basic Oxford Instruments (MD4A) cryostat with liquid nitrogen in both the helium and nitrogen containers was used to obtain temperatures greater than 80 K. At lower temperatures, approximately 1 litre of liquid nitrogen was added to the helium container and pumped on with a mechanical pump. The lowest temperature that could be achieved in this way was approximately 50 K, but since heat had to be supplied to the filling line to prevent condensation, the lowest temperature that could be maintained during an experiment was 58 K.

2.9 Typical Procedure

Gas from the storage volume was admitted to the TI gauge and the quantity calculated. The valves connecting the TI gauge to the cell were opened slowly and the gas allowed to flow into the cell. The valve to the TI gauge was then closed and the Baratron gauge opened to the cell while the system came to equilibrium. Equilibration times ranged from 15 min. to 2 hours depending upon the temperature and state of the film. At a given temperature, the time constant was longest when the monolayer was near completion and shortest at low densities when the film was in a 2D gas phase. These times increased at lower temperature. When it was thought the system had reached equilibrium, the pressure was recorded and the zero of the gauge checked. The amount of gas not adsorbed and the thermal transpiration corrections were then applied. From time tq time, the system was left for 12 more hours to check that equilibrium had indeed been achieved.

CHAPTER 3

RESULTS I

3.1 Low Temperature Isotherms for Acetylene

The isotherms obtained at the lowest temperatures are plotted in Figure 3.1. The dashed curves are estimates of phase boundaries based on these adsorption data alone. Finite size effects, due to substrate inhomogeneity, may be expected to cause the vertical regions of the isotherms to have finite slopes, but changes in slope can still be used to indicate changes in the state of the film. There are eight distinct regions in the phase diagram, five of which were reported previously by Menaucourt et al (19); 2D gas, 2D gas-solid, 2D solid I, 2D solid II, and hypercritical regions. The new features found here are the clear indications of the 2D gas-liquid, 2D liquid-solid and 2D liquid regions which are marked by vertical segments in the isotherms. From these results, we can place the critical point at approximately 121 K and the triple point at approximately 117 K.

The isotherms reported by Menaucourt et al (Figure 3.2) did not yield evidence for liquid-solid or gas-liquid coexistence. The critical temeprature was placed at approximately 155 K (34° higher than this work), as deduced from the temperature dependence of the quantity:

Figure 3.1. Isotherms for acetylene obtained at T = 109.47 K, 114.10 K, 117.84 K, 119.00 K, 119.43 K, 120.85 K, 122.70 K. The dashed lines represent phase boundaries.

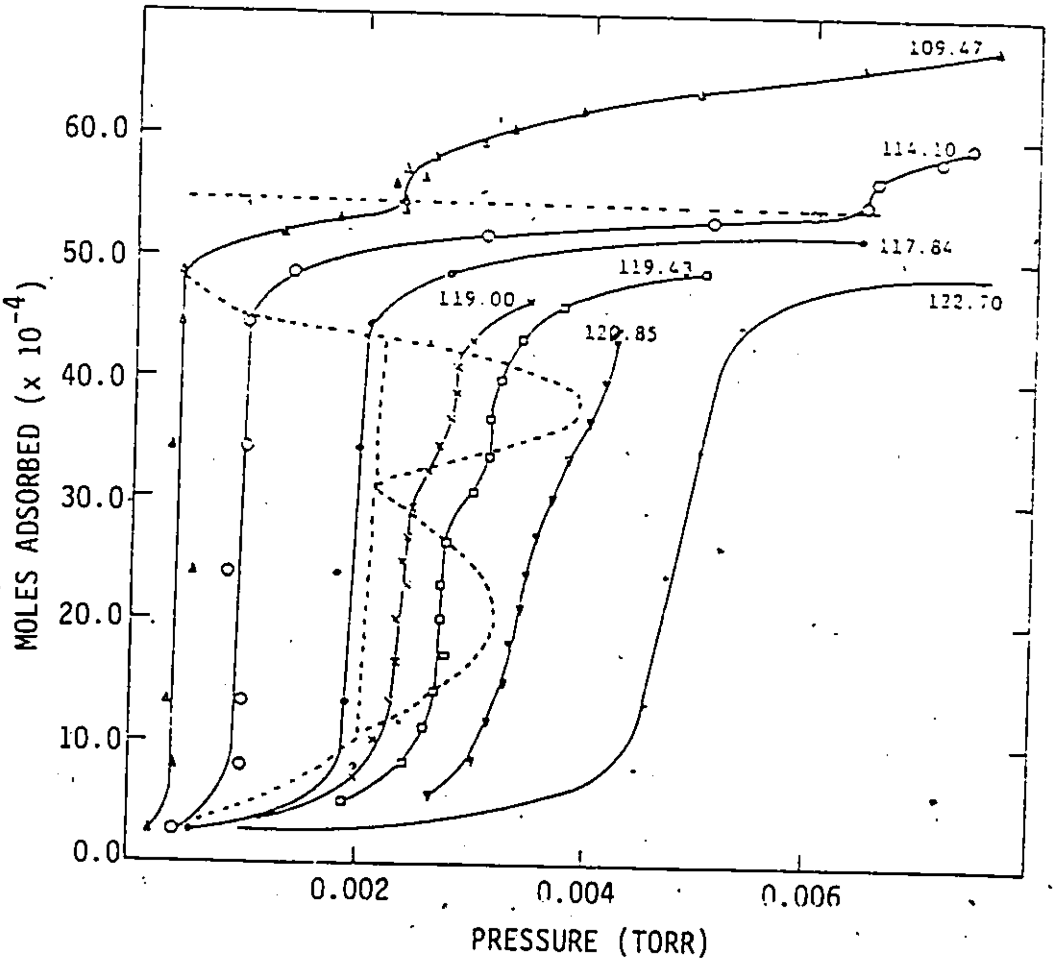
109.47
114.10
117.84
119.43
119.00
120.85
122.70
60.0
50.0
40.0
30.0
20.0
10.0
0.0
MOLES ADSORBED (x 10^{-4})
0.002
0.004
0.006
PRESSURE (TORR)

Figure 3.2A. Isotherms obtained by Menaucourt (19) at temperatures of (1) 117.84 K, (2) 122.65 K, (3) 130.58 K, (4) 138.83 K.

Figure 3.2B. Isotherms obtained by Menaucourt (19) at temperatures of (1) 149.7 K, (2) 150.75, (3) 152.73 K, (4) 154.75 K, (5) 155.72 K, (6) 156.75 K, (7) 157.75 K, (8) 158.76 K, (9) 159.74 K.

Figure 3.2C. Isotherms obtained by Menaucourt (19) at high coverage and T = 114.16 K. Figure taken from ref. (19).

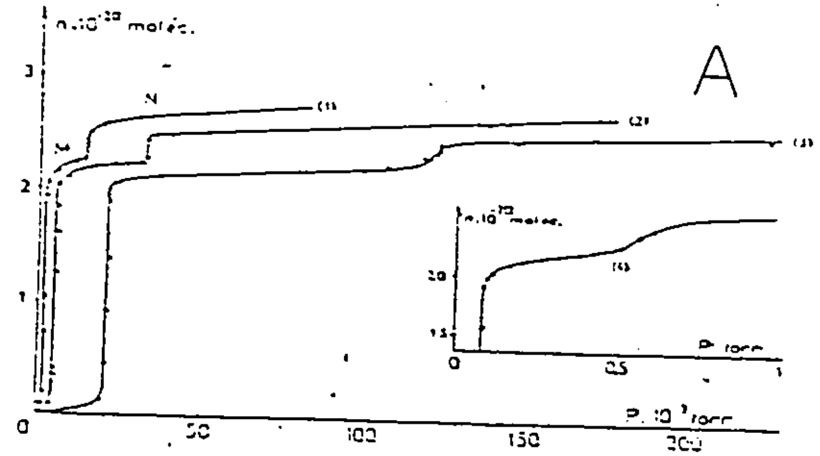
A
n.10^{-20} moléc.
3
2
1
0
M
N
(1)
(2)
(3)
50
100
150
200
P.10^{3} torr
n.10^{-20} moléc.
2.0
1.5
(4)
0
0.5
1
P torr

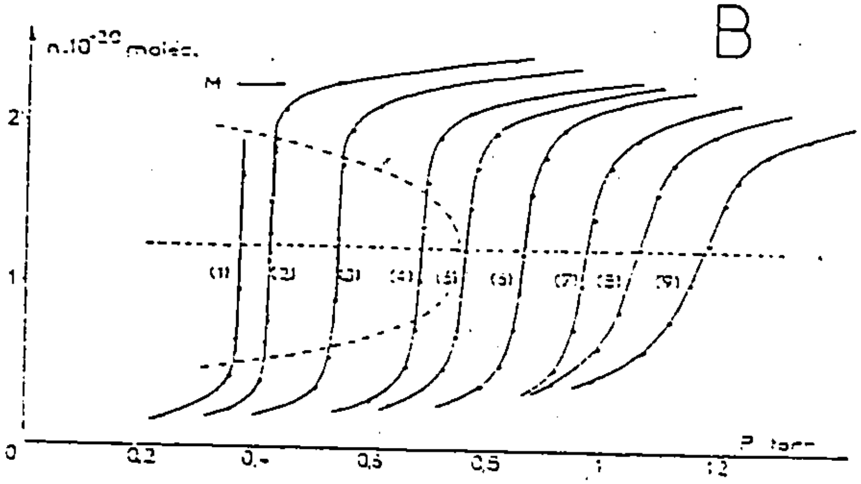
B
n.10^{-20} moléc.
M
2
1
0
(1)
(2)
(3)
(4)
(5)
(6)
(7)
(8)
(9)
0.2
0.4
0.6
0.8
1
1.2
P torr

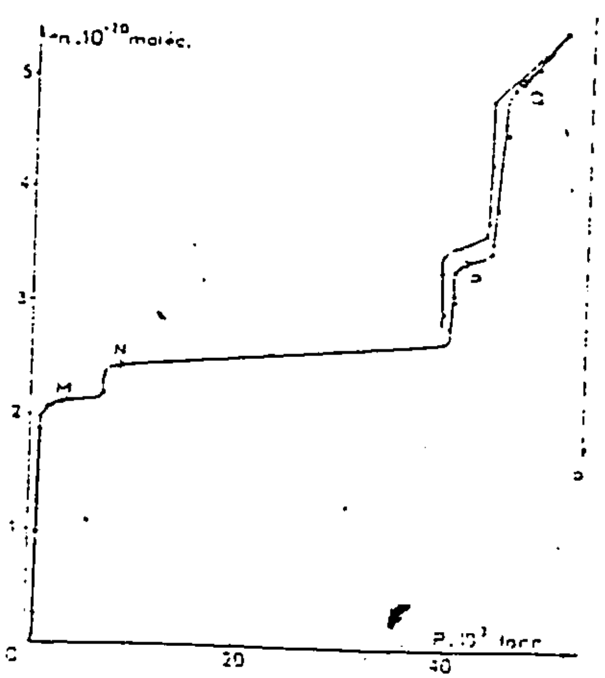
C
n.10^{-20} moléc.
5
4
3
2
1
0
M
N
O
P
20
40
P.10^{3} torr

$$\left(\frac{\partial \ell n P}{\partial n}\right)_T \qquad (3.1)$$

where n is the quantity adsorbed and P is the pressure. The derivative is taken at half a monolayer. At the critical temperature, the film undergoes a transition from a liquid-gas coexistence to a hypercritical fluid phase with a change in the temperature dependence of the slope. This large difference in estimated values of the 2D critical temperature is puzzling.

For simple molecules, it has been shown that the ratio of the two and three dimensional critical temperatures is $T_C(2D)/T_C(3D) = 0.40 \pm 0.05$ (27). The largest deviation from this value is for Cyanogen, 0.475 (27). From the data of Menaucourt et al (19) $T_C(2D)/T_C(3D) = 0.51$, which is to be compared with 0.39 found in this work. Terlain and Larher (27) obtained isotherms for CO_2, a molecule similar to C_2H_2 in several ways, and found features similar to those of Figure 3.1 with liquid-solid and liquid-gas coexistence regions and $T_C(2D)/T_C(3D) = 0.42$. CO_2 and C_2H_2 have the same structure in the bulk solid (Pa_3) and similar quadrupole moments, as well as similar sublimation and critical temperatures in 3D (195 and 304 K for CO_2 and 189 and 308K for C_2H_2). Menaucourt et al measured pressures with a mercury McLeod gauge which is not as precise as a Baratron manometer. Also, mercury reacts with acetylene.

The graphite substrates used for the experiments were not the same. Menaucourt et al used an uncompressed exfoliated graphite which has been shown (28) to yield sharper features in isotherms than does graphite GTA. They have been interpreted to mean that the former material has a more homogeneous surface (greater correlation length). If size effects are playing a significant role, in reducing the transition temperature, then, one might expect the observed transition temperature to be lower for the adsorption on Grafoil. On the other hand, Terlain and Larher used a substrate which was very similar to that used by Menaucourt et al (19).

A measurement of the critical temperature, with a different experimental technique, would possibly settle the inconsistency, but no such experiment has been performed to date. The possible kinds of experiments which can be made on physisorbed layers are scattering (neutron, atom, ions, electron, x-rays), NMR, and thermodynamic. In the scattering experiments, the different mobilities in the hypercritical and liquid phases can be observed through the intensities of the inelastic components. The results of NMR studies of methane (29) adsorbed on Grafoil indicated different behaviour of the spin-lattice relaxation times as a function of both temperature and density in the liquid-gas coexistence and hypercritical phases. Recently (30), the critical temperature of adsorbed methane was estimated through heat capacity measurements. This calorimetric method might be tried with C_2H_2 but the experimental problems in handling C_2H_2 would make it somewhat more difficult than for CH_4.

3.2 Absolute Area

A proper analysis of adsorption isotherms requires a knowledge of the area presented to the adsorbing molecules. In the present work, the area was determined in two ways with excellent agreement. The first method involved the measurement of an isotherm of carbon monoxide at low temperature (58 K). X-ray scattering and LEED experiments have shown that the completed monolayer is a commensurate $1\times\sqrt{3}$ solid structure (Figure 1.1), with a corresponding projected area of 15.72 $Å^2$/molecule. Primarily due to surface inhomogeneity, the film would not be expected to be ideal and the experimental area not exactly 15.72 $Å^2$/molecule. But, where the surface is not ideal, the molecule is still adsorbed, and therefore the relative error in the area is very much smaller than the relative area of the damaged regions. It is difficult to place error estimates on the area determined in this way. The amount of gas needed to complete the $1\times\sqrt{3}$ structure was 60×10^{-4} moles, which on the assumption of the ideal area of 15.72 $Å^2$/molecule, yields an absolute area of 568 m^2.

The simplicity of the above method is due to the fact that, at 58 K, the adsorbed CO is commensurate with the well-known structure of the graphite substrate. At 111 K, a Xe monolayer on graphite has a close packed structure which is incommensurate with the substrate (31). Thus, x-ray scattering data (31) were used to determine the Xe atom-atom separation. A x-ray scattering peak corresponding to the planes shown in the inset of Figure 3.3 was found at 1.61 ± 0.01 $Å^{-1}$ and it yields a plane separation of 3.90 ± 0.02 Å. This implies an area of 17.58 ± 0.22 $Å^2$/molecule. From a Xe isotherm at 111 K, also shown in Figure 3.3, the total surface area is found to be 556 ± 12 m^2, which is in excellent agreement with the first method used.

No further remarks will be made here about the 2D gas, 2D gas-liquid, 2D liquid-solid, 2D liquid and hypercritical phases at low temperatures. The remainder of this section will deal with the two

Figure 3.3. Isotherm of Xe on Grafoil at T = 111 K. The arrow indicates coverage for 1 monolayer. The Insets are an x-ray diffraction peak obtained at 1 monolayer and T = 112 K, ref. (31) and the Xe planes to which this peak corresponds.

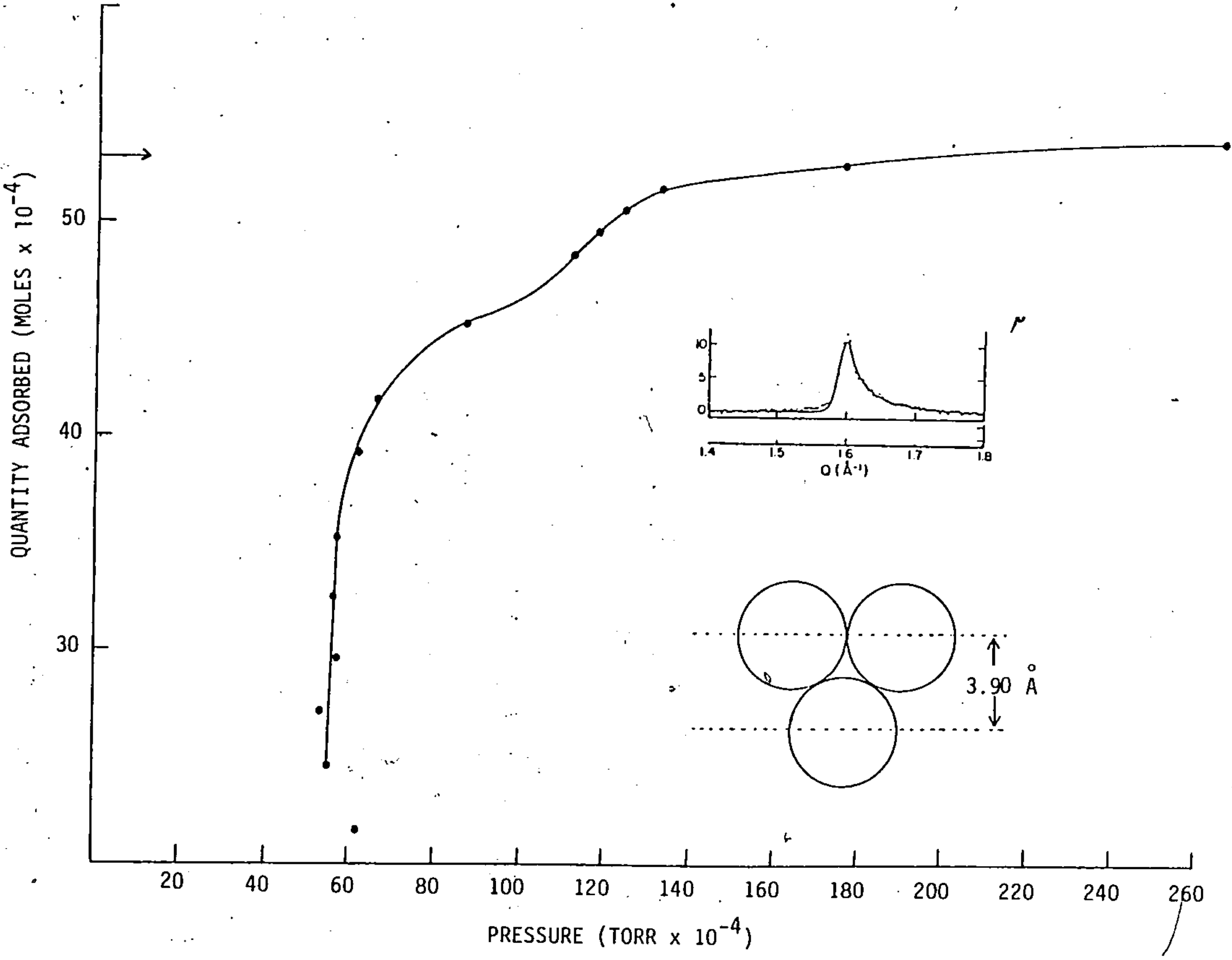
QUANTITY ADSORBED (MOLES x 10^{-4})
50
40
30
PRESSURE (TORR x 10^{-4})
20
40
60
80
100
120
140
160
180
200
220
240
260
10
5
0
1.4
1.5
1.6
1.7
1.8
Q (Å^{-1})
3.90 Å

solid phases.

Menaucourt et al (19) used the surface density and the shape of the acetylene molecule in proposing the structures in Figure 3.4A. The areas of solids I and II (points M and N respectively in Figure 3.2) were 18.6 ± 0.7 and 16.1 ± 0.6 $\mathring{A}^2$/molecule. The proposed low density, solid I, structure is incommensurate with the substrate, and the molecules lie flat on the surface with hydrogen atoms in contact. If C_2H_2 molecules are considered to be rigid sticks this is not an unreasonable structure, but, if standard interaction potentials are considered the proposal is extremely unlikely. The most unfavourable arrangement for molecules with large quadrupole moments is to lie side by side. It can be shown that this proposed structure is not bound to the surface when typical potentials presented in Chapter 4 are employed in the calculation.

The proposed high density solid II structure (point N of Figure 3.2) has the molecules standing vertically in the commensurate $1x\sqrt{3}$ positions. Again, for molecules with large linear quadrupole moments, this arrangement is very unfavourable and the orientation with respect to the surface is the most unfavourable. It can be shown that the structure corresponding to this proposal is also unbound.

It would be difficult if not impossible to guess the structures of the two solids on the basis of the isotherm data alone. Later, results of calculations will be presented to assist the structural deductions. A couple of points will be made now. The densities of the two solids as estimated here are 18.9 ± 0.5 and 15.7 ± 0.3 $\mathring{A}^2$/molecule, which are comparable to those found by Menaucourt et al, 18.6 ± 0.7 and

Figure 3.4A. The two solid structures for C_2H_2/graphite proposed by Menaucourt (19).

Figure 3.4B. The two solid C_2H_2 structures for C_2H_2/graphite from the neutron diffraction study (20).

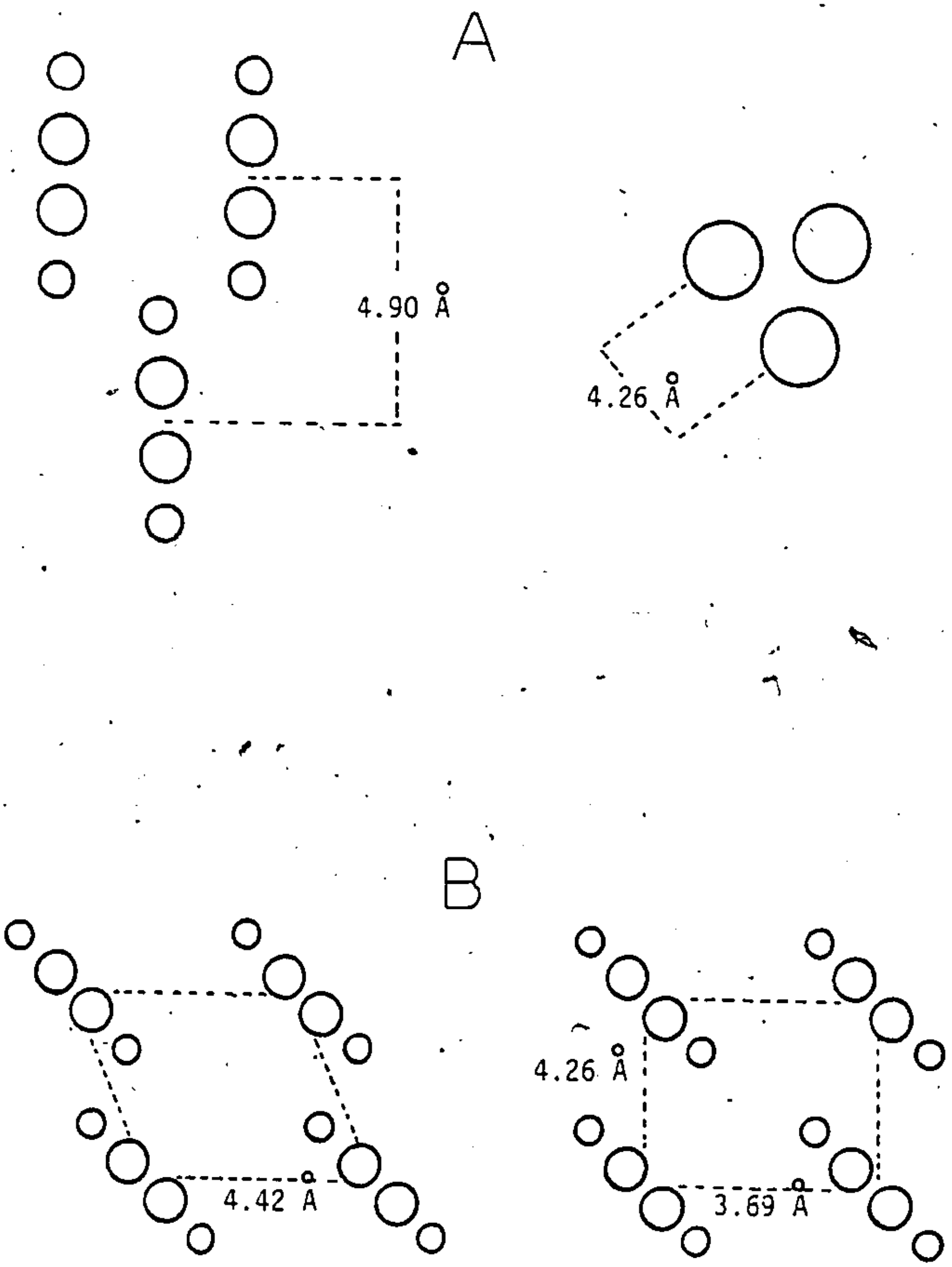
A
4.90 Å
4.26 Å
B
4.42 Å
4.26 Å
3.69 Å

16.1 ± 0.6 Å^2/molecule. Within the uncertainties, the two sets of estimates overlap. Both agree that the solid II area is that of the commensurate 1x$\sqrt{3}$ solid, 15.72 Å^2/molecule. The reason for the discrepancies is probably due to the methods used to determine the total area of the substrate. Menaucourt et al used a value of 14.7 ± 0.3 Å^2 (32) for the cross-sectional area of a Kr atom, with the number of Kr atoms needed to complete a monolayer. The problem with this method is that the cross-sectional area of a polarizable molecule such as Kr could change when the molecule is placed near a polarizable surface such as graphite. In fact, it is the polarizability of the atom and the surface that leads to adsorption.

The only other experiment which has been performed on the two solid structures of adsorbed C_2H_2 was neutron diffraction (20). It verified that the two solids have different structures. Two Bragg peaks were obtained for each structure, and the two proposed structures are displayed in Figure 3.4B. The low density solid is incommensurate with the substrate and the molecules lie flat on the surface, whereas the high density phase is commensurate with the graphite substrate but the molecules are tilted 35° from the surface. The proposed high density phase is not the 1x$\sqrt{3}$ structure but has an area of 15.72 Å^2/molecule. Both proposals assume no basis in the lattice, i.e., all molecules have the same orientation. Calculations to be presented later will show two different structures which also agree with the diffraction data.

Isotherms, at surface coverages beyond a monolayer, were obtained over a limited temperature range between 109 - 111 K (Figure 3.5). There

Figure 3.5. Isotherms obtained at densities beyond 1 monolayer at T = 109.47 K, 110.3 K and 111.14 K.

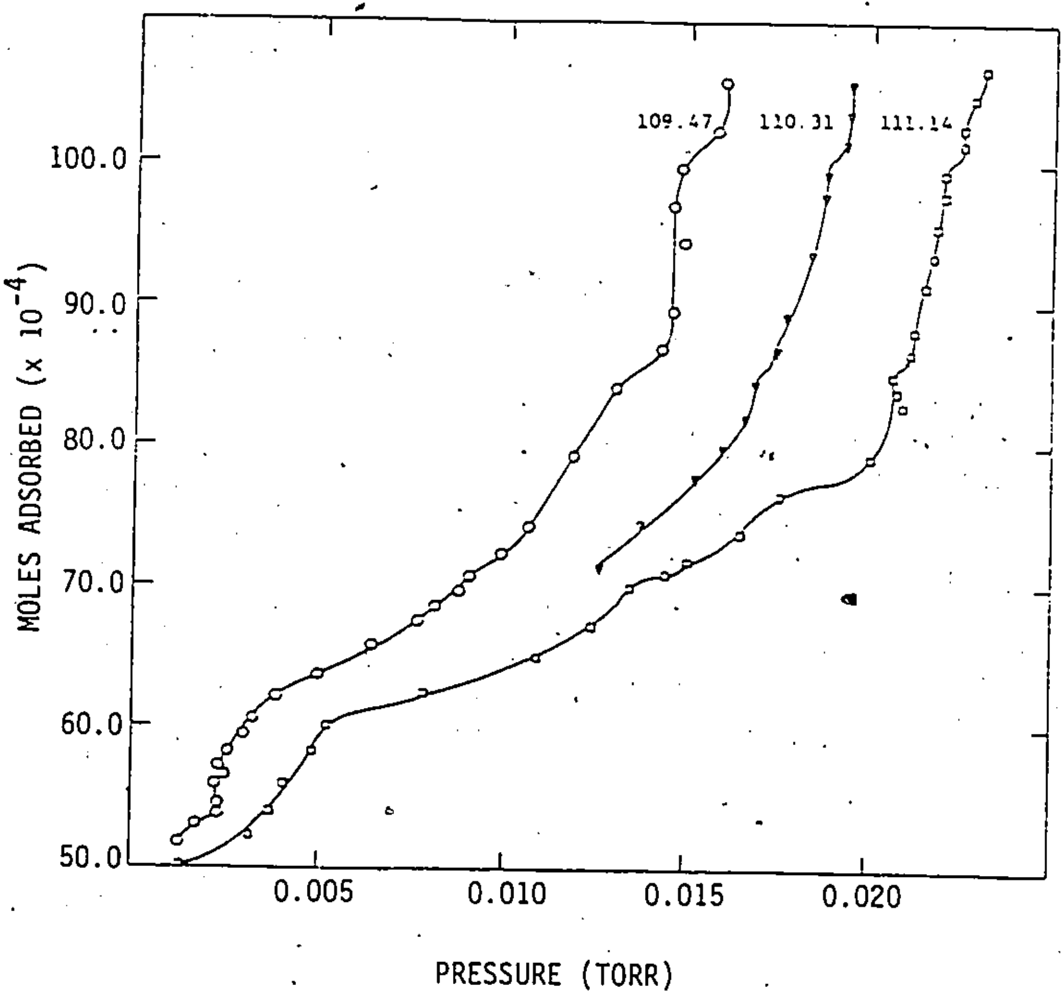
109.47
110.31
111.14
MOLES ADSORBED (x 10^{-4})
100.0
90.0
80.0
70.0
60.0
50.0
0.005
0.010
0.015
0.020
PRESSURE (TORR)

are two features of interest here. The kink at 100×10^{-4} moles adsorbed in all 3 curves represents a density that is close to twice that of solid I and this suggests the formation of a bilayer. In order for the bilayer to be of the solid I structure, the first layer would have to make a transition from solid II back to solid I. This transition would need to occur in the region preceding the vertical section in the 2nd layer, and could be responsible for the observed distinct curvature in this part of the isotherm. Although the features attributed to the bilayer appear reproducible, this was only true if the experiments were done slowly. In runs where the monolayer was created very quickly, the kinks appeared at different densities and were not reproducible. In the experiment at 109 K, the film was built up over a period of almost 4 weeks and the features are much more clearly defined than in either of the other two, where the film was created in 2 days.

Menaucourt et al (19) had seen transitions at higher densities which were attributed to both structural transitions in the first layer and to the formation of a second layer. In the first of these (point P in Figure 3.2), the film was seen to make a transition from the $1 \times \sqrt{3}$ commensurate arrangement with the molecular axis perpendicular to the surface to a close packed incommensurate structure with the molecules still standing on the surface. As mentioned earlier, this structure can be shown to be unbound. The second transition (point Q in Figure 3.2) was seen to be a bilayer of the (III) face of the cubic phase of the 3D crystal or a bilayer of solid II (point N of Figure 3.2) rather than of solid 1.

3.3 Isotherms at Higher Temperatures

Isotherms at temperatures greater than 117 K, displayed in Figures 3.6, 3.7 and 3.8 were measured at high densities in order to examine the disappearance of the solid I to solid II transition. That seemed to occur gradually. However, conjecture on what is happening here would be very speculative if it were based on these data alone.

3.4 Low Density Isotherms

Some of the most interesting results of the experiments were the values of Henry's Law constants as a function of temperature. Henry's Law constant is defined to be the slope of an isotherm in the limit of zero coverage (density), where the adsorbed molecules can be considered to be non-interacting, i.e., a 2D ideal gas. In this limit it can be shown that the isotherm should be linear. Another important quantity, which will also be discussed is the isosteric heat of adsorption. Experimentally, this is the heat released when a molecule in the 3D gas phase above the surface is adsorbed at constant temperature, and is given by the relation:

$$q_{ST} = k_B T^2 \left(\frac{\partial \ell n P}{\partial T}\right)_n \qquad (3.2)$$

A plot of q_{ST} vs. coverage, obtained with the aid of eq. 3.2, is shown in Figure 3.9 for several temperatures. At low temperatures, the small absolute pressure differences have such large uncertainties that no values of q_{ST} below 124 K are presented. The scatter in the values of q_{ST} is an indication of the uncertainties involved in the use of eq. 3.2. Piper et al (34) have measured q_{ST} for CO/graphite directly using a

Figure 3.6. Isotherms for C_2H_2/Grafoil obtained at T = 117.84 K, 122.70 K, 124.50 K, 130.38 K.

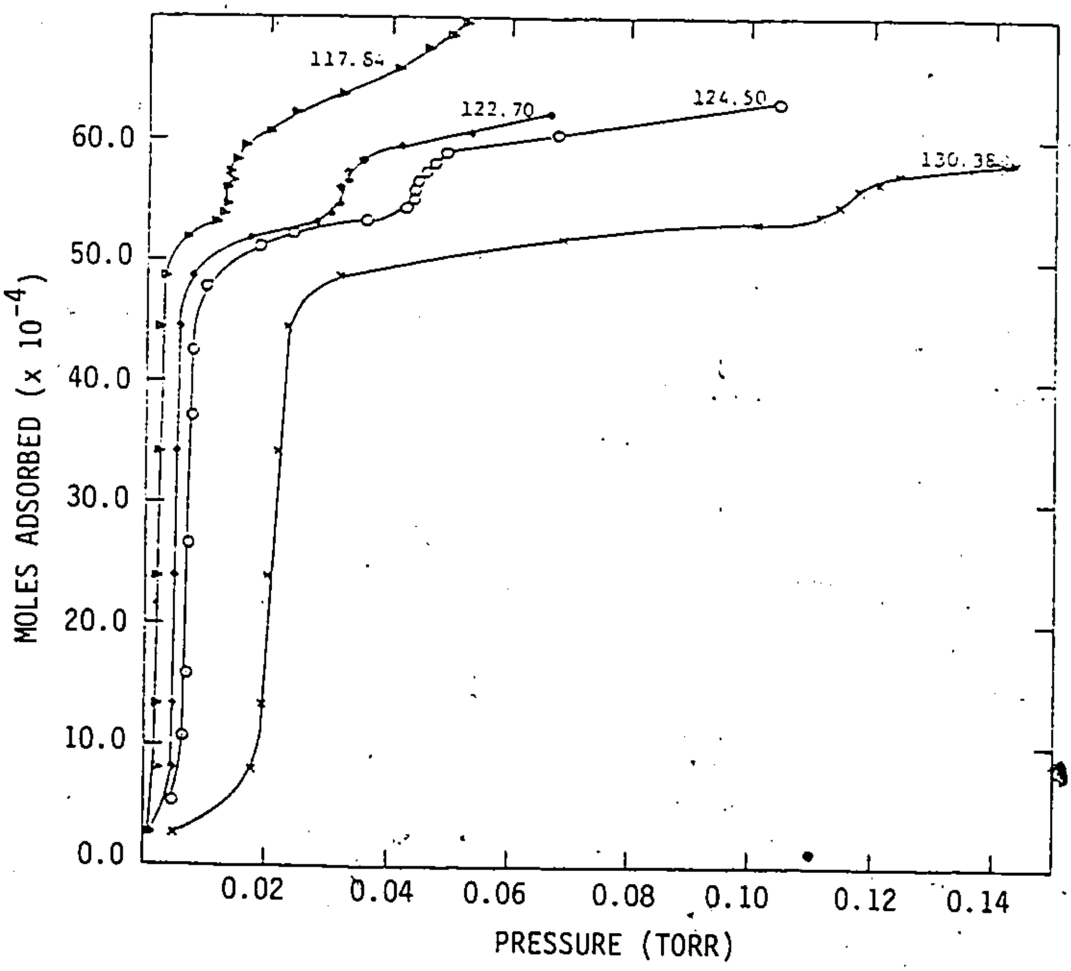
117.84
122.70
124.50
130.38
MOLES ADSORBED (x 10^{-4})
0.0
10.0
20.0
30.0
40.0
50.0
60.0
0.02
0.04
0.06
0.08
0.10
0.12
0.14
PRESSURE (TORR)

Figure 3.7. Isotherms for C_2H_2/Grafoil obtained at T = 134.89 K, 146.10 K, 154.11 K, 163.86 K, 173.85 K, 183.76 K, 182.70 K.

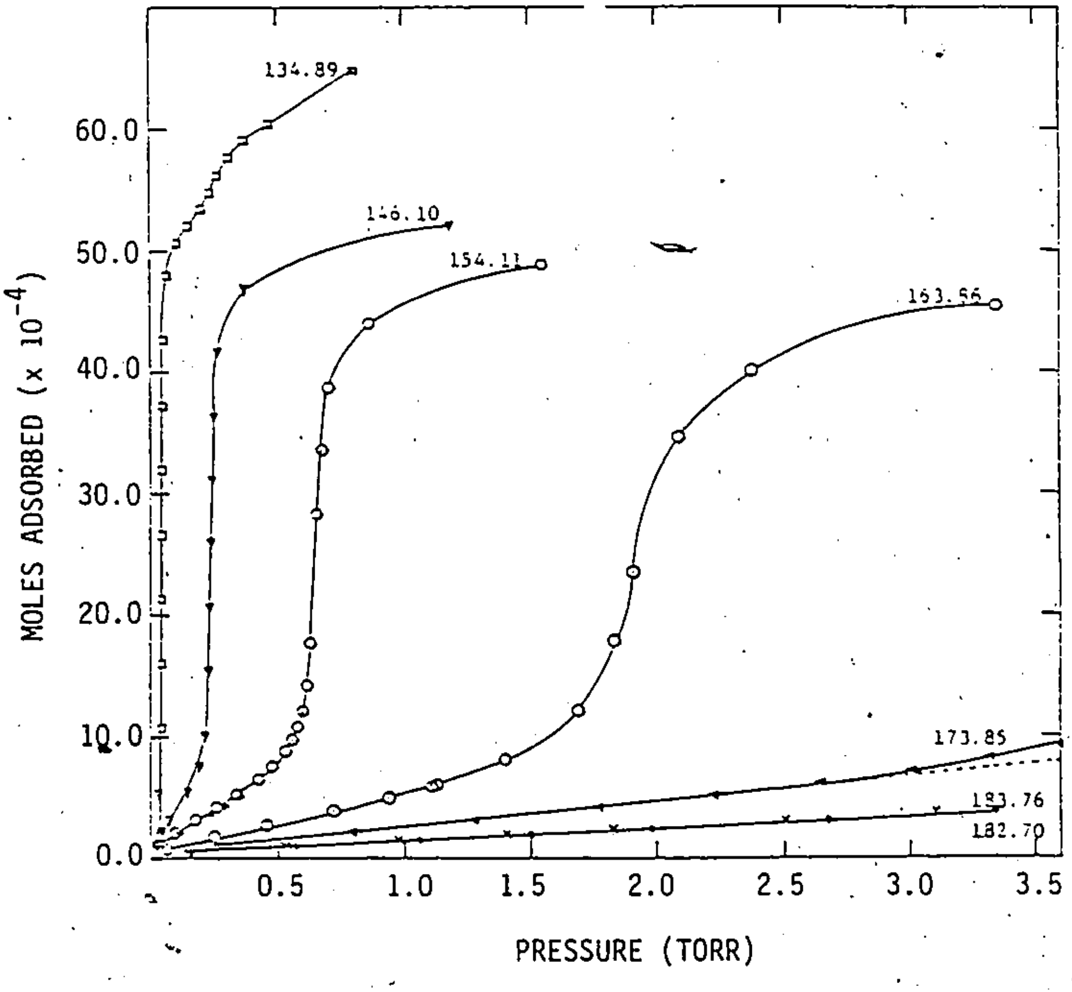
134.89
146.10
154.11
163.56
173.85
183.76
182.70
60.0
50.0
40.0
30.0
20.0
10.0
0.0
0.5
1.0
1.5
2.0
2.5
3.0
3.5
MOLES ADSORBED (x 10^{-4})
PRESSURE (TORR)

Figure 3.8. Isotherms obtained at low coverage for C_2H_2/Grafoil at T = 163.86 K, 173.85 K, 182.70 K, 183.76 K.

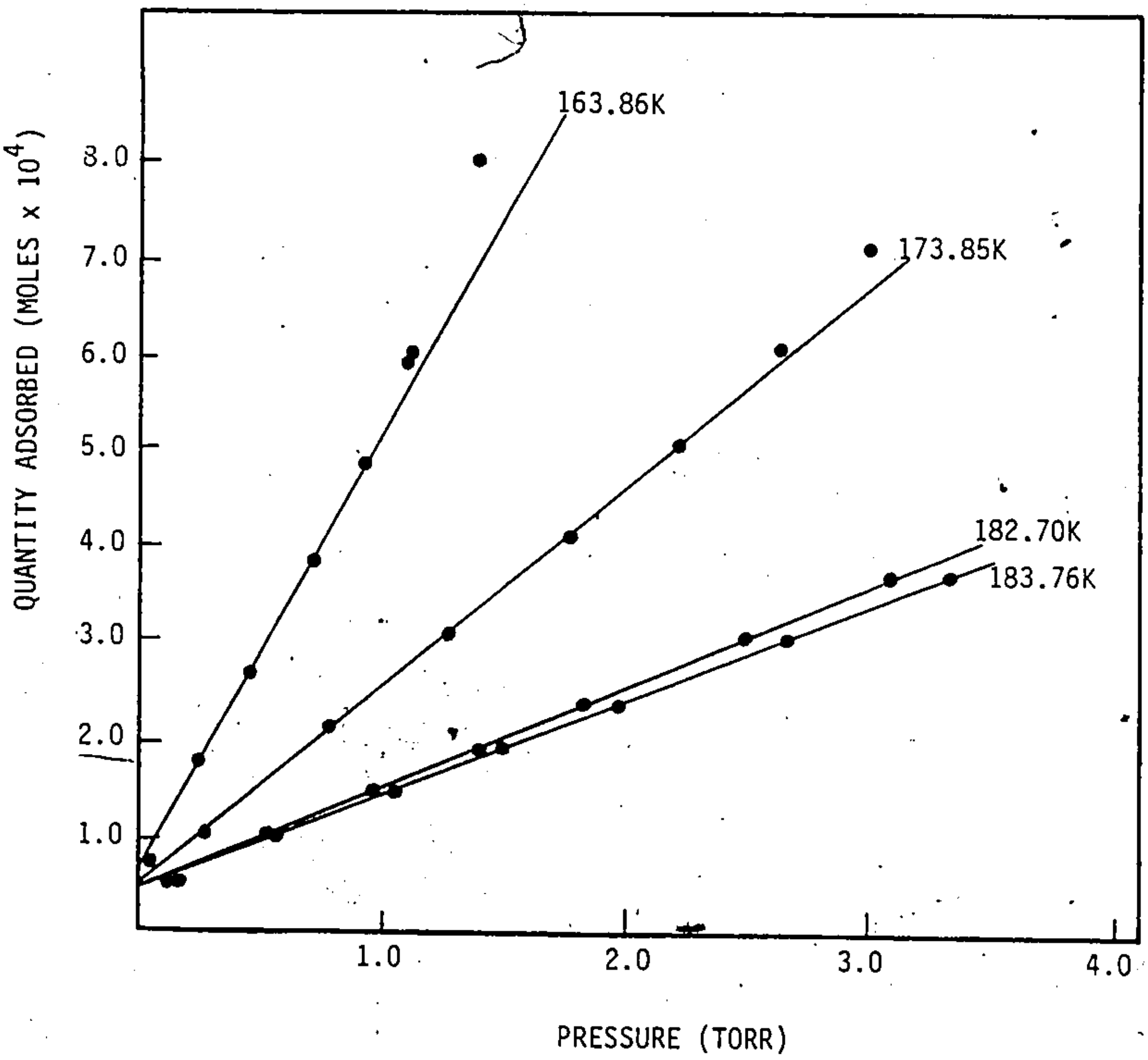
163.86K
173.85K
182.70K
183.76K
QUANTITY ADSORBED (MOLES x 10^4)
8.0
7.0
6.0
5.0
4.0
3.0
2.0
1.0
1.0
2.0
3.0
4.0
PRESSURE (TORR)

Figure 3.9. Isosteric heat of adsorption of C_2H_2/Grafoil vs. coverage obtained with the use of eq. (3.2) and the isotherm data. The lines serve only as a guide to the eye.

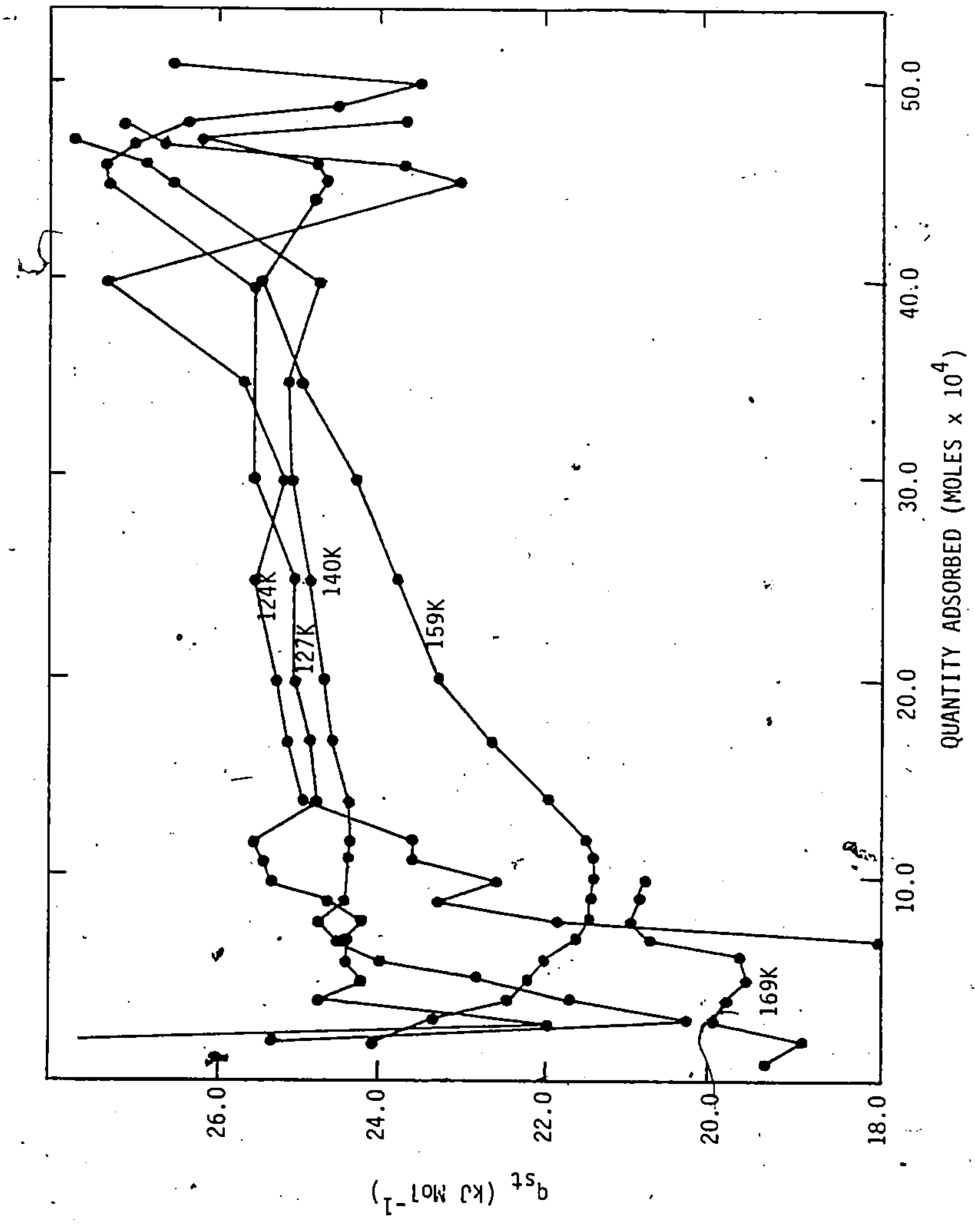

26.0
24.0
22.0
20.0
18.0
q_{st} (kJ Mol^{-1})
10.0
20.0
30.0
40.0
50.0
QUANTITY ADSORBED (MOLES x 10^4)
124K
127K
140K
159K
169K

calorimetric technique. The results for CO/graphite are displayed in Figure 3.10; the uncertainties are only of the order of 1%. Because of the reactivity of C_2H_2, this apparatus could not be employed for measurements on it (copper was used for the sample cell to obtain a necessarily high thermal conductivity). A quantity, which will be needed later, is the integral heat of adsorption of a completed monolayer (∿ 52×10^{-4} moles) of solid I at low temperature.

$$Q(n_o) = \int_0^{n_o} q_{ST}\, dn \tag{3.3}$$

Because of the scatter in the data, it is difficult to estimate Q, but smoothing and integrating the curves for 124, 127, and 140 K yields a value of 25 ± 1 kJ Mol^{-1} at T = 130 K. The harmonic approximation with 5 degrees of vibrational freedom yields a cohesive energy of 26.6 ± 1 kJ Mol^{-1} from the equation

$$q_{ST} = -\langle U\rangle_{T=0} - \frac{n}{2} k_B T + k_B T \tag{3.4}$$

where n is the number of degrees of vibrational freedom and <U> is the potential energy at T = 0 K, a quantity easily calculated as a function of density. For a 2D ideal gas one can show that:

$$q_{ST} = k_B \frac{\partial \ln k_H}{\partial(1/T)}, \tag{3.5}$$

a useful relation between Henry's constant (k_H) and q_{ST}.

Prior to presenting results for k_H and q_{ST}, it is necessary and informative to explain a snag in the definition of k_H presented above. Henry's law constants are measured to obtain information on the molecule-surface interaction. There are no ideal surfaces. All surfaces have a nearly continuous and peaked distribution (perhaps Gaussian) of

Figure 3.10. Isosteric heat of adsorption vs. coverage for CO/Grafoil from Piper et al (34). The different symbols represent independent runs.

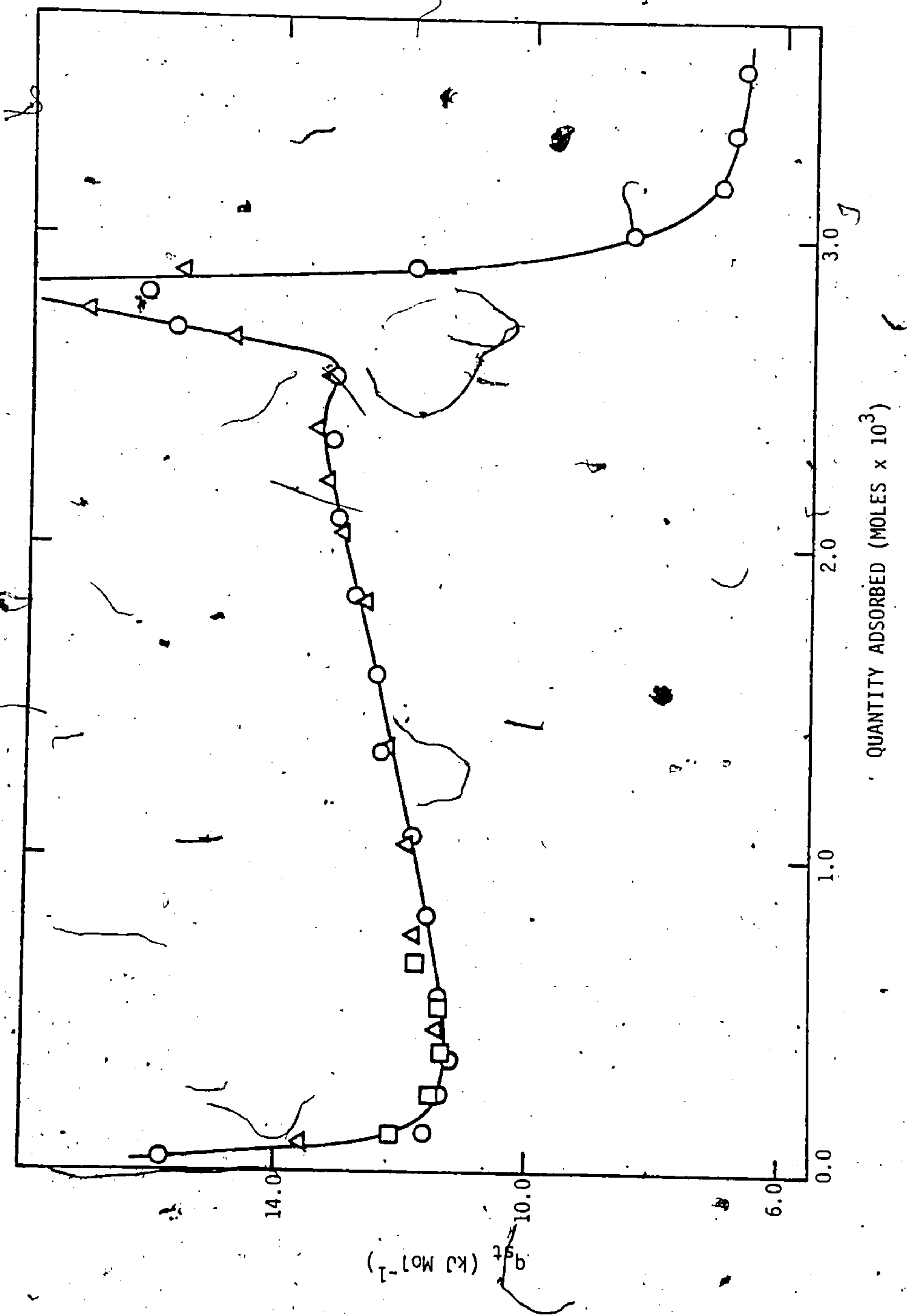
14.0
10.0
6.0
q^{st} (kJ Mol^{-1})
0.0
1.0
2.0
3.0
QUANTITY ADSORBED (MOLES x 10^3)

adsorption energies, but normally interest is focussed on the most homogeneous regions. The first adsorbed molecules fill up the high energy wing of this distribution. This can be seen from the direct measurements of q_{ST} shown in Figure 3.10. The larger values of q_{ST} at low coverage are presumably due to adsorption on the damaged areas of the surface and perhaps on the metallic parts of the sample cell. A large value of q_{ST} manifests itself as a large slope of the adsorption isotherm. An examination (on an expanded scale) of the highest temperature isotherms (175 - 185 K) reveals a very large initial slope followed by a change to a long linear region. A later increase in slope occurs when the molecule-molecule interactions become significant. The large initial slope is presumably that caused by the molecules being strongly bound in the deepest energy wells. For this reason, the slope of the long linear region, and not the initial slope, was taken to determine the Henry's law constant.

An extrapolation of the high temperature q_{ST} vs. coverage curve to zero density yields a value of 19.0 ± 0.5 kJ mol^{-1} for the isosteric heat of one isolated molecule. A better way to determine this quantity is to plot $\ln(K_H)$ vs. 1/T, the slope of which yields q_{ST} through eq. 3.3. The plot is shown in Figure 3.11 and gives the result for q_{ST} of 19.4 ± 0.5 kJ Mol^{-1}.

At this point, it should be mentioned that these results for q_{ST} are not in agreement with the values of q = 17.3 kJ Mol^{-1} at 183 K as determined from the gas chromatography measurements (84). No estimates of the errors were offered in the latter work. Comparisons of the gas chromatography results for CH_4 and the direct measurements of Piper and Morrison shows the gas chromatography results to be smaller by ∿ 1 kJ Mol^{-1}.

Figure 3.11. The logarithm of Henry's Law constant vs. inverse temperature for C_2H_2/Grafoil. The error bars lie within the symbols.

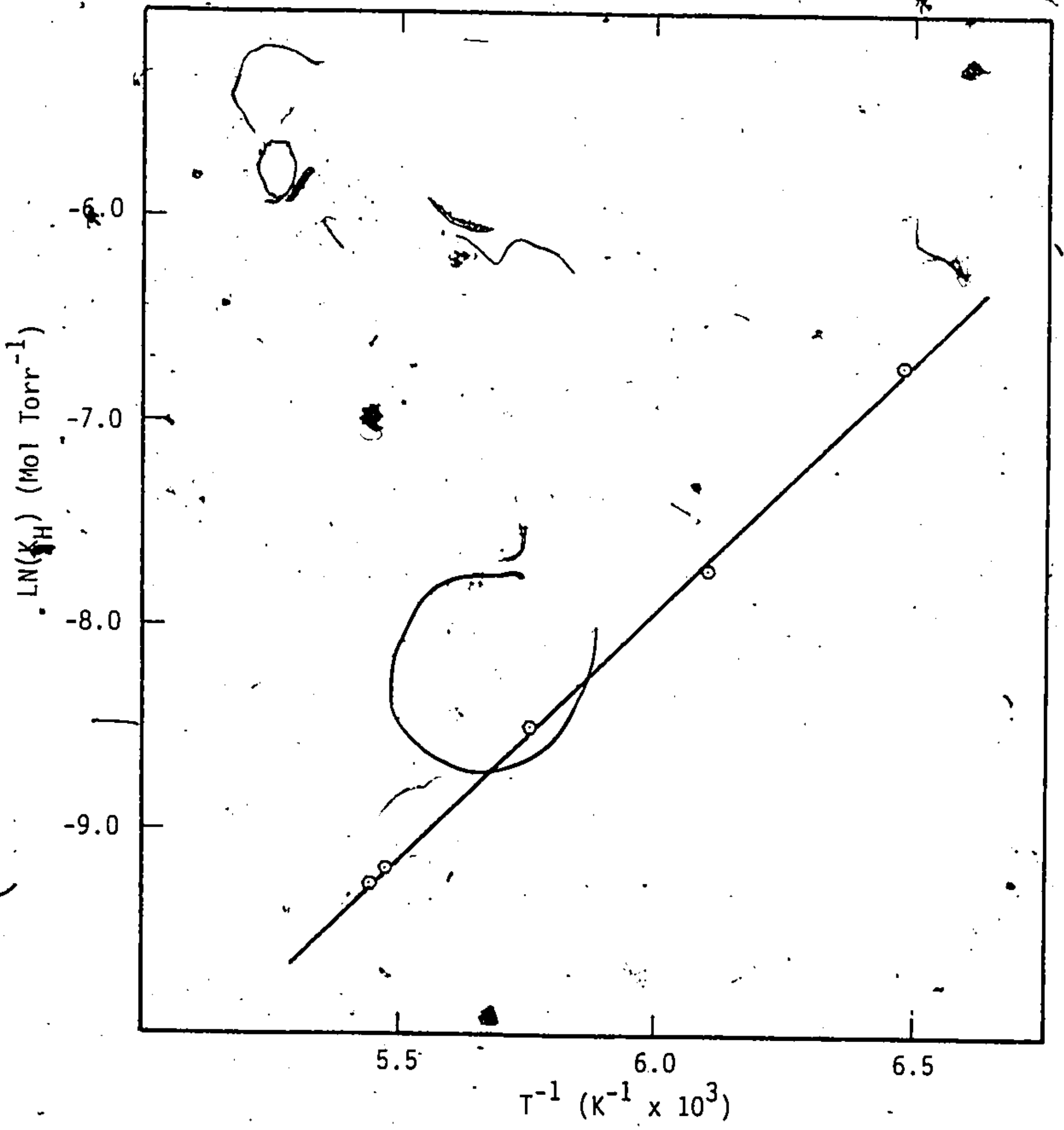
-6.0
-7.0
-8.0
-9.0
LN(K_H) (Mol Torr^{-1})
5.5
6.0
6.5
T^{-1} (K^{-1} x 10^3)

In the following section measurements of q_{ST} for CO from isotherms will be shown to compare well with the direct measurements. As yet, this disagreement is unresolved.

The full significance of these Henry's Law constants will only become apparent in a later chapter when an attempt to calculate them with a potential model is made.

3.5 Carbon Monoxide Isotherms

The isotherms of carbon monoxide on Grafoil are displayed in Figure 3.12. The two dimensional critical temperature can be identified as lying between 60.4 K and 62 K because the isotherm at T = 60.4 K has a vertical segment but the one at 62.0 does not. The three-dimensional critical temperature is 134.4 (14) from which we obtain $T_C(2D)/T_C(3D) = 61.0/134.4 = 0.45$.

The existing information about the phase diagram for the CO/graphite system obtained from x-ray scattering (23), LEED (24), and thermodynamic results (34) is summarized in Figure 3.13. The contribution to this phase diagram from the isotherm data is the identification of the critical temperature.

At four higher temperatures, Henry's Law constants were measured and plotted against inverse temperature, (Figure 3.14). From the slope in the latter figure and eq. 3.3, the value of the isosteric heat at zero coverage was found to be 11.25 ± 0.3 kJ mol^{-1} at a mean temperature of 93.2 K. An independent direct calorimetric measurement (34) Figure (3.10) gave the result of 11.0 ± 0.1 kJ mol^{-1} which is in good agreement. As in the case of acetylene, there will be further discussion about Henry's Law constants when the calculations based on potential models are presented.

Figure 3.12. Isotherms obtained for CO/Grafoil at T = 58.0 K, 60.4 K, 62.0 K, 63.9 K.

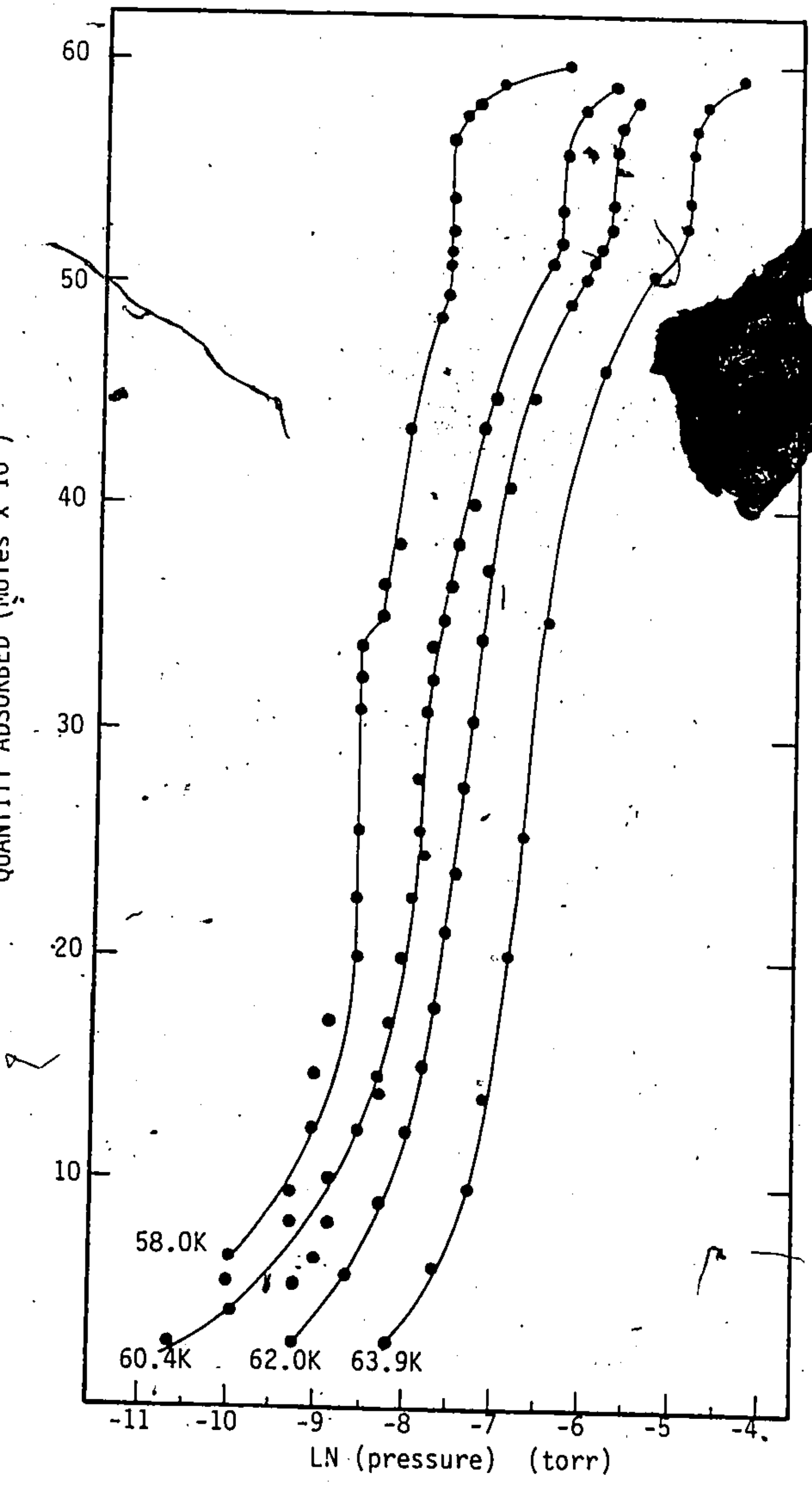
QUANTITY ADSORBED (Moles x 10^4)
60
50
40
30
20
10
58.0K
60.4K
62.0K
63.9K
-11
-10
-9
-8
-7
-6
-5
-4
LN (pressure) (torr)

Figure 3.13. A phase diagram for Carbon Monoxide adsorbed on graphite from x-ray (23), LEED (24) and thermodynamic (34) studies.

CO - commensurate and ordered

CD - commensurate and disordered

IO - incommensurate and ordered

ID - incommensurate and disordered

IP - incommensurate and pinwheels

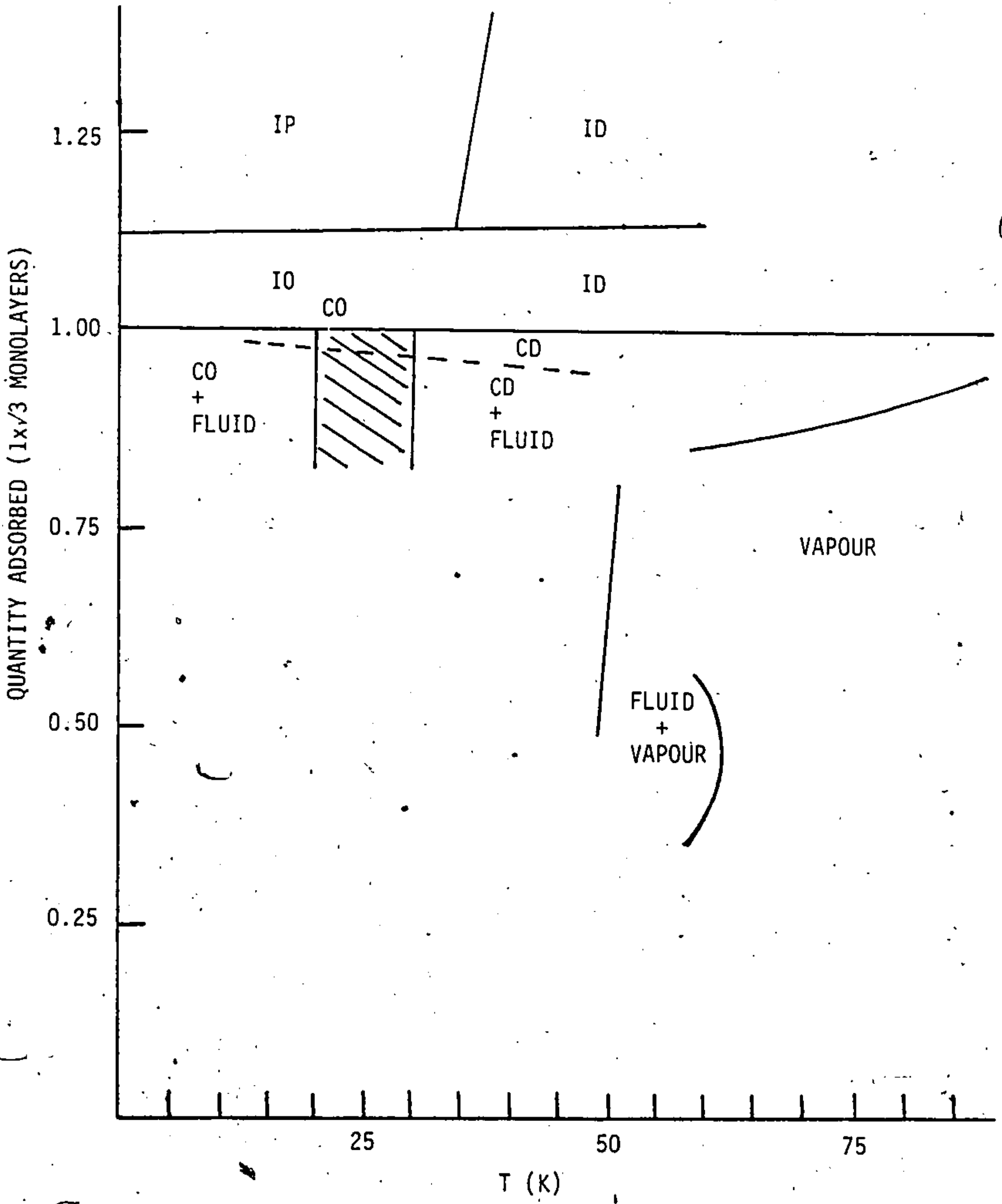
IP
ID
IO
ID
CO
CD
CO
+
FLUID
CD
+
FLUID
VAPOUR
FLUID
+
VAPOUR
1.25
1.00
0.75
0.50
0.25
QUANTITY ADSORBED (1x√3 MONOLAYERS)
25
50
75
T (K)

Figure 3.14. The logarithm of Henry's Law constant vs. inverse temperature for CO/Grafoil. The error bars lie within the symbols.

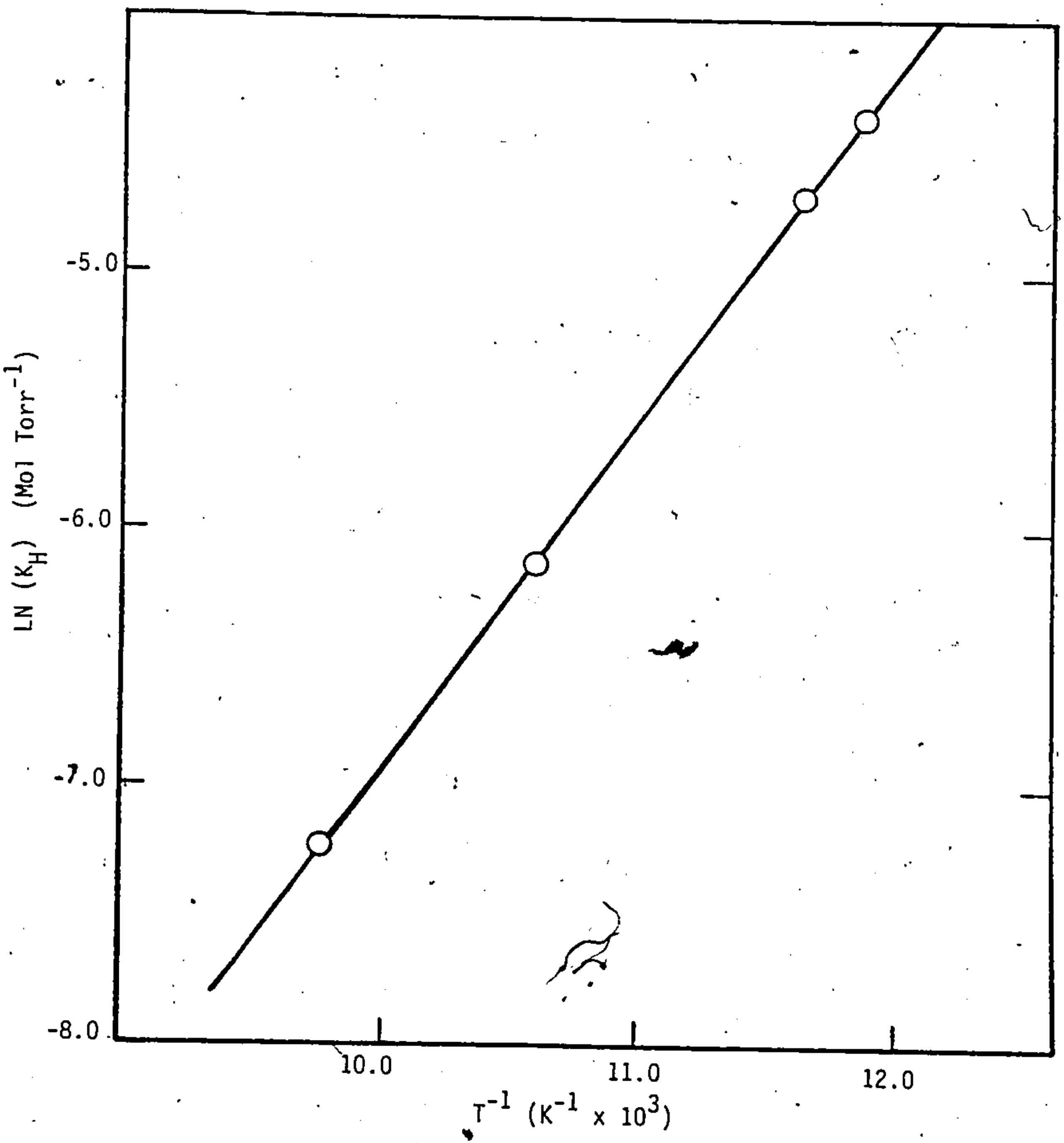
-5.0
-6.0
-7.0
-8.0
LN (K_H) (Mol Torr^{-1})
10.0
11.0
12.0
T^{-1} (K^{-1} x 10^3)

CHAPTER 4

INTRODUCTION TO INTERMOLECULAR POTENTIALS

4.1 Ab Initio Calculations

The properties of an adsorbed film are determined by the interaction forces between the molecules and between the molecules and the surface. In physical adsorption the molecules remain as distinct units, because the interaction energy between the molecules is much smaller than bonding energies of the atoms. Hence, they are known as molecular systems.

The interaction between two molecules (A,B) can be approximated up to second order by (35,36)

$$\Delta E = \langle A\psi_o^A\psi_o^B|H^{AB}|A\psi_o^A\psi_o^B\rangle - \langle\psi_o^A|H^A|\psi_o^A\rangle - \langle\psi_o^B|H^B|\psi_o^B\rangle$$
$$+ \frac{\sum_{r,s}{}' \langle\psi_o^A\psi_o^B|V^{AB}|\psi_r^A\psi_s^B\rangle\langle\psi_r^A\psi_s^B|V^{AB}|\psi_o^A\psi_o^B\rangle}{E_o^A - E_r^A + E_o^B - E_s^B} \quad (4.1)$$

where A is an antisymmetrization operator, H^A, H^B, H^{AB} are the isolated molecule and dimer Hamiltonians and

$$V^{AB} \equiv H^{AB} - H^A - H^B$$

$$= \sum_i{}' \sum_j \frac{e_j^B e_i^A}{r_{ij}} \quad (4.2)$$

Exchange has only been considered in the first order, because second order exchange energies have been found to be very small (36). The prime in the summation of eq. 4.1 indicates that both r and s $\neq 0$.

Although, in principle, eq. 4.1 can be evaluated for all orientations and separations, this is only practicable, in terms of computer time, for simple molecular and rare gas dimers. The best results have been found for the simplest systems such as $He^{3,4}$ and H_2 dimers (35,36,37), but recently calculations on systems of larger molecules including CO (5) and C_2H_2 (18) have been performed. Equation 4.1 is prohibitively complicated to use in calculations on condensed systems. Approximate model potentials have been developed for them based on the individual terms of eq. 4.1.

The first approximation is the arbitrary division of the interaction eq. 4.1 into long and short range solutions and then to combine them to describe the potentials of intermediate range.

At long range, where the molecular wavefunctions do not overlap significantly, the antisymmetrization operator 'A' is replaced by the identity operator leading to:

$$\begin{aligned}\Delta E = {} & \langle\psi_o^A\psi_o^B|V^{AB}|\psi_o^A\psi_o^B\rangle + \sum_{\substack{r=0\\ s\neq 0}} \frac{|\langle\psi_o^A\psi_o^B|V^{AB}|\psi_o^A\psi_s^B\rangle|^2}{E_o^B - E_s^B} \\ & + \sum_{\substack{s=0\\ r\neq 0}} \frac{|\langle\psi_o^A\psi_o^B|V^{AB}|\psi_r^A\psi_o^B\rangle|^2}{E_o^A - E_r^B} + \sum_{\substack{r\neq 0\\ s\neq 0}} \frac{|\langle\psi_o^A\psi_o^B|V^{AB}|\psi_r^A\psi_s^B\rangle|^2}{E_o^A - E_r^A + E_o^B - E_s^B}\end{aligned} \qquad (4.3)$$

In the limit of zero overlap V^{AB} can be expanded as a convergent multipole series and the first term in eq. 4.3 can be seen to be just the electrostatic multipole interaction energy. The second and third terms are known as the induction energy. They arise as a result of the static multipole of one molecule inducing a multipole in the other.

The last term in eq. 4.3 is the dispersion or van der Waal's energy. This interaction exists between any two polarizable molecules. A fluctuation produces a multipole in molecule A which then induces a multipole in molecule B.

The induction and dispersion terms can be calculated as a multipole expansion leading to anisotropic attractive interactions which vary as $1/r^6$ (dipole-dipole), $1/r^8$ (dipole-quadrupole) and $1/r^{10}$ (quadrupole-quadrupole) etc.

The induction forces are typically very much smaller than either the electrostatic or dispersion forces and are usually not included in the total interaction. It should be noted that the dispersion terms can be calculated by a semi-empirical method involving dipole oscillator strengths (f-values) deduced from the results of light scattering experiments (40,41). The long range interaction then consists of anisotropic electrostatic multipole-multipole and dispersion forces.

At short range, the situation is more complicated as one must evaluate eq. 4.1 with the antisymmetrized wavefunction (at least in first order). It is instructive to consider the first and second order energies as consisting of two parts. The first order energy is divided into electrostatic and exchange terms (38). The electrostatic term is the first order energy of eq. 4.1 with the antisymmetrization operator replaced by the identity operator. The first order exchange term is

$$E^{(1)}_{exch} = E^{(1)} - E^{(1)}_{elect} \qquad (4.4)$$

The effect of the overlap of the electron charge clouds on the long range multipole moments of the molecules can be estimated through the quantity

$$E^{(1)}_{penetration} = E^{(1)}_{elect} - E^{(1)}_{mult} \qquad (4.5)$$

where E_{mult} is the long range electrostatic energy. In a similar manner, the second order energy is partitioned into

$$E^{(2)}_{penetration} = E^{(2)} - E^{(2)}_{mult} \qquad (4.6)$$

where $E^{(2)}$ is the second order term in eq. 4.1 and E_{mult} is the long range multipole dispersion energy. The charge penetration or overlap effects have been shown to reduce the electrostatic interactions at typical lattice separations in solids. The exchange and penetration energies vary approximately exponentially and are strongly anisotropic.

The molecular separations of interest in condensed matter lie in an intermediate range. The potential in this region is constructed by adding the long range electrostatic and dispersion energies to the short range exchange and penetration energies.

The potentials described above involve complicated anisotropic interactions in a numerical form, but for use in a calculation on a condensed system, the potential must be described in a simple mathematical form. This is usually effected with multicentered interactions (atom-atom approximation). The short range and dispersion potentials are fitted to either the 6-12 or 6-exp form

$$\begin{aligned} V(r) &= 4\varepsilon\left(\frac{\sigma^{12}}{r^{12}} - \frac{\sigma^6}{r^6}\right) \\ V(r) &= Ae^{(-\alpha r)} - \frac{C_6}{r^6} - \frac{C_8}{r^8} - \frac{C_{10}}{r^{10}} \end{aligned} \qquad (4.7)$$

with several interaction sites in the molecule (often but not always the nuclear sites). More complicated forms have been suggested which involve the atom-atom method but with anisotropic parameters (37,42). The 6-12 potential is sketched in Figure 4.1, σ represents the separation at which the potential is zero and ε is the well depth. σ and α are measures of the atomic radii and C_6 and ε are measures of the atomic polarizability.

The electrostatic interaction is described with a distribution of point multipoles or charges which are fitted so as to reproduce the long range multipole moments of the molecule.

Only recently have evaluations of eq. (4.1) been feasible for molecules as complicated as N_2 but large molecular systems have been studied for some time. Empirical potentials have been developed by fitting the atom-atom parameters of eq. (4.7) to a wide range of experimental data including lattice dynamics, sublimation energies, crystal structures and virial coefficients. This approach has been used extensively in the development of potentials for hydrocarbons (43,44). Two approximations permeate the literature of atom-atom potentials. First is the assumption that a set of parameters for any type of atom can be transferred from one molecule to another. For example, potential parameters for oxygen in CO are transferred to oxygen in CO_2 or O_2 and vice versa. The second assumption deals with interactions of unlike atoms such as carbon and hydrogen. A common approximation is to work

Figure 4.1. The 6-12 Potential Form.

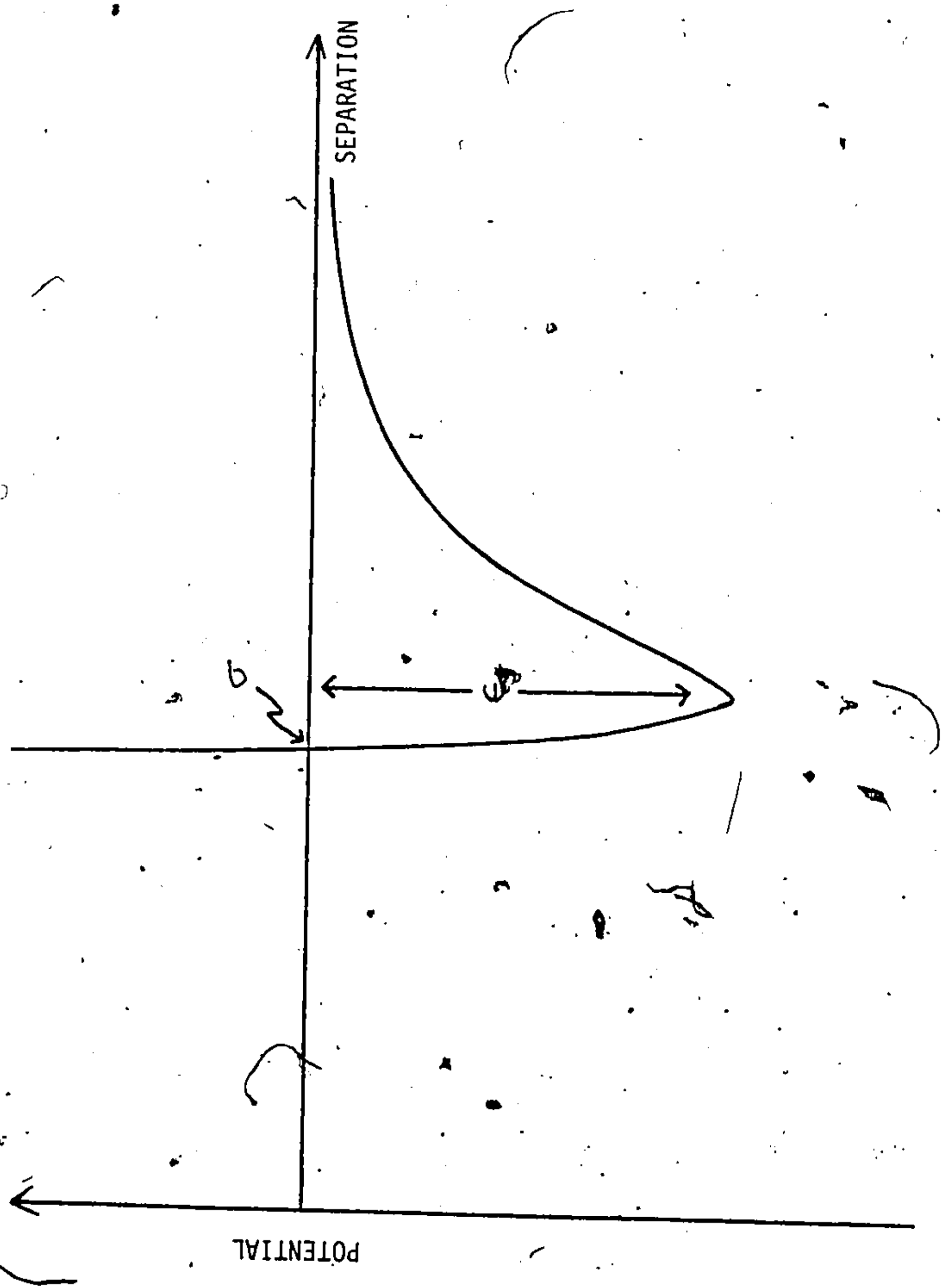
SEPARATION
POTENTIAL
b
φ

out parameters for the like atoms (carbon-carbon (C-C) or hydrogen-hydrogen (H-H)) and then to use the so-called combination rules (below) for the C-H parameters.

$$\sigma_{AB} = (\sigma_{AA} + \sigma_{BB})/2; \quad \alpha_{AB} = (\alpha_{AA} + \alpha_{BB})/2$$
$$\epsilon_{AB} = (\epsilon_{AA}\epsilon_{BB})^{\frac{1}{2}}; \quad C_{6AB} = (C_{6AA}C_{6BB})^{\frac{1}{2}}; \quad A_{AB} = (A_{AA}A_{BB})^{\frac{1}{2}} \tag{4.8}$$

The first of these is simply the mean of the size parameters, and the second is based on an approximate expression for the Van der Waals interaction (45).

4.2 Additivity

In the above discussion the interactions were pair-wise interactions. The total energy of a many body system would be the sum of all pair interactions. This assumption of pairwise additivity is only approximately valid. If there are at least three molecules, the short range interactions are not strictly pairwise additive. This can easily be seen from eq. (4.1) because the antisymmetrization operator can act on more than just pairs. Physically, the electron cloud of each molecule will be distorted by the presence of all the molecules near it, but this clearly cannot happen in a pairwise fashion. The long range electrostatic and 2nd order dispersion energies are strictly pairwise additive but the 3rd and higher order dispersion cannot be described as a sum of pair interactions. In these many body energies, the dispersion interaction between molecules A and B is mediated by a 3rd (3 body), or a 4th (4 body) and so on. In the three body interaction, molecule A induces a multipole in molecule C, which then interacts with molecule B.

The three body energy has been calculated in the multipole expansion (46). If only the dipole is considered, the term is known as the triple dipole energy (47) and has been shown to contribute significantly to the energy of a bulk system (2). But, in the adsorbed state, the small number of close triples reduces this energy to only 2% of the two body dispersion energy (48). The higher order multipoles make increasingly smaller contributions. In the light of the present knowledge of intermolecular potentials, these 3 body terms are typically not included.

In the presence of a surface, the interaction between two molecules is significantly altered by a 3 body interaction in which the surface plays the role of the mediating body. The surface mediated interaction (as it has come to be known) was first discussed by Sinanoglu and Pitzer (49), but the approach presented here is due to McLachlan (50). With a field susceptibility, linear response approach and the continuum approximation for the substrate, he showed that the dispersion interaction between two adsorbed molecules is altered by an amount ΔE:

$$\Delta E = \frac{1}{\pi 2R^3R'^3}(2 + 3\cos(2\theta) + 3\cos(2\phi))\int_0^\infty \alpha^2(i\omega)g(i\omega)d\omega$$
$$- \frac{3}{\pi R'^6}\int_0^\infty \alpha^2(i\omega)g^2(i\omega)d\omega \qquad (4.9)$$

where $g(i\omega) = (\varepsilon(i\omega) - 1)/(\varepsilon(i\omega) + 1)$.

This term is generally positive if the line joining the molecular centres is parallel to the surface and can be as large as 20% of direct dispersion interaction. $\alpha(i\omega)$ is the dynamic polarizability of the molecule and $\varepsilon(i\omega)$ is the dielectic constant of the solid at frequency

ω. McLachlan also showed that the dispersion interaction of a molecule with a surface can be considered as the interaction of the molecule with its own image in the substrate. In fact, the 3rd body in the substrate mediated interaction was the image of one of the molecules. Figure 4.2 illustrates the image plane and the coordinates of eq. (4.9).

A theoretical estimate of the position for the image plane was made by Zaremba and Kohn (51). They found that, for rare gases adsorbed on noble metals, the image plane should be placed half a lattice spacing above the surface defined by the nuclear centres. Although, graphite is metallic in the basal plane, it is not a noble metal, but, in the absence of a calculation specifically for graphite, the same theory is used for the position of the image plane.

The following approach in applying McLachlan's theory is due to Rauber et al. (52). Eq. (4.9) can be written in the form:

$$\Delta E = \frac{1}{6R^3R'^3}(2 + 3\cos(2\theta) + 3\cos(2\phi))C_{1s} - \frac{1}{R'^6}C_{2s} \qquad (4.10)$$

where

$$C_{1s} = \frac{3}{\pi}\int_0^\infty g(i\omega)\alpha^2(i\omega)d\omega \qquad (4.11)$$

and

$$C_{2s} = \frac{3}{\pi}\int_0^\infty \alpha^2(i\omega)dg^2(i\omega)d\omega \qquad (4.12)$$

In terms of these quantities the parameters in the dispersion interaction C_6 and C_3 can be written as:

$$C_6 = \frac{3}{\pi}\int_0^\infty \alpha^2(i\omega)d\omega \qquad (4.13)$$

$$C_3 = \frac{1}{4\pi}\int_0^\infty g(i\omega)\alpha(i\omega)d\omega \qquad (4.14)$$

Application of this theory requires a knowledge of the quantities $g(i\omega)$

Figure 4.2. The geometry for the substrate screened interaction; also shown are the image atoms (dashed).

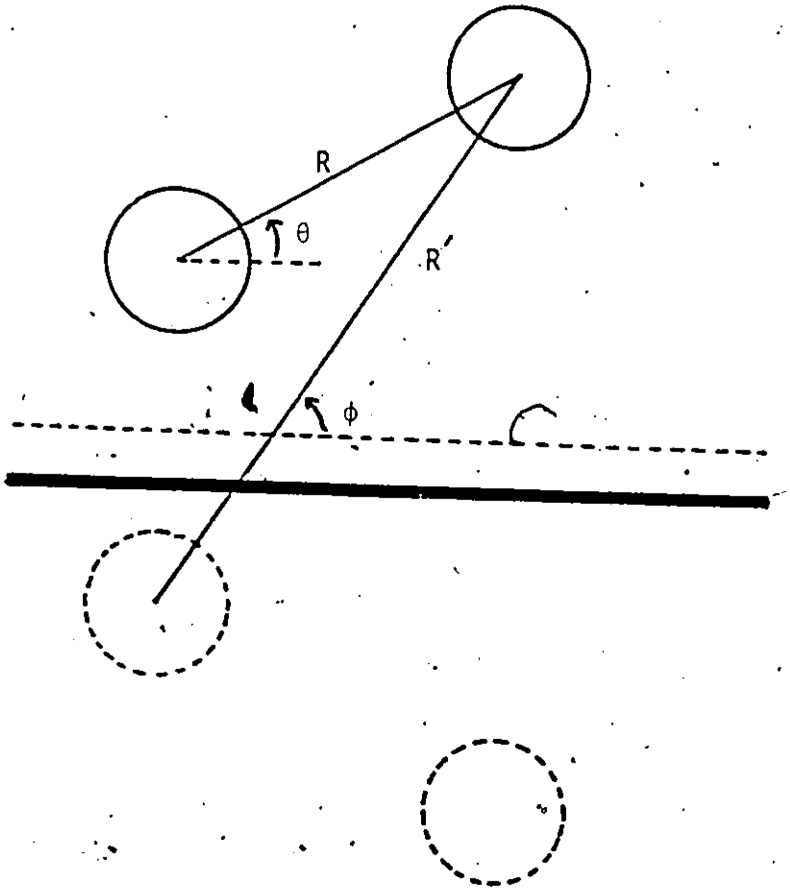
R
θ
R′
φ

and $\alpha(i\omega)$. Vidali and Cole (53) used Lorentzian approximations to calculate the long range dispersion interaction. Their approximations were used by Rauber et al. (52):

$$\alpha(i\omega) = \alpha_0/[1 + \omega^2/E_a^2], \tag{4.15}$$

and

$$g(i\omega) = g_0/[1 + \omega^2/E_s^2] \tag{4.16}$$

where E_a and E_s are characteristic energies of the molecule and the surface and α_0 and g_0 are static values. Substitution of eqns. (4.15) and (4.16) into eqs. (4.11), (4.13) and (4.14) yields

$$C_6 = \frac{3}{4}\alpha_0^2 E_a \tag{4.17}$$

$$C_3 = \frac{g_0 \alpha_0 E_s}{8(1 + x)} \tag{4.18}$$

$$C_{1s} = g_0 C_6 \frac{x(2 + x)}{(1 + x)^2} \tag{4.19}$$

$$C_{2s} = g_0^2 C_6 \frac{x(x^2 + 3x + 1)}{(1 + x)^3} \tag{4.20}$$

where $x = E_s/E_a$.

Values of α_0 and C_6 from experiment were used in fitting g_0, E_s and E_a for a variety of substrates and adsorbed molecules. These results for CO, ~~Xe,~~ and N_2 on graphite were used in the potential models outlined in the next chapter.

4.3 Molecule-Surface Interaction

For long range interactions in the continuum approximation, Lifshitz (54) found the result:

$$E = C_6/Z^3. \tag{4.21}$$

McLachlan (50) showed that this molecule-surface interaction can be considered as a molecule-image molecule interaction.

At short range, the atomic nature of the surface must be taken into account. By far, the most widely used model is the sum of a 6-12 potential over the atoms of the surface. The ordered surface and the $1/r^n$ form allows the sum to be performed as a Fourier series similar to the Ewald sum method that is used for ionic lattices. The sum for a 6-12 potential was performed by Steele (55):

$$V(r) = V_o(z) + \sum_{n>\text{[illegible]}} V_n(z) f_n(x,y), \tag{4.22}$$

$$V_o(z) = 4\pi\rho\epsilon_{AS}\sigma_{AS}^2 \sum_{p=0}^{\infty} \frac{1}{5}\left(\frac{\sigma_{AS}}{z_p}\right)^{10} - \frac{1}{2}\left(\frac{\sigma_{AS}}{z_p}\right)^4 \}, \tag{4.23}$$

$$V_n = \frac{2\pi\epsilon_{AS}\sigma_{AS}^6}{a_s} \left[\frac{\sigma_{AS}}{30}\left(\frac{g_n}{2z}\right)^5 K_5(g_n z) - 2\left(\frac{g_n}{2z}\right)^2 K_2(g_n z)\right]. \tag{4.24}$$

For molecules, the atom-atom approximation is used and the sum must be performed for each interacting site of the molecule. The subscripts AS refer to the interacting site (or atom)-surface. σ and ϵ are the 6-12 parameters. The quantity g_n is a surface reciprocal lattice vector, a_s is the surface unit cell area and the K_n's are modified Bessel functions. The index 'p' refers to the sum over the graphite layers with Z_p given by:

$$Z_p = Z_p + Pd$$

where d = 3.37 Å is the interplanar separation. For most molecules, including all those considered here, only f_1 needs to be included to obtain sufficient accuracy.

$$f_q = -2[\cos\frac{2\pi}{a}(x + \frac{y}{\sqrt{3}}) + \cos\frac{2\pi}{a}(x - \frac{y}{\sqrt{3}}) + \cos(\frac{4\pi}{a}\frac{y}{\sqrt{3}})] \qquad (4.25)$$

with $a = 2.46\ \mathrm{\AA}^2$. If, in the 6-12 model, one approximates the sum over the surface atoms with an integral the result is the 10-4 model. It is often used, but, it is a flat surface model and it can only be used where the surface corrugation is presumed not to be important. In addition, integration over the graphite planes yields a 9-3 potential, the attractive part of which has the Lifshitz $1/Z^3$ form. The 10-4 potential will be used to calculate Henry's law constants at high temperatures where the effects of corrugation are small.

It is interesting to note that, although at long range the concept of an image has been used, it plays no role in the 10-4, 6-12 or 9-3 models. The latter all assume that the interactions are centred about the nuclei.

A molecule-surface interaction in which the position of the image plane plays a crucial role is the electrostatic image potential. At long range, molecules possessing an electric multipole moment should produce an image moment in the surface. An ideal metal substrate would have an exact image, whereas, for a dielectric, in the continuum approximation, one would introduce a dielectric constant. It is the static response of the solid which is important here, and in this limit, graphite is considered to be a good metal (56). Typical distances of adsorbed molecules from the surfaces (defined by the nuclear centres) are 3.0 - 4.0 Å. At these small separations, the use of an image plane is questionable for two reasons. First, at close range, the corrugation of the surface will become important, but the concept of an image plane assumes a flat surface. A second point has to do with the calculation of image forces on graphite specifically. As in the case of substrate mediated interactions, the theory used for the position of the image plane is that due to Zaremba (51) which was worked out for noble metals. Graphite is laminar, and the electrons are not as mobile [illegible] perpendicular direction as they are in the plane. It seems unlikely that graphite could produce as good an image as a noble metal.

Bruch (56) calculated the image potentials for N_2 and CO_2 on graphite assuming point multipoles on the centre of mass and found the energy to be a significant fraction of the total of the interaction energy.

Calculations discussed in the next chapter will show that this approach to image forces breaks down when the multipole moments are large or distributed widely in the molecule. In these situations, the multipole centre is able to touch its own image. The remainder of this chapter will present in some detail those specific models employed in calculations.

4.4 N_2 Models

Nitrogen is second only to the rare gases in the effort that has been made in developing an intermolecular potential. It has yielded several models which have been tested against a broad spectrum of experimental data with some considerable success. The tests included the gas phase (second virial coefficients, viscosity), the liquid phase (thermodynamic properties, structure factors, diffusion coefficients) and the solid phase (lattice dynamics, sublimation energies, structure). Comparisons of many N_2-N_2 potentials can be found in Murthy et al (57) and Ling and Rigby (42). The latter authors suggest a model which was too complicated to be used in the calculations to be presented here and therefore two less accurate but simpler models were chosen.

The two N_2-N_2 potential models were due to Luty and Pawley (58) and Berns and van der Avoird (38). The Luty model is an atom-atom 6-exp model with the parameters fitted to the lattice dynamics of the solid. The parameters are given in Table 4.1. The model was used in only one calculation and was primarily intended to be compared to the following model.

Like the Luty potential the van der Avoird potential is an atom-atom 6-exp but also includes an electrostatic interaction in the form of distributed point charges. The dispersion constant was taken from ab initio calculations of Mulder et al (40). In these calculations, ab initio calculations of the anisotropic dispersion coefficients C_6, C_8 and C_{10} were combined with semi-empirical values of C_6 and experimental polarizabilities to form a model for the anisotropic dispersion interactions for nitrogen dimers. Three body interactions were not considered and the induction interactions were found to be very small. The van der Avoird dispersion term was found by fitting this anisotropic molecule-molecule potential to the C_6/r^6 atom-atom form.

The electrostatic interactions were approximated with four point charges (two pairs of equal magnitude but opposite sign) symmetrically placed on the molecular axis. The positions and magnitudes were fitted to the electrostatic energy from the multipole expansion up to the hexadecapole for 36 orientations of the dimer. The multipole moments were also taken from the calculations of Mulder et al (40).

Table 4.1

Atom-Atom Nitrogen Potential Models

$$V = B\exp(-\alpha \cdot r) - C_6/r^6$$

	Luty and Pawley	Berns and van der Avoird
Short Range		
B (kJ Mol^{-1})	2.050×10^5	7.70×10^5
α ($\mathrm{\AA}^{-1}$)	3.60	4.036
Long Range Dispersion		
C_6(kJ $\mathrm{\AA}^6$ Mol^{-1})	1803	1407
Long Range Electrostatic		
q (e), position (Å)	-	-.373, ±1.044
		+.373, ±0.847
Substrate Screening Parameters (from eq. 4.10-4.12)		
C_{1s} (kJ Mol^{-1} $\mathrm{\AA}^6$)	1922	
C_{2s} (kJ Mol^{-1} $\mathrm{\AA}^6$)	3683	

The parameters of the exchange term were found by fitting their own SCF calculations on 36 orientations of the dimer to an atom-atom exponential form.

The potential thus derived compares well with semi-empirical potential models fitted to gas phase data and therefore should provide an equally good description of angle averaged interactions. The authors also report good agreement with solid phase structural data (for two structures: cubic phase at 0 K and tetragonal phase at high pressure and 0 K), sublimation energies and lattice dynamics (59,38).

The substrate mediated interaction was calculated with the method and parameters due to Rauber et al (52). This is a molecule-molecule interaction with the force centres located at the centres of mass.

4.5 Hydrocarbon Models

These are almost exclusively atom-atom 6-exp type, with and without an electrostatic interaction. Several authors have presented models (43,44,60,61). The differences between the models lie in the treatment of the electrostatic interaction. The Williams approach is typical and his models seem to be the most often used in the literature. For this reason, it was chosen for the calculations (with altered electrostatic terms).

Williams chose an atom-atom 6-exp form. This model has nine parameters, three for each type of atom, C-C, C-H, H-H. The size parameters $\alpha_{CC} = 3.68\ \mathring{A}^{-1}$, $\alpha_{CH} = 3.74\ \mathring{A}^{-1}$, $\alpha_{HH} = 3.67\ \mathring{A}^{-1}$ were chosen at the outset. α_{CC} was taken from a calculation of the interplanar separation and compressibilities of graphite (62). α_{HH} was found by fitting ab initio calculations to the hydrogen dimer. The combination rules were used to find α_{CH}. The remaining six parameters B_{CC}, B_{CH}, B_{HH}, C_{CC}, C_{CH}, C_{HH} were fitted to the crystal structures and sublimation energies of many aromatic and non-aromatic hydrocarbons. In these fits the hydrogen atom centre was located 1.040 Å from the carbon atom for all molecules. The typical C-H distance is 1.110 Å from the hydrogen atom.

Williams also included electrostatic interactions in another series of fits in the form of point charges at the atomic sites. The magnitudes of the charges were included as parameters but the charge of the hydrogen atom was maintained equal and opposite to the charge on the carbon atom. The results of both fits are in Table 4.2. It should be noted that the charge distribution, if used in the C_2H_2 molecule, would give a quadrupole of only 57% of the value for the molecule in the gas phase. To alleviate this discrepancy, a new point charge distribution was determined which reproduced the long range quadrupole and hexadecapole moments as determined by SCF calculations (5). This electrostatic model is also described in Table 4.2. The quadrupole moment of C_2H_2 is almost five times that of N_2. In N_2 it has been shown that the electrostatic interaction is crucial to the proper description of the N_2-N_2 interaction. The electrostatic interaction should be extremely important in C_2H_2. Since the Williams model leads to a small quadrupole moment, the exchange and dispersion terms must make up the difference if this model is to be used for C_2H_2. One might, then, expect that simply tacking on a larger quadrupole would overestimate the binding energy. This turns out to be only partially true for a simple reason. In most hydrocarbon solids studied by Williams, the electrostatic contribution to the energy is not as large as in C_2H_2. This means that the Williams fits are primarily to the exchange and dispersion terms.

4.6 C_2H_2-C_2H_2 Model

The only potential model which has been developed specifically for C_2H_2 is due to Gamba and Bonadeo (GB) (16). It is also an atom-atom 6-exp model but with the electrostatic interaction described by four point dipoles on the molecular axis. The magnitudes and positions of the dipoles were adjusted to fit the quadrupole and hexadecapole moments. The parameters were fitted to the experimental sublimation energies, crystal structures, and lattice dynamics ($K = 0$) of the two solid phases, cubic and orthorhombic. The parameters varied in the fits were all nine 6-exp parameters, and an overall multiplicative constant for the electrostatic energy similar to a dielectric constant. The GB potential parameters are given in Table 4.2. This is the only potential which stabilizes the orthorhombic structure. Other models give the cubic structure at $T = 0$ K. Unfortunately, the value of the sublimation energy used in the GB fit did not include the heat of transition from the cubic phase to the orthorhombic phase. This has been measured to be ~ 0.6 kJ Mol^{-1} (63). A comparison of the observed and calculated values of the sublimation energies is given below. When the transition energy is included the fit is not very good.

Table 4.2

Atom-Atom Acetylene Potential Models

$$V = Be^{-\alpha R} - C_6/R^6$$

	Williams I	Williams II	GB
Short Range			
B_{CC} (kJ Mol^{-1})	350000	300000	1830000
B_{CH}	36000	60000	23000
B_{HH}	11000	12000	31000
α_{CC} (Å^{-1})	3.60	3.60	3.909
α_{CH}	3.67	3.67	3.703
α_{HH}	3.74	3.74	3.746
Long Range Dispersion			
C_{6CC} (kJ Mol^{-1} Å^6)	2386	1880	2029
C_{6CH}	525	562	418
C_{6HH}	115	168	1381
Electrostatic Models			
1) q (electrons), Z (Å)		+0.179, ±0.6035 -0.179, ±1.6625	
2) dipoles (eÅ), Z(Å)			±0.2667, ±0.528 ±0.0337, ±2.0
3) q (electrons), Z (Å)		+0.300, ±1.6625 -0.179, ±0.6035 -0.244, 0.0	
Substrate Screening			
C_{1s} (kJ Mol^{-1} Å^6)		8336.8	
C_{2s}		4463.5	

	Observed	Calculated
Cubic	5.6 kJ Mol^{-1}	6.0 kJ Mol^{-1}
Orthorhombic	6.9	6.3

Although the quadrupole and hexadecapole moments were fixed to the values from SCF calculations (5), the next highest moment was a free parameter. Gamba and Bonadeo found that it had an appreciable effect on the calculated frequencies, which improved as the size of this moment was increased from 10 to 24 $e\mathring{A}^6$. On the other hand, it was found that the lattice energies and constants did not change significantly if the five point charge model was substituted for the four dipoles. Since the former is much easier to calculate, it was used in the structure determinations to be described in the next chapter.

Although the GB model appears to be successful in the region in which it has been fitted, there are disturbing features in the exchange and dispersion terms. The dispersion parameter C_{HH} is almost as large as C_{CC} and larger than C_{CH}. These parameters are proportional to the polarizabilities of the relevant atoms and the polarizability for the carbon atom should be larger than that of the hydrogen atom. The parameter α is inversely proportional to the sum of the hard core radii of the interacting centres. An examination of Table 4.2 shows that Gamba's model has the carbon atom smaller than the hydrogen atom. Finally, the factor $E = 0.544$, which reduces the electrostatic energy by a factor of $E^2 = .3$, seems too high to be explained in terms of a dielectric constant or reduced multipole moments due to charge overlap effects.

The substrate-mediated interaction requires a knowledge of the dipole-dipole dispersion parameter C_6. This has not been calculated, so the value for Xe was used as an estimate. The isotropic 6-12 parameters for Xe and C_2H_2 are similar and one might expect that the values for C_6 are close. The method due to Rauber et al was used to calculate the substrate screening parameters. The value of the static polarizability was taken from SCF calculations (5). This term was small and therefore any errors in the use of the Xe parameters will not affect the results.

In the orthorhombic phase, the nearest neighbour C-H separation is only 2.73 Å with the molecules in a Tee configuration. This short distance has led to speculation about the occurrence of hydrogen bonding. SCF calculations (18) on the dimer have shown the Tee configuration to be the most stable and suggested a weak hydrogen bond. Neither of the models presented have any terms representing a hydrogen bond between the hydrogen atom and the centre of the triple C-C bond in the molecule. It would be difficult to include this interaction in a model applicable to many different situations. The large charge difference between the hydrogen atom and the centre of mass in the five point charge model does make the Tee configuration the most stable for the dimer in the Williams model.

4.7 Carbon Monoxide Models

Little research has been done on possible potential models for CO. Some early work (70) in lattice dynamics assumed that the interaction was similar to that of N_2, but this ignored the charge asymmetry found in SCF calculations (6). Recently, a lattice dynamical study of the cubic phase of CO yielded several asymmetric models, two of which are summarized in Table 4.3. The electrostatic parts (three point charges on the molecular axis) were fitted to the multipole moments found from recent SCF calculations (6). The exchange and dispersion terms were fitted to the lattice frequencies ($|K| = 0$) and cohesive energies. The molecules have three interaction centres, one on each atom and one at the centre of mass. Because the initial calculations with these models were disappointing, their use to study the adsorbed state was not pursued further.

A potential model developed in a manner similar to that applied to hydrocarbons was introduced by Mirsky (65). It was an atom-atom 6-exp potential with an added electrostatic interaction. The parameters of this model are also given in Table 4.3. The C-C parameters were fitted to the cohesive energies and elastic constants of many different hydrocarbon solids (60). The O-O parameters were fitted to the structures and cohesive energies of CO_2 in an atom-atom 6-exp plus point quadrupole model (66). The combination rules were used for the C-O parameters. The potential was used by Mirsky (65) to calculate various experimental results of dilute CO-Ar solid mixtures with reasonable success. The CO-Ar mixtures would not involve electrostatic interactions if they were sufficiently dilute and therefore the simple superposition of an electrostatic interaction is perhaps more reasonable here than in the Williams models. The same three point charge interaction was used as in the previous models.

The asymmetry in the dispersion interaction leads to an asymmetric

Table 4.3

Atom-Atom Carbon Monoxide Potential Models

$$V(r) = Be^{-\alpha r} - F(r)\left[\frac{C_6}{r^6} + \frac{C_8}{r^8} + \frac{C_{10}}{r^{10}}\right]$$

$$F(r) = \begin{cases} 1 & r > R \\ e^{-(1-r/R)} & r < R \end{cases}$$

	B (kJ Mol^{-1}Å)	α (Å^{-1})	C_6 (kJ Mol^{-1}Å^6)	C_8 (kJ Mol^{-1}Å^8)	C_{10} (kJ Mol^{-1}Å^{10})	R (Å)
Model 1						
C-C	32.58	3.269	3732	31288	280366	3.72
C-O	31.91	3.521	0	0	0	-
C-CM	-8.77	3.113	0	0	0	-
O-O	31.15	3.505	0	0	0	-
O-CM	-7.84	3.333	0	0	0	-
CM-CM	0.27	2.971	1561	13092	117307	3.72
Model 2						
C-C	10.15	3.41	1908	0	0	-
C-O	9.88	3.41	0	0	0	-
C-CM	0	0	1410	0	0	-
O-O	20.10	3.34	0	0	0	-
O-CM	0	0	1017	0	0	-
CM-CM	0	0	1937	0	0	-
Mirsky						
C-C	3.00	3.68	1761			
C-O	3.17	3.91	1420			
O-O	3.25	4.18	1085			

Electrostatic (used in all models)

q (electrons), Z (Å)		
	-0.636,	-1.0820
	0.831,	-0.6446
	-0.195,	0.3256

...... continued

Table 4.3 (continued)

Substrate Screening

	C_{1s} (kJ Mol^{-1}Å^6)	C_{2s} (kJ Mol^{-1}Å^6)
C-C	709.7	373.4
C-O	557.6	293.4
O-O	438.1	230.5

C-Carbon; O-Oxygen; CM-Centre of Mass

Origin is at the centre of mass

Carbon is at -0.6446 Å

Oxygen is at +0.4836 Å

substrate mediated interaction. Again the method of Rauber et al (52) was used to calculate the substrate mediated parameters. The value of C_6 and the static polarizability for a CO molecule were taken from the calculations of Jhanwar and Meath (67) and of Amos (68), respectively. The molecule-molecule parameters were then $C_{1s} = 2263$ kJ Mol^{-1}Å^6 and $C_{2s} = 1192$ kJ Mol^{-1}Å^6. Conversion to atom-atom parameters was effected by assuming that they were in the same ratio as the C_6 atom-atom parameters of the Mirsky model. The resulting parameters are listed in Table 4.3 and were used in all of the CO-CO models.

4.8 Molecule-Surface Interactions

The molecule-surface interactions were calculated with one of two procedures, either by a Fourier (if a corrugated surface was required) or a 10-4 method.

C_2H_2:

The atom-atom 6-exp parameters for C-H and C-C from the Williams model were fitted to a 6-12 form by comparing the separation at zero potential (σ) and the well depth (ϵ). The image interaction, if used, was simply superimposed on the above terms.

CO:

The Mirsky atom-atom 6-exp C-C and O-O parameters were fitted to a 6-12 form as in C_2H_2. The graphite 6-12 parameters were taken from calculations of the interplanar separation and compressibilities of graphite (62), $\sigma = 3.4$, $\epsilon = 28$ K. Combination rules were used to find the C-graphite and O-graphite parameters.

N_2:

The N-graphite potential was developed by Steele (55) by combining 6-12 N_2-N_2 parameters and the 6-12 graphite parameters. The N_2-N_2 parameters were fitted to experimental thermodynamic and structural properties of the liquid in molecular dynamics simulations (69).

The molecule-surface parameters for C_2H_2, CO and N_2 are displayed in Table 4.4.

Table 4.4

Atom-Atom Molecule/Graphite 6-12 Parameters

$$V = 4\varepsilon\left[\frac{\sigma^{12}}{r^{12}} - \frac{\sigma^{6}}{r^{6}}\right]$$

C_2H_2	
σ_{CS} (Å)	3.45
σ_{HS} (Å)	2.88
ε_{CS} (K)	47.97
ε_{HS} (K)	25.09
CO	
σ_{CS} (Å)	3.39
σ_{OS} (Å)	3.14
ε_{CS} (K)	33.42
ε_{OS} (K)	41.52
N_2	
σ_{NS} (Å)	3.36
ε_{NS} (K)	31

CHAPTER FIVE

RESULTS II

5.1 Monte Carlo Methods and Techniques

The statistical mechanics of many body systems often involves integrals over a large number of variables. For example, in the canonical ensemble the average energy is:

$$U = \frac{\int U(q_1 \ldots q_n) e^{-U(q_1 \ldots q_n)/k_B T} dq_1 \ldots dq_n}{\int e^{-U(q_1 \ldots q_n)/R_B T} dq_1 \ldots dq_n} \tag{5.1}$$

where q_i describes the coordinates of each particle in the system. The straightforward numerical evaluation of the integrals of eq. (5.1) is not possible. It has been long known (71,72) that the Monte Carlo procedure is much faster. In its most basic form, one averages the integrand over a randomly chosen set of points in the coordinate space. This method works well if the integrand does not vary too rapidly. The Boltzmann factor in eq. (5.1) varies very rapidly and an extremely large number of points is needed to obtain sufficient accuracy. The biased sampling procedure, first introduced by Metropolis et al (73) reduces the number of samples needed. The ensemble average can be rewritten as:

$$\langle A\rangle = \frac{\int \frac{1}{p} A(q) e^{-U(q)/k_BT} dq}{\int \frac{1}{p} e^{-U(q)/k_BT} dq} \qquad (5.2)$$

where p can be any probability distribution. Metropolis et al chose the Boltzmann distribution itself for p which results in:

$$\begin{aligned} A &= \int A(q)dq/\int dq \\ &= \sum_v A(q_v)/\sum_v 1 \\ &= \frac{1}{M}\sum_v A(q_v) \end{aligned} \qquad (5.3)$$

where q_v is the v^{th} point in the sampled set. The method of Metropolis et al (73) is not just to sample randomly the coordinate space but to bias the random sampling with the Boltzmann distribution which helps to ensure that the sampled set of points significantly contributes to the integral (eq. 5.1).

To implement the method, the energy of the system is calculated at an initial position (q). The coordinates of one or more particles are changed to (q) ± (Δq) where the (Δq)'s are randomly chosen increments ranging up to a previously selected maximum value. The energy of the new position is evaluated and the Boltzmann factor exp(-ΔE/kT) is compared to a random number between 0-1. If the Boltzmann factor exceeds the random number, the move is accepted, otherwise, the move is rejected. If the move is accepted, the new position is used in the average (eq. 5.3), but, if it is rejected, the old position is put into the average again. In this way, the system evolves towards classical thermodynamic equilibrium.

5.2 Size Effects

A real system involves a very large number of particles but this is not a realistic choice in simulations. The largest simulation published used 100,000 Xe atoms (74). The interaction potentials between Xe atoms are simpler than those to be discussed here. It was desired to test several model potentials on three different systems, therefore the system size had to be quite small.

The magnitude of size effects varies with the number of particles, and acts to decrease the fluctuations in the system.

5.3 Surface Effects

In a small system the number of particles on or near the surface can be a large fraction of the total. The environment for these particles is very different from those in the bulk. Periodic boundaries greatly reduce surface effects but at the expense of introducing a false periodicity into the system. This can be very important in small systems. For example, if the natural periodicity is incommensurate with the boundaries, the structure could be frustrated. In adsorption on a periodic substrate, the boundaries should be maintained commensurate with the substrate.

5.4 Interaction Range

All of the potential models of Chapter 4 are of the long range $1/r^n$ form, and therefore, every molecule interacts with the entire system. Including every pair interaction in the energy was unfeasible and unnecessary and so two cutoff radii were used. Up to the first cutoff, the full anisotropic potential model was used but, between the two cutoff radii, the calculations employed an approximate orientationally-averaged potential. The effect of the procedure on the energy was less than the uncertainty in the model while the saving in computer time was substantial.

5.5 Sampling

The procedure for determining which particle to move and the maximum increment Δq is part of the probability distribution over which one is sampling. If the increment is very small, then ΔE will be small and most moves will be accepted but the system will be slow to reach equilibrium. By contrast, a large increment will result in a low acceptance rate but the system will again be slow to reach equilibrium. A given system will have some optimum increment size which is not known a priori. A rule of thumb is to choose the increment size to produce an acceptance rate of 50%. This can be done through short test runs or by monitoring the acceptance rate during the run and periodically adjusting the increment size. In situations where the energy dispersion is large, such as at high temperatures or in clusters where the surface molecules have higher energies, the acceptance rate can be monitored for each molecule individually. A different method for handling large energy dispersion has been suggested (75). Here, the increment size is biased by the factor $Ae^{B(E-\langle E\rangle)}$ where $\langle E\rangle$ is the running average energy. High energy particles are then given large increments. The authors (75) found that by optimizing the parameters A and B, the procedure was substantially faster in reaching equilibrium in the high dispersion systems studied. In the systems to be discussed here, the dispersion was not particularly large and it was found that this method was not faster in producing equilibrium than monitoring the acceptance rate for each molecule separately.

5.6 Methods

Two general methods were employed in the calculations. The first was to place 64 molecules in periodic boundaries (commensurate with the substrate) and to allow each molecule to move separately.

The second method was to assume a unit consisting of four molecules and to replicate this unit periodically to form a solid cluster, Figure 5.1. The height and orientation of each molecule, the lattice vectors L_1 and L_2 and the position of the origin were allowed to vary separately. The lattice vectors could also be changed under the restriction of constant area defined by $L_1 \times L_2$. This four sublattice method can only produce ordered solid structures which have no more than a four molecule basis.

5.7 Henry's Law Constants

Henry's Law constant, which is the slope of an isotherm in the limit of zero density, probes the interaction of a single molecule with the surface. With the assumption of a flat (uncorrugated) surface, Henry's Law constant (K_H) is given by:

$$K_H = \frac{A}{2k_BT} \int_0^{z_0}\int_0^{\pi} \sin\theta\left(e^{-\phi(z,\theta)/k_BT} - 1\right)d\theta dz \qquad (5.4)$$

where $\phi(z,\theta)$ is a model potential, z is the height of the centre of mass above the surface, θ is the tilt angle from the normal to the surface, and A is the total surface area. This section deals with the evaluation of K_H for a standard 10-4 potential model and the attempts to refine

Figure 5.1. The unit consisting of 4 molecules which was replicated to form a solid cluster.

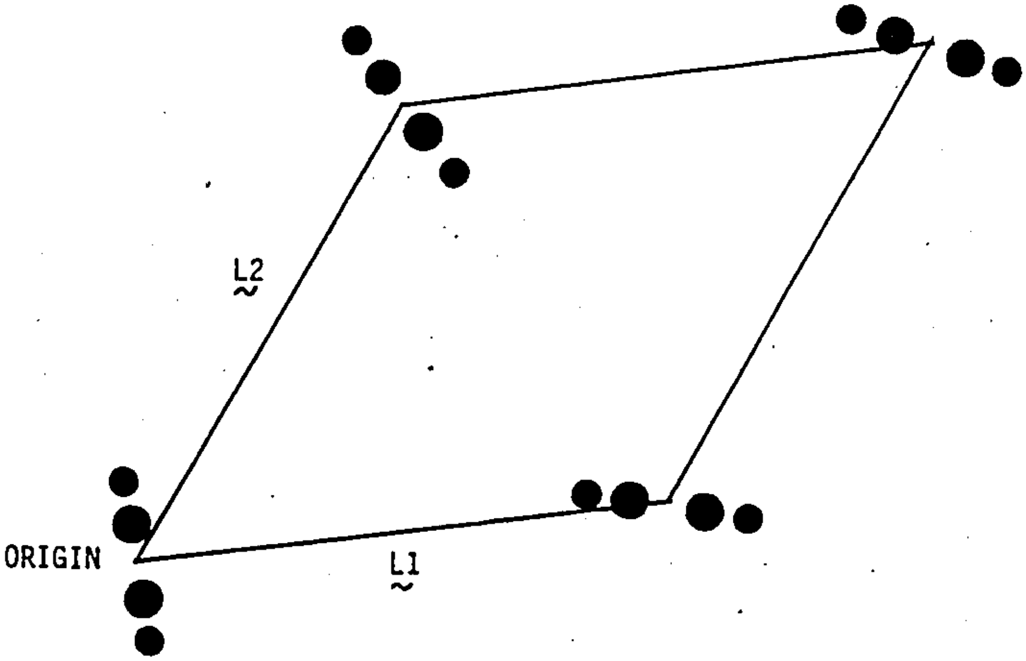
L2
ORIGIN
L1

the parameters of the model to fit the experimental data of sec. 3.4.

The atom-surface 10-4 model (eq. 4.23) is the atom-atom 6-12 potential integrated over the surface atoms, and it results in a flat surface model. The approximation of a flat surface at the experimental temperatures (> 155 K) is very good because the maximum corrugation typically obtained from the 6-12 model is ∼ 80 K and ∼ 20 K for C_2H_2 and CO respectively.

The double integral involved in the expression for K_H is not analytic and it was evaluated numerically with Simpson's rule. The experimental results for C_2H_2 and CO are presented in Table 5.1. The values of q_{ST} were derived from the temperature dependence of K_H (eq. 3.5). The first potential tried was that of Williams (set IV) fitted to a 6-12 form. This and potentials very similar to it are the most commonly used potentials for hydrocarbons. The results of the fit are illustrated in Table 5.2. The calculated value of q_{ST} agrees with experiment quite well but K_H is larger than experiment by more than a factor of 2-3. The 6-exp form of the Williams model yielded essentially the same results. In some sense, K_H is a measure of the allowed phase space. The Williams type potentials seem to allow the molecule too much freedom over the surface. There were no other potentials available and so the method was checked by applying it to the CO/graphite system. The Mirsky potential (Table 4.3) as fitted to a 6-12 form but with the values of ε_{CS} and ε_{OS} scaled up by 5% was used in the calculations. The calculated results are compared with the experimental ones in Table 5.1. The comparison is obviously quite satisfactory and so it is felt that the disagreement in the case of C_2H_2 is caused by the potential and not by

Table 5.1

Henry's Law Constants and Isosteric Heats of Adsorption

	Temperature	$K_H \times 10^4$ (exp)	$K_H \times 10^4$ (calc.)
$\underline{C_2H_2}$			
	183.76	.95 ± 0.04	-
	182.70	1.02	-
	173.85	2.04	5.92
	163.86	4.44	
	154.33	12.00	
q_{ST}		19.4 ± 0.5	19.4
CO			
	102.39	6.9 ± 0.2	7.1
	94.27	21.30 ± 0.05	21.9
	85.66	91 ± 2	91.8
	84.02	122 ± 2	123.2
q_{ST}		11.25 ± 0.3	11.3

Table 5.2

Fitted Values of the 10-4 Parameters for C_2H_2/Graphite

	ε_{CS}	σ_{CS}	ε_{HS}	σ_{HS}
(1)	59.1	2.72	40.8	2.875
(2)	49.2	2.73	47.4	2.99
(3)	70.9	2.60	43.1	2.60
(4)	65.71	2.76	31.6	3.10
(5)	-0.60	3.35	92.6	2.88
Williams	48.0	3.45	25.1	2.88

the method.

A refinement of the 10-4 parameters was made with a non-linear IMSL routine (ZXSSQ). The quantities fitted were q_{st} and K_H at 173.86 K. Many fits were found depending on the initial values given to the parameters. Occasionally, an initial set would result in the program running off into some completely non-physical region of parameter space where it was unable to find a fit in a reasonable number of iterations. In these cases, a new set of initial values was given. In all of the fits, the final set of parameters (Table 5.2) had the same physical significance. There are four important differences between these parameters and the Williams parameters (also in Table 5.2).

The well depth for a 10-4 potential is proportional to $\varepsilon\sigma^2$. The fitted parameters all have well depths for the hydrogen atom up to 50% larger than those for the Williams parameters.

In 4 of the 5 fits, the value of σ_{HS} is greater than or equal to σ_{CS} which implies that the hydrogen atom is equal to or larger than the carbon atom.

SCF calculations (88) show that the outer charge density contours of an acetylene molecule are egg shaped. In an atom-atom potential model these outer charge density contours approximately determine the hard core repulsive distances, σ. The shape of an acetylene molecule can be represented with $\sigma_H < \sigma_C$.

When σ_{HS} and σ_{CS} were fixed to values close to the Williams values, the value of ε_{CS} approached zero (no interaction at all).

All of the fitted potentials resulted in the molecule lying less than 3 Å from the surface (defined by the nuclear centres) and more restrained to lie flat on the surface than in the Williams model.

An image force could be used to explain each of these points. If a point charge model is assumed to describe the charge distribution, (eg. the 5 point charge model of Table 4.2), the image force would be purely attractive and would push the molecule closer to the surface. The carbon atoms which usually sit in the potential minimum in the Williams model would be pushed out of the minimum towards the repulsive region of the potential. The hydrogen atoms which usually sit too high would be pushed towards the potential minimum. The increased attraction at the ends of the molecule would come from the image force and the hydrogen atoms. Since the molecule now lies closer to the surface, the repulsive part of the 6-12 potential is more effective in preventing the molecule from tilting.

All attempts to calculate the image force, using the theory outlined in Sec. 4.3 and the five point charge model, resulted in one of the outside charges touching its own image. A point quadrupole at the centre of mass resulted in the same catastrophe. It appears that the image force is far too large if the image plane is raised above the surface. The magnitude of the image force reinforces the objections to the use of an image plane in these systems which was mentioned in Sec 4.3.

5.8 The Solid Phases of Adsorbed Acetylene

Acetylene adsorbed on graphite has been shown to have two different solid structures (19,20). The areas have been determined from isotherm data to be 18.9 ± 0.5 and 15.7 ± 0.3 $\mathring{A}^2$/molecule. Neutron diffraction studies have been made and the structures of Figure 3.4 proposed. These experiments were performed at two temperatures 57 K and 120 K. The results are displayed in Table 5.3. With only two Bragg peaks one cannot obtain a unique structure and the proposed structures were made with no basis assumed. The next two sections will present Monte Carlo simulations of the solid structures at 0 K which employ the two C_2H_2-C_2H_2 potential models of Table 4.2 and two C_2H_2-surface potential models of the previous section.

5.9 Low Density Solid

The simulation of the low density structure employed the 4 molecule method at 5 K with the area free to change. This method was necessary to match the areas in the simulations to those corresponding to the isotherm data.

The C_2H_2-C_2H_2 GB potential model with the C_2H_2-surface model of Williams was the first to be tried and yielded the structure in Fig. 5,2. This is a very slightly incommensurate $1\times\sqrt{3}$ herringbone with the molecules lying flat on the surface. This structure does not reproduce the diffraction Bragg peaks of solid I. The energy of the structure is 32 kJ Mol^{-1}, which is not in agreement with the value of the integral heat, 27 kJ Mol^{-1}, found from isotherms. The Williams model reproduced the single particle adsorption energy and, therefore, we conclude that it is the GB potential which gives too much binding energy.

The next attempt was with the Williams C_2H_2-C_2H_2 and C_2H_2-graphite models and the resulting structure is shown in Figure 5.3. This is a square nearly tee structure (P_{2gg} space group) with the molecules lying flat on the surface and a lattice spacing of 4.45 Å. This space group reproduces the diffraction Bragg peaks, but the area of 19.9 Å^2/molecule is larger than the value of 18.9 ± 0.5 Å^2/

Table 5.3

Neutron Diffraction Data

Coverage	Bragg Angle (Deg)	Coherence Length (Å)	Intensity
0.65	16.9	200	93
	27.35	120	175
0.89	17.03	150	122
	27.60	120	216
1.24	19.3	120	152
	26.75	200	280
1.54	19.9	120	152
	26.77	200	280

Figure 5.2. Result of the low density solid C_2H_2 simulation using the potential due to Gamba and Bonadeo. The (+) signs denote the carbon atoms of the graphite substrate. The dashed lines indicate the replicated unit.

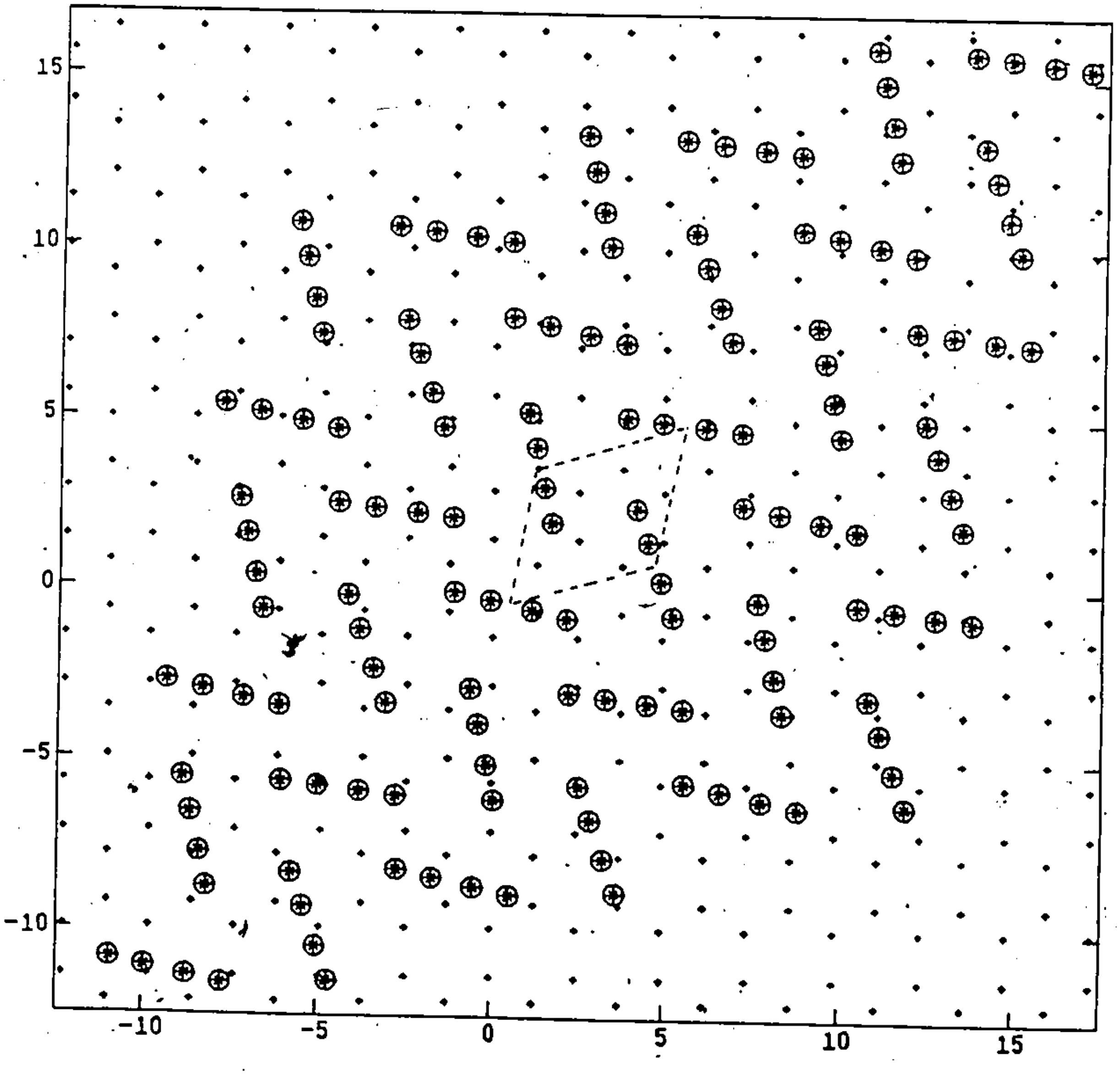
15
10
5
0
-5
-10
-10
-5
0
5
10
15

Figure 5.3. The result of the low density solid C_2H_2 simulation using the potential due to Williams and the 5 pt. charge model. The (+) signs denote the carbon atoms of the graphite substrate. The dashed lines indicate the replicated unit.

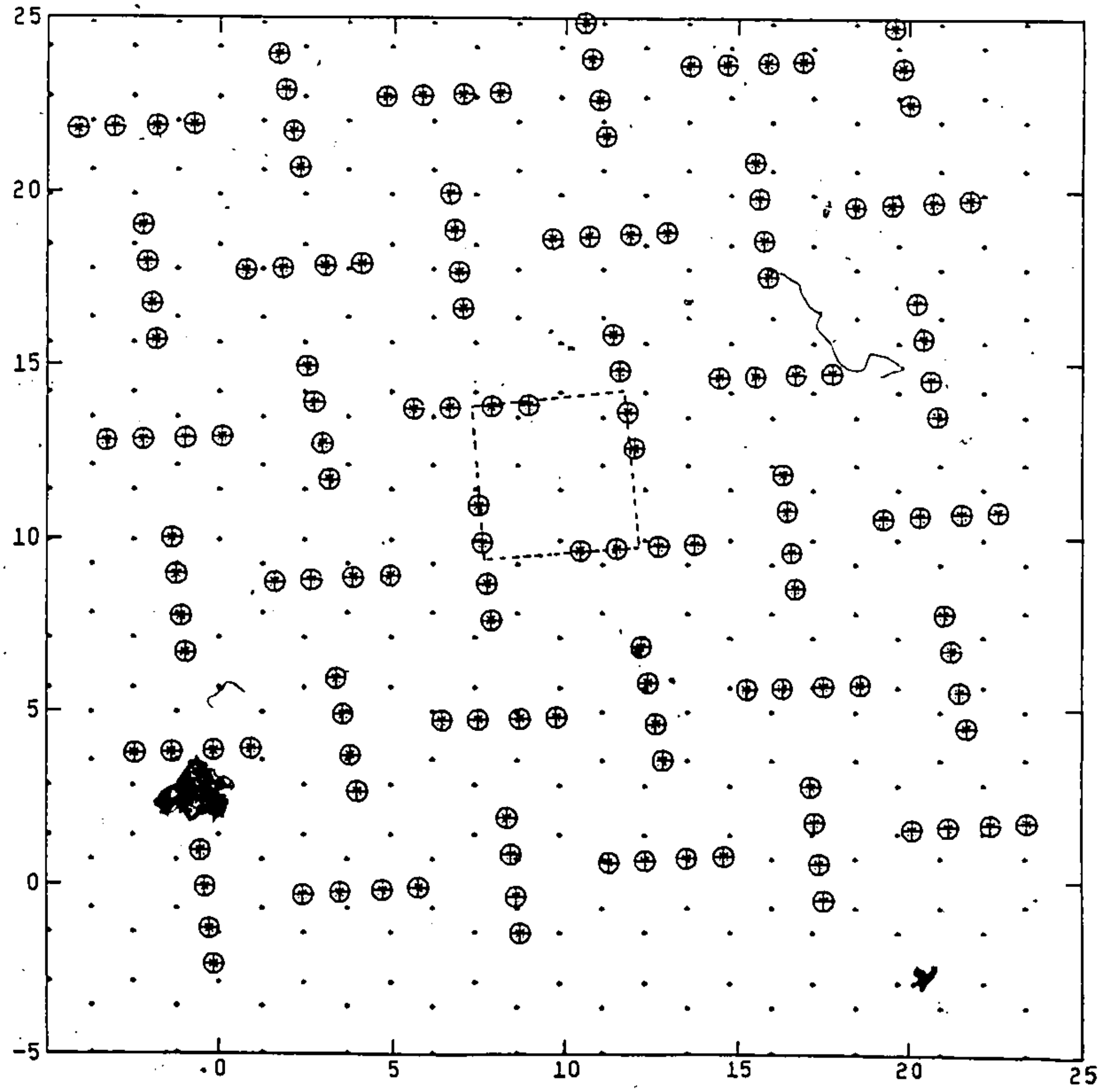
25
20
15
10
5
0
-5
0
5
10
15
20
25

molecule found from the isotherms. The energy is also too high (32 kJ Mol^{-1}) as in the case of the GB model. To reduce the energy the magnitude of the quadrupole was lowered by 16%, which reduced the electrostatic energy by 30%. As was discussed previously, a reduction of the electrostatic moments (from the gas phase values) in condensed systems is often necessary to obtain a fit to experimental data. A reduction of 16% is not as large as many authors have suggested.

The reduction of 16% introduces a factor of $\sqrt{.7} = .84$ into the electrostatic potential similar to but smaller than the factor of $\varepsilon = .544$ in the GB model. The simulation employing the factor of $\varepsilon = \sqrt{.7}$ and Williams C_2H_2-C_2H_2 and C_2H_2-graphite models yielded the structure of Figure 5.4. This is an incommensurate $1 \times \sqrt{3}$ herringbone structure which does not reproduce the neutron Bragg peaks, but the energy of 27 kJ Mol^{-1} agrees with the experimental value. The molecules in Figure 5.4 are tilted 20° from the surface. The ends tilted from the surface are indicated by the arrows. Williams C_2H_2-graphite potential did not fit Henry's Law constants because it allowed the molecule too much freedom to tilt on the surface. The same C_2H_2-C_2H_2 potential but now with a C_2H_2-graphite potential which fit K_H, set #2 of Table 5.2, resulted in the structure of Figure 5.5. This is, again, a square nearly teed lattice with the molecules lying flat on the surface and a lattice spacing of 4.55 Å, larger than in the previous square lattice. It fits the experimental diffraction data. While the energy of 28 kJ Mol^{-1} agrees with experiment the area of 21 $\mathrm{Å}^2$/molecule is too low. No other models for the low density structure were tried.

Figure 5.4. The result of the low density C_2H_2 solid using the potential due to Williams and the 5 pt. charge model with the quadrupole moment scaled down by 16%. The (+) signs denote the carbon atoms of the substrate. The dashed lines indicate the replicated unit.

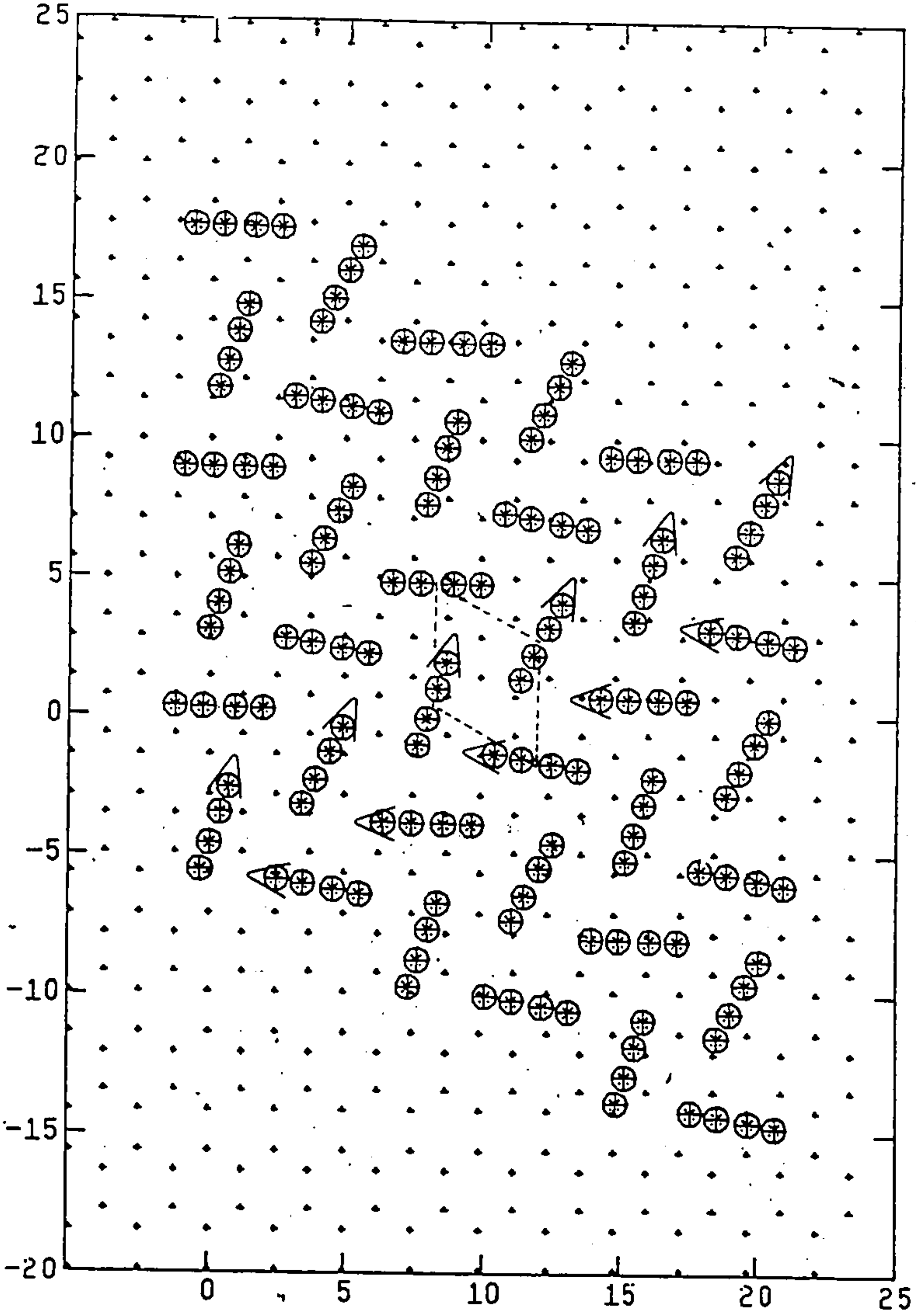
25
20
15
10
5
0
-5
-10
-15
-20
0
5
10
15
20
25

Figure 5.5. The result of the low density C_2H_2 simulation using the potential due to Williams and the 5 point charge model with the quadrupole moment scaled down 16% and a potential to the surface which fit q_{ST} and k_H. The (+) sign denotes the carbon atoms of the graphite substrate. The dashed lines indicate the replicated unit.

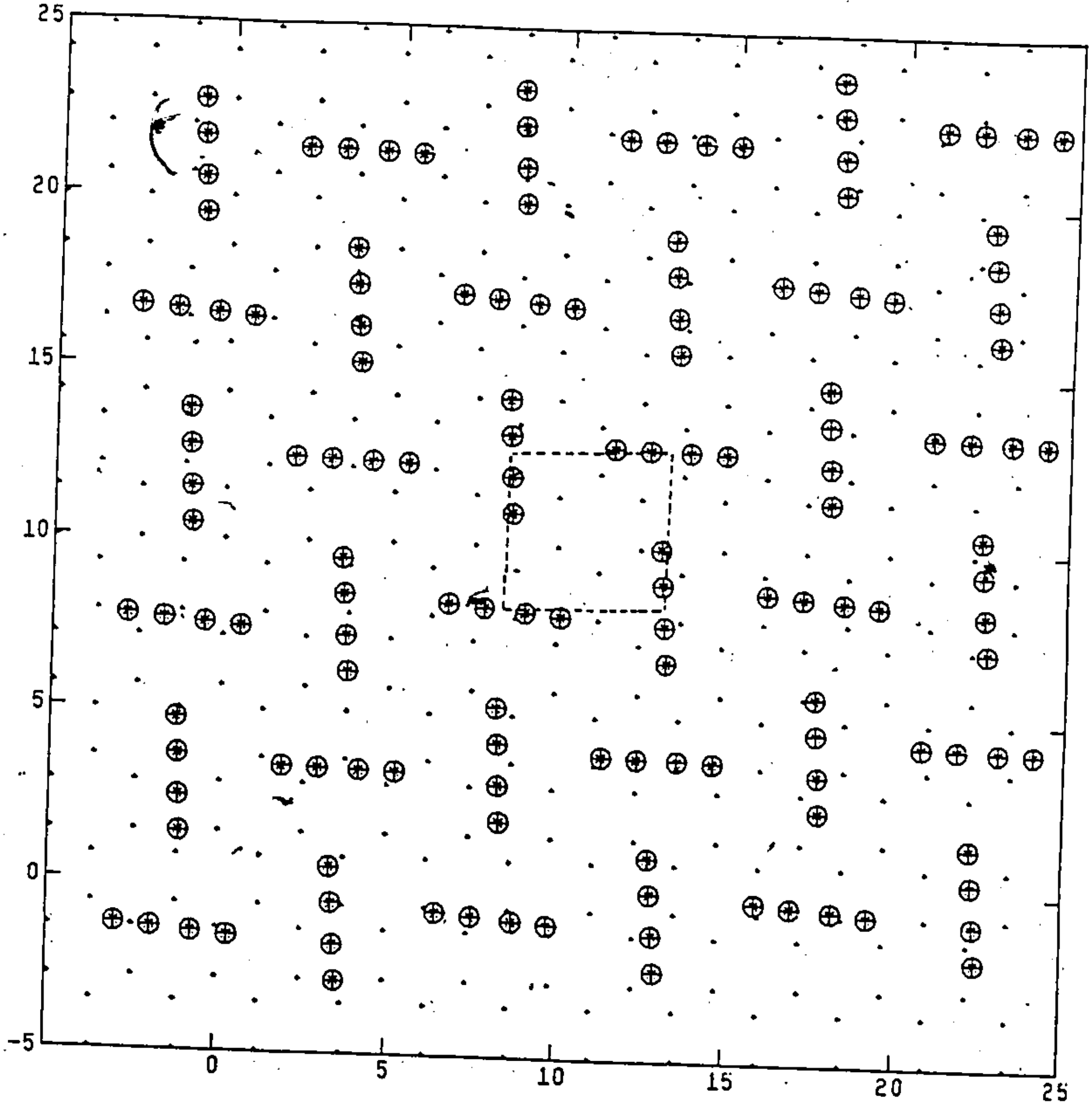
25
20
15
10
5
0
-5
0
5
10
15
20
25

In summary, two structures were found, a $1\times\sqrt{3}$ herringbone and a square tee. The herringbone does not reproduce the Bragg angles nor the relative intensities, as will be shown in the next section. It will be proposed that this is the high density structure. The square nearly teed lattice can reproduce the neutron data. Its structure (Figure 5.5) has a nearest neighbour separation of 4.55 Å and the average deviation from a tee orientation is ∿ 3°. The Bragg angles, plane separations, and relative intensities for a square P_{2gg} lattice (Figure 5.6A) were calculated for several n.n. distances and deviations from the perfect tee orientations. The best fits were found for a n.n. distance of 4.33 Å and a 0° deviation. These results and the results from similar calculations on the simulated structures are given in Table 5.4. The relative intensities were calculated on the assumption of a 2D powdered sample. The necessary structure factor and multiplicities were taken from the International Table on Crystallography. Table 5.4 shows results for only the main peaks. All other peaks have either low structure factors or are at high angles where the geometric factors quickly reduce the intensities.

The simulated structure differs from the structure corresponding to the best fit primarily in the lattice parameter (3.5 - 6%). In the simulated structure the hydrogen atoms are pointing somewhat towards the carbon atoms and away from the centre of mass. This also occurs in the a,b plane of the orthorhombic lattice, where the n.n neighbour separation is 4.31 Å, which is very similar to the best fit.

5.10 High Density Solid

Simulations of the high density structure required the use of

Figure 5.6A. The P_{2gg} unit cell which gives the square-tee structure.

Figure 5.6B. The P_{2gg} unit cell which gives the $1\mathrm{x}\sqrt{3}$ herringbone structure.

A

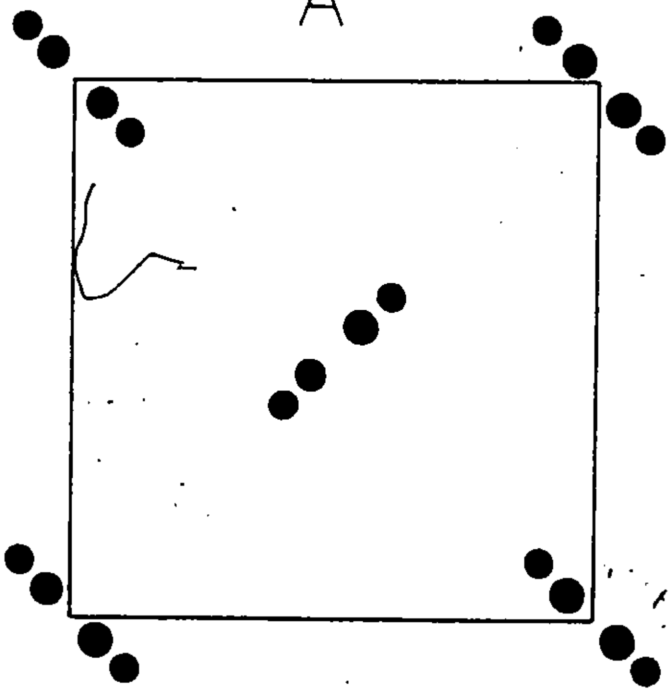

B

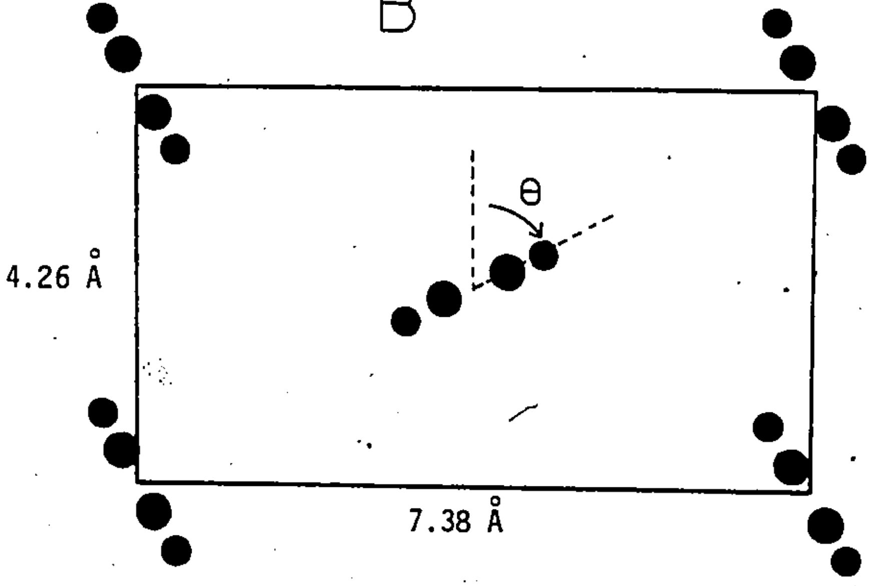

Table 5.4

Low Density Structural Fits to the Neutron Data

	Exp.	Best Fit	Simulated	
Bragg Angle (Deg)	16.9	16.9	16.1	16.5
	27.35	27.35	25.9	26.6
Plane Separation (Å)	4.33	4.33	4.55	4.45
	2.74	2.74	2.88	2.82
Intensity	93			
	175			
Relative Intensity	1.88	2.00	2.28	2.37

either the four molecule method at fixed area or periodic fixed boundaries because the structure was only stable under pressure.

The initial configurations for the simulations were either the diffraction based proposal (Figure 3.4B) or the same centre of mass structure but with random orientations.

All of the models yielded a 1x√3 herringbone structure (P_{2gg} Figure 5.6B and 5.7). The GB model was not tried since it already had resulted in a 1x√3 herringbone which was only very slightly incommensurate at zero pressure. It was felt that the introduction of commensurate boundaries at the 1x√3 commensurate density would make no difference.

Only the tilt angle of the molecule from the surface was different. The Williams C_2H_2-C_2H_2 potential with no reduction of the quadrupole gave the structure of Figure 5.7. Here, the tilt angle is ~20° (the raised end is indicated by the arrows). Reduction of the quadrupole caused the angle to increase to ~ 25° with no other changes. The structure has been labelled 'the 2-out structure' by Harris and Berlinsky (76) who made a mean field study of possible structures of N_2-like molecules adsorbed on graphite. Substitution of the molecule-surface potential for set #2 of Table 5.2 (fits to K_H and q_{ST}) reduced the tilt angle to only ~11° and destroyed the order in the tilting angles.

The results of the same structural analysis which were made for the low density case are displayed in Table 5.5. Many fits to the neutron data were obtained by varying the relative orientations and tilt angles of the molecules. The results in Table 5.5 are for the simulated structures. None of the simulated structures fits the diffraction data because a peak at a Bragg angle of 36.5° (h,k = 1,3 and 2,0) has an

Figure 5.7. The result of the high density C_2H_2 solid simulations. The arrow represents the end of the molecule which is tilted out of the plane and the dashed lines outline a unit cell of the P_{2gg} structure.

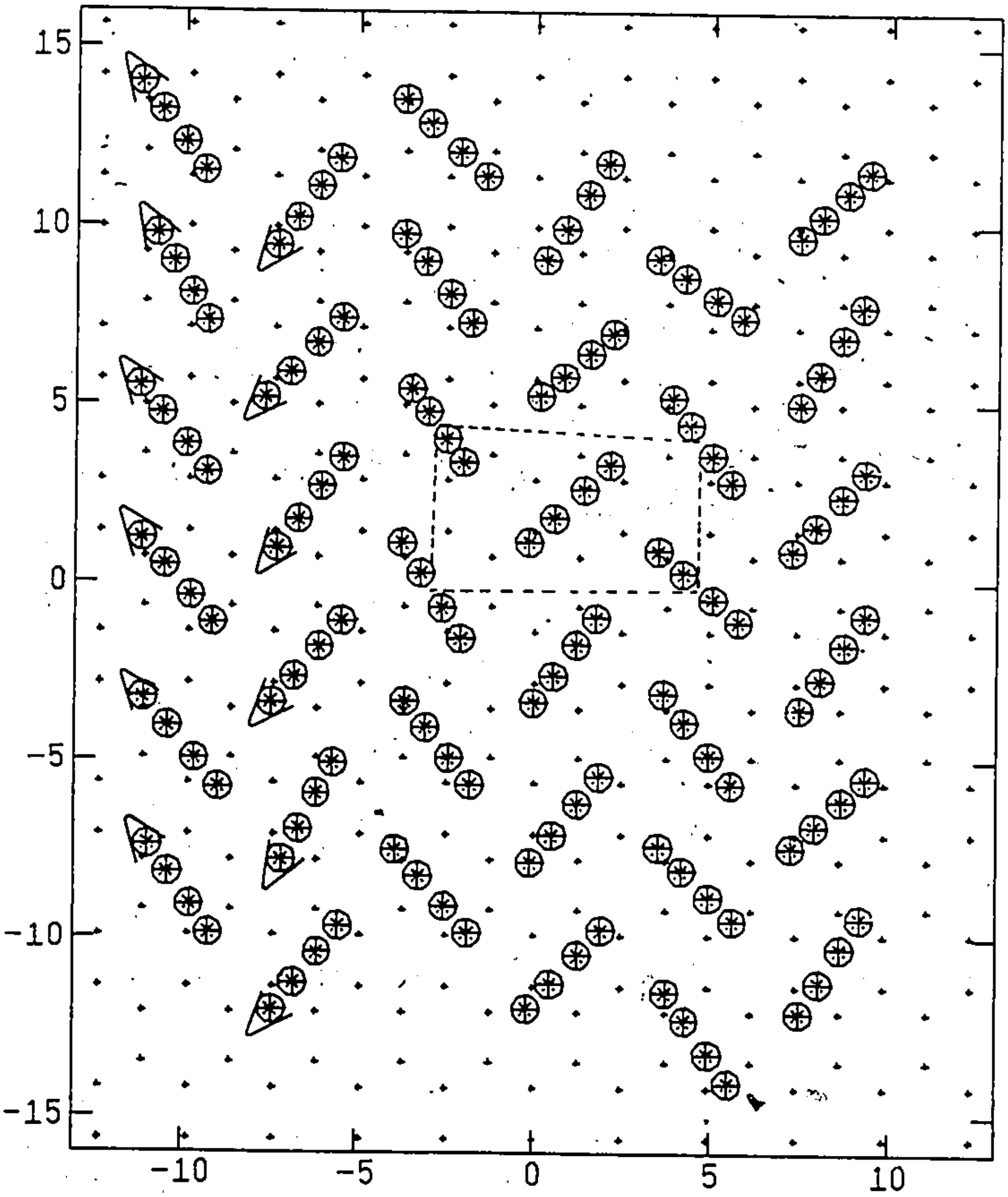
15
10
5
0
−5
−10
−15
−10
−5
0
5
10

Table 5.5

High Density Structural Fits to Neutron Data

	Exp.	Gamba $\theta=30$ $\phi=0$	Williams $\varepsilon = \sqrt{.7}$ and Williams to the Surface $\theta=41$ $\phi=25$	Williams $\varepsilon = \sqrt{.7}$ and Fits to Henry's Law Constants $\theta=41$ $\phi=11$
Bragg Angle (Deg)	19.9	19.9	19.9	19.9
	26.8	26.8	26.8	26.8
Plane Separation (Å) (h,k)	3.70	3.69 (0,2)(1,1)	3.69	3.69
	2.80	2.79 (1,2)	2.79	2.79
Relative Intensity	1.84	2.28	2.27	3.42

intensity equal to that of the peak at 19.9°. The angle θ of Figure 5.6 is 30° and 41° in the structures as determined by the GB and Williams models respectively. The best fits were obtained for angles θ of 53°, 52°, 51° and 48° if the tilt angle φ was 0°, 11°, 20° and 25° respectively. Therefore, a change of only 10° in the angle θ is necessary in the structure of the Williams models but, a change of 23° is needed in this angle for the GB model structure.

To summarize: the GB potential which was moderately successful in describing the sublimation energies and lattice dynamics in 3D did not predict the correct solid structures in 2D and resulted in a cohesive energy which was far too large. The Williams potential with 5 point charges predicted solid structures (square tee and commensurate 1x√3 herringbone) in agreement with the diffraction data but the cohesive energy and the area per molecule were too large. Reduction of the quadrupole moment resulted in an incorrect structure at low densities as the molecules found it easy to tilt from the surface. A change of the molecule-surface interaction to one in which the molecules found it more difficult to tilt from the surface returned the structure to the square tee. The Williams model with a 5 point charge electrostatic model and a reduced quadrupole has not been used to describe the lattice dynamics of the bulk solids. Calculations of the cohesive energies of the 3D cubic and orthorhombic structures with this model potential yielded 22.7 and 21.4 kJ Mol^{-1} respectively. This is to be compared with experimental values of 23.4 and 28.9 kJ Mol^{-1}. A rough check of the stability of these structures at 0 K showed that, in the cubic phase there was a very broad, shallow minimum in the energy at a volume 12% lower than the experimental volume (isotropic compression) with an energy of 23.7 kJ Mol^{-1}. The cubic phase is only stable for T > 133 K, and lattice expansion could make up some of this difference in the volumes and energies. For the orthorhombic phase, an uniaxial compression along the c-axis produced a very small decrease in the energy of 0.2 kJ Mol^{-1}. Clearly, this model does not stabilize the orthorhombic structure at low temperatures. Attempts to fit the parameters of this model to the cohesive energies were not successful.

The conclusion from these results is that no satisfactory intermolecular potential for C_2H_2 has been found as yet. Models which seem to work for the bulk systems do not work for the adsorbed systems. The possibility of hydrogen bonding in the 3D orthorhombic and 2D square tee structures needs to be addressed. A hydrogen bond could stabilize both of the structures. It would also tend to compress the square tee structure (found in these simulations) to a density closer to that found experimentally. If the hydrogen bond did exist, one would have to use different potential forms (in these simplistic models) for the different structures since the hydrogen bond would not exist in the cubic or $1\times\sqrt{3}$ herringbone structures.

5.11 Integral Heats of Adsorption

Direct measurements of the isosteric heat of adsorption as a function of coverage have been made by Piper et al for N_2 (33) and CO (34) on Grafoil. The results for CO were already presented in Figure 3.4. Integration of this curve yields the integral heat of adsorption which is a quantity easily calculated in a Monte Carlo simulation from the relation:

$$Q = H_g - H_s = (E_g + (PV)_g) - (E_s + (PV)_s) \qquad (5.5)$$

where g and s refer to the gas and surface phases. The PV term for the surface phase is generally very small and can usually be dropped. The PV term for the gas phase is $k_B T$. These approximations lead to:

$$Q = (E_g - E_s) + k_B T. \qquad (5.6)$$

The difference in the total energies is the potential energy of the surface phase at temperature T.

$$Q = k_B T - U(T) \qquad (5.7)$$

This was the relation used to calculate the integral heat in the simulations. The experimental heats vs. coverage for CO and N_2 at T = 79.3 K are displayed in Figure 5.8 and 5.9. The large values of the integral heat at low coverages were due to adsorption in the damaged areas of the substrate and the cell walls. When these contributions are corrected for, the results are the dashed lines marked 'experiment'. An extrapolation of the integral heat to zero coverage yields the heat of adsorption for a single molecule, Q(0).

Monte Carlo simulations of the integral heat for N_2 and CO at coverages up to one monolayer were performed as a test of both the molecule-surface and the molecule-molecule potentials. The same procedure was used for both N_2 and CO.

$\underline{N_2}$

An atom-atom 6-12 model and the Fourier method with parameters proposed by Steele (55) (Table 4.4) was employed as the molecule-graphite

Figure 5.8. A comparison of the calculated integral heat of adsorption vs. coverage and the experimental values for the CO/Grafoil system.

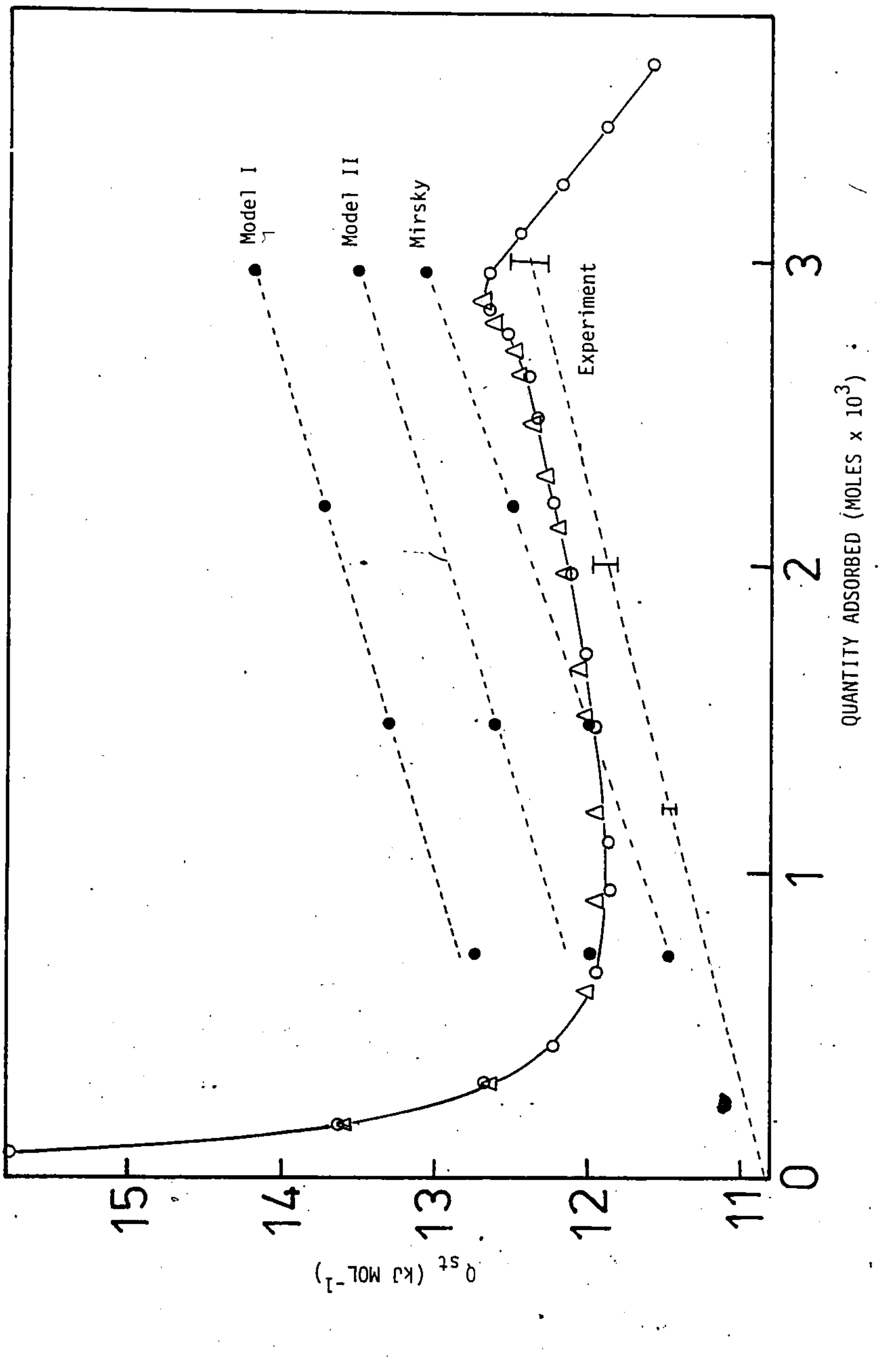
Model I
Model II
Mirsky
Experiment
15
14
13
12
11
0
1
2
3
QUANTITY ADSORBED (MOLES x 10^3)
Q_{st} (kJ MOL^{-1})

Figure 5.9. A comparison of the calculated integral heats of adsorption vs. coverage and the experimental values for the N_2/Grafoil system.

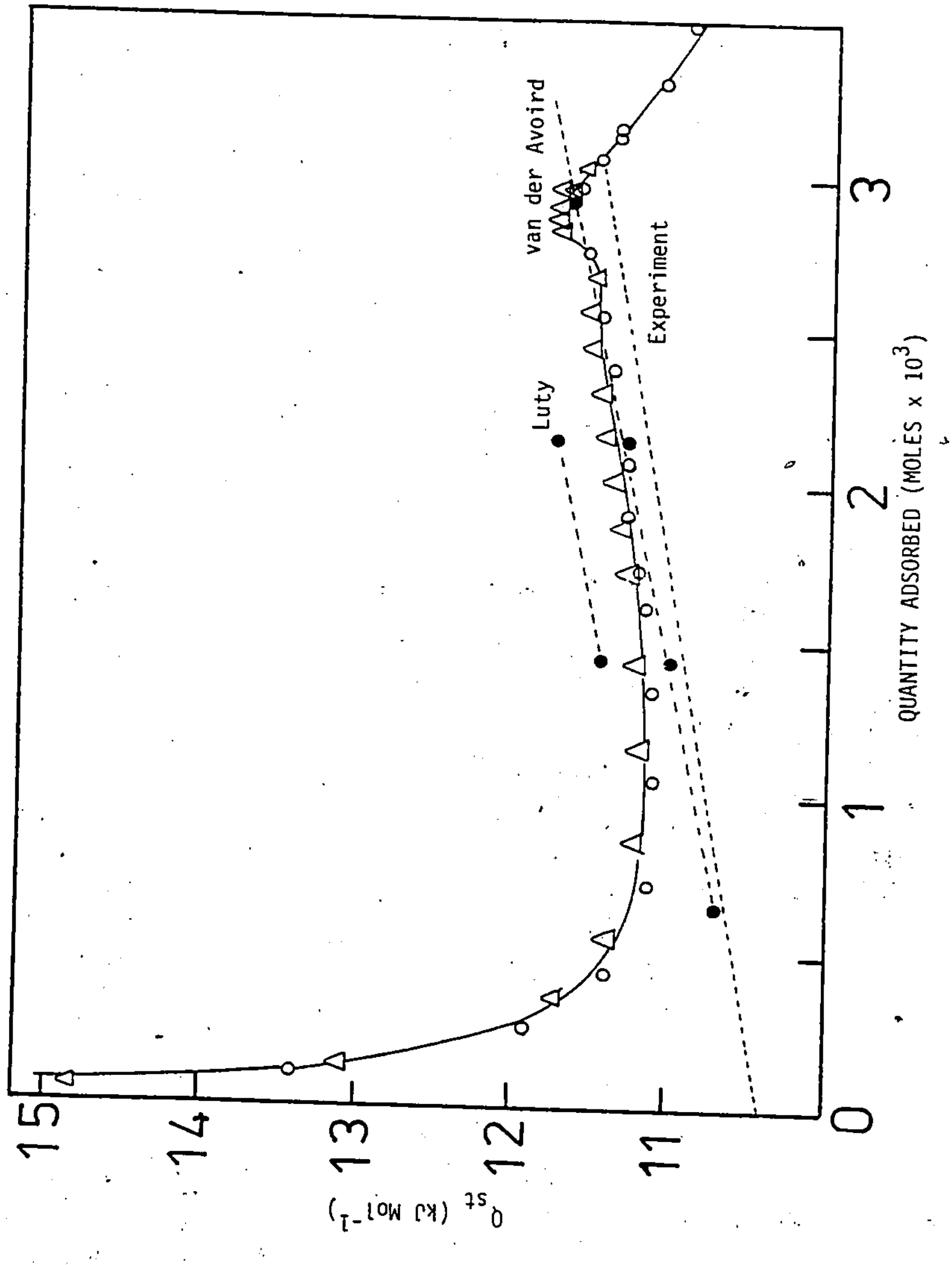
van der Avoird
Experiment
Luty
15
14
13
12
11
0
1
2
3
QUANTITY ADSORBED (MOLES x 10^3)
Qst (kJ Mol^{-1})

potential. The simulations were performed in two parts.

1. A Monte Carlo simulation of one molecule on graphite was performed first. Typically, 8.0×10^5 steps were made with an estimated uncertainty in the energy of ~ 0.02 kJ Mol^{-1}. The N_2-graphite parameters of Table 4.4 resulted in a value of $Q = 9.3$ kJ Mol^{-1}. This is to be compared to the experimental value of 10.4 kJ Mol^{-1}. Any change in the parameters to fit the experiment would not be unique, so, the well depth parameter ε was scaled to give $Q(0) = 10.4$ kJ Mol^{-1}. These parameters were then used in the simulations at higher densities.
2. The simulations of the coverage dependence of Q were performed with 64 molecules and periodic boundaries. Typically, 5000 steps were made which resulted in an uncertainty of ~ 0.05 kJ Mol^{-1} in the energy. The temperature was the experimental value of 79.3 K. The total potential of Table 4.1 was used up to a centre of mass separation of 8.0 Å. Between 8.0 and 12.0 Å, a molecule-molecule 6-12 potential was used with $\varepsilon = 91.5$ K and $\sigma = 3.68$ Å. This procedure resulted in a difference of $< 1\%$ in the energy but a very large saving in computer time.

The two molecule-molecule potential models of Sec. 4.4 were tested at coverages of 1/4, 1/2, 3/4 of a monolayer (defined by the $1 \times \sqrt{3}$ commensurate monolayer density). The results for both models are displayed in Figure 5.9. It is the difference in energy from the zero coverage value that should be considered when these results are compared to the experiment. It can be seen that the Van der Avoird potential gives values of the integral heat which are considerably closer to the experimental values than the Luty model but neither model fits the experimental results exactly.

Both of these potentials describe the lattice dynamics of the bulk solid but they give quite different results here. For both models, the film acted as a fluid with the molecules rotating freely. This rotation is the origin of the difference since, in the van der Avoird model the quadrupole energy is orientationally averaged, resulting in a smaller contribution, but in the Luty model there was no electrostatic interaction and the exchange and dispersion terms will not average away.

CO

The same molecule-surface model was used as in the case of N_2 but with the parameters due to Mirsky (Table 4.4). The well depth needed to be raised by only 4% to fit the experimental value of $Q(0) = 10.9$ kJ Mol^{-1}. It was values scaled by 5% that fitted the Henry's law constants in Sec. 5.7.

All three models of Table 4.3 were used in the simulations of the coverage dependence and yielded energies (Figure 5.8) which were too high. The two models which fitted the lattice dynamics ($K = 0$) and cohesive energies of the bulk solid (64) were far worse than the Mirsky model. It resulted in a fluid-like behaviour with few long-lived clusters. The other two models gave a liquid-like structure but with many long-lived clusters and few isolated molecules.

5.12 Orientational Order-Disorder Transition in N_2 and CO

From the previous section two models emerge as the most successful, the van der Avoird (N_2) and the Mirsky (CO). The remainder of this chapter will be concerned with the simulation of the low temperature structures and the orientational order-disorder transitions of these two molecules adsorbed on graphite.

As alluded to in the introduction, N_2 and CO have many similarities such as mass and size. In the past intermolecular potentials used for CO have been scaled from N_2 model potentials. But CO and N_2 molecules have some important differences. There is a mass asymmetry, and SCF calculations have shown a charge asymmetry in the CO molecule. N_2 has no odd multipoles whereas CO has an octopole and a small dipole moment. Although, N_2 and CO are essentially the same size, the charge density gradients are quite different. N_2, of course, is symmetric but in CO the charge density gradients about the carbon and oxygen atoms are not the same. Therefore, one can expect different exchange and dispersion parameters for the two ends of the CO molecule in an atom-atom model of the intermolecular potential.

In N_2, it has long been known that the electrostatic interaction is essential to the understanding of the condensed phases. For CO, the electrostatic interaction should be larger and more complex than in N_2.

The structure of N_2 at the $1x\sqrt{3}$ commensurate density at low temperatures is known (78) to be the herringbone shown in Figure (5.10). Results of heat capacity measurements (79) depict a transition at 27 - 28 K which was interpreted as an order-disorder transition from a $1x\sqrt{3}$ herringbone structure to a $1x\sqrt{3}$ rotator phase. Recently, a series of x-ray (23) and LEED (24) experiments has examined the low temperature structures as well as the transitions in both N_2 and CO adsorbed on

Figure 5.10. The commensurate $1 \times \sqrt{3}$ herringbone structure for N_2 adsorbed on graphite at 10 K.

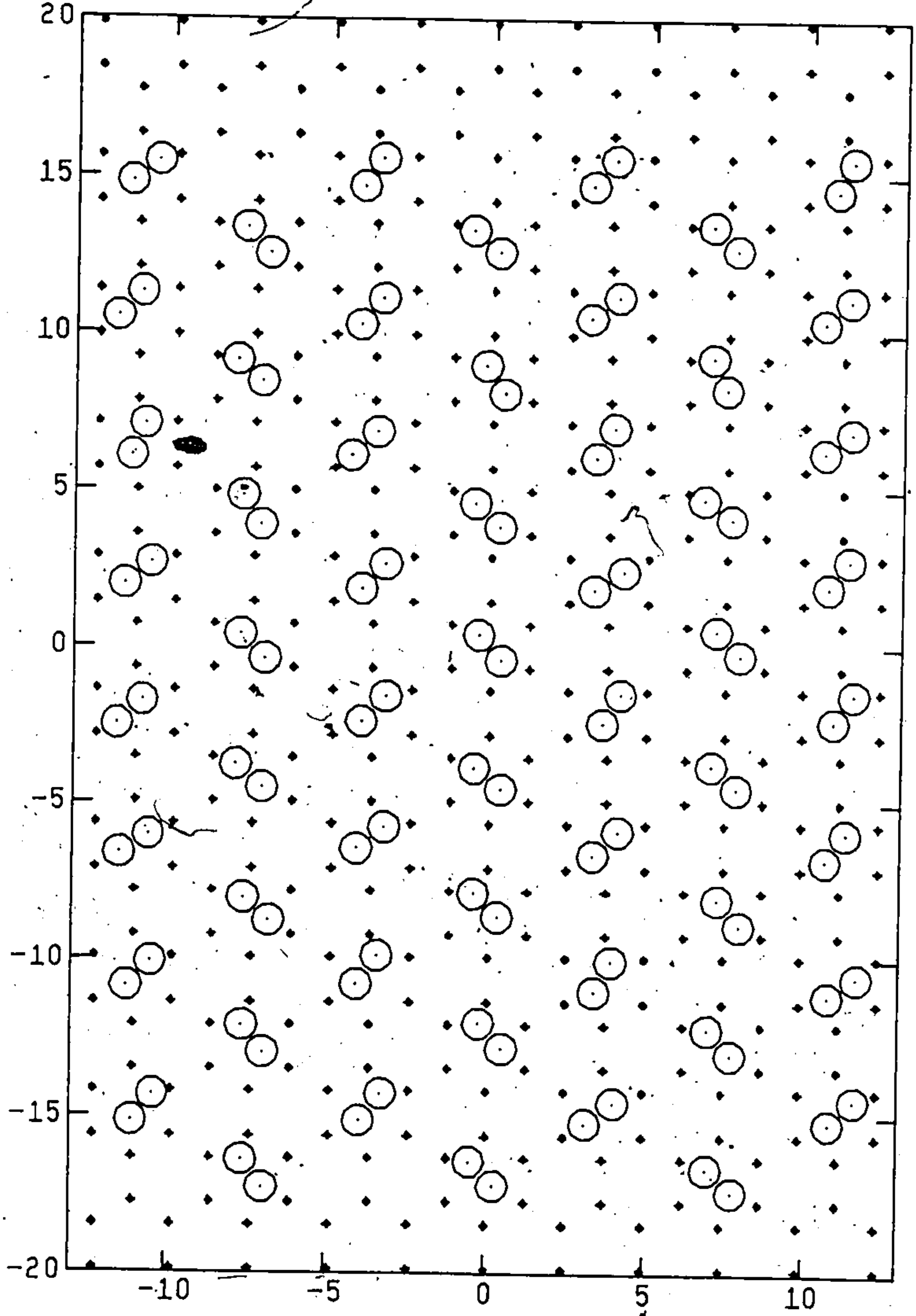
20
15
10
5
0
-5
-10
-15
-20
-10
-5
0
5
10

graphite. The x-ray studies have shown that the molecules are in a commensurate $1\times\sqrt{3}$ herringbone structure at low temperatures and coverages up to one monolayer. The orientational correlation length for CO was approximately half that of N_2. The LEED study confirmed these results but also showed that there was no head to tail order in the CO structure. When the commensurate monolayers of CO and N_2 were heated an orientational order-disorder transition was observed in the x-ray measurements (Figure 5.11A). In N_2 this transition was sharp and occurred between 27 - 30 K but, in CO it was much broader, beginning at ∿ 20 K. The melting transitions were shown to be at ∿ 80 K for both solids (Figure 5.11B). These results are completely the reverse of those expected from the simple scaling arguments for the quadrupole moment that worked well for the bulk solids.

The x-ray studies were also made at higher surface densities but the authors claim considerable uncertainty in the value of the density. They tentatively placed the value at 1.12 commensurate monolayers but suggest that this value may be too high. In any case, the structure of both CO and N_2 remained herringbone, but the behaviour of the orientational transition was completely different, in fact, almost the reverse of the situation at the commensurate density. Here, the transition is broad for N_2, starting at a very low temperature and is accompanied by a slight increase in the lattice parameter. The transition in CO, on the other hand, does just the reverse. It is sharpened considerably and moves to a higher temperature accompanied by an increase in the lattice parameter. The higher density results are shown in Figures 5.12A, B.

Figure 5.11. X-ray scattering data for the commensurate phases of N_2 (●) and CO (○) adsorbed on graphite, from ref. (23). The (20) reflection is due to the centre of mass $1 \times \sqrt{3}$ order and the (21) reflection is due to the herringbone superlattice.

A) Data for the orientational order-disorder transition.

B) The melting transition.

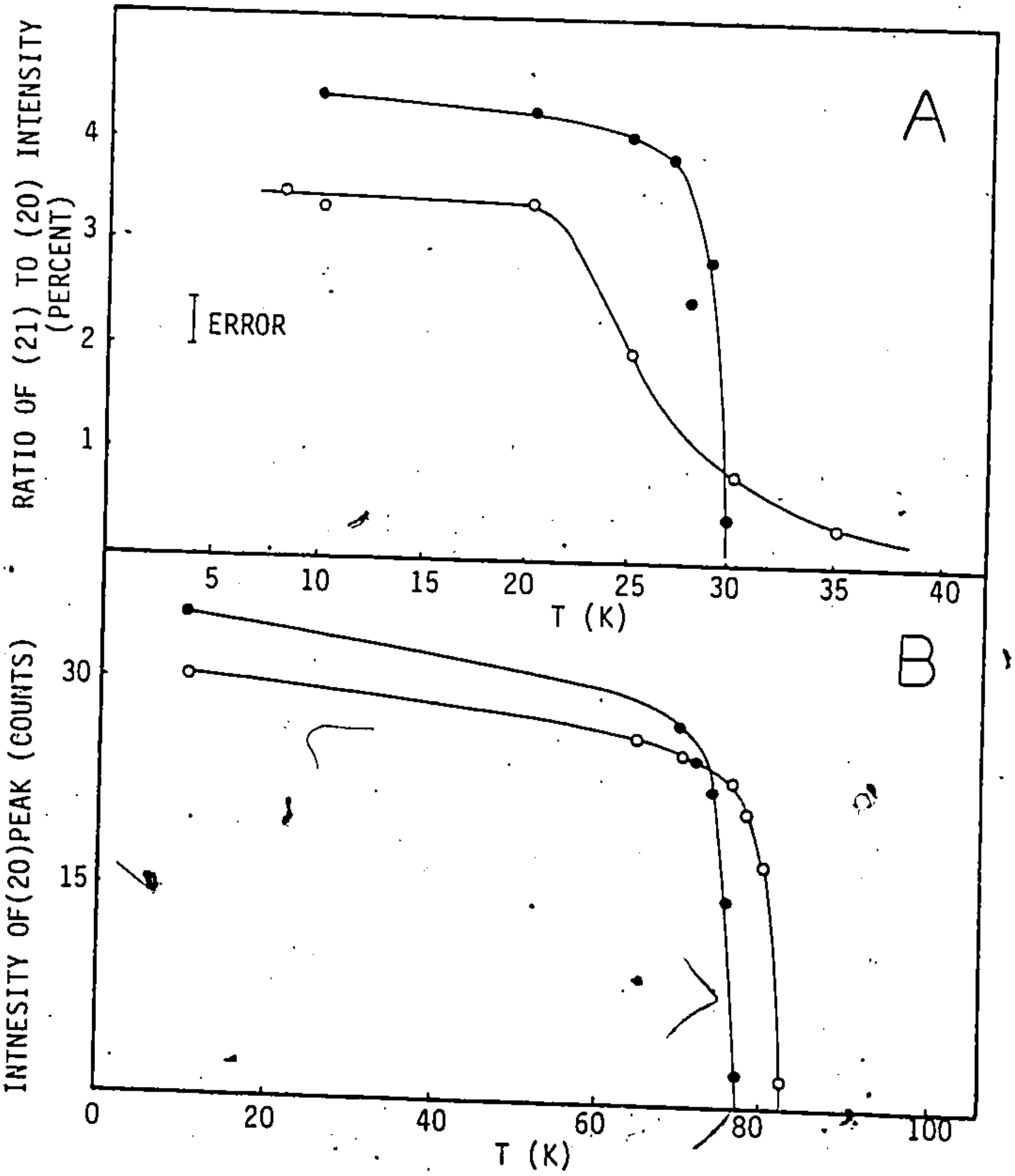
RATIO OF (21) TO (20) INTENSITY (PERCENT)
1
2
3
4
ERROR
A
5
10
15
20
25
30
35
40
T (K)
B
INTNESITY OF(20)PEAK (COUNTS)
15
30
0
20
40
60
80
100
T (K)

Figure 5.12. X-ray scattering data for the incommensurate phase of N_2 (A) and CO (B) adsorbed on graphite, from ref. (23). The open circles are the data for the orientational order-disorder transition and the closed circles are the data for the intermolecular distance.

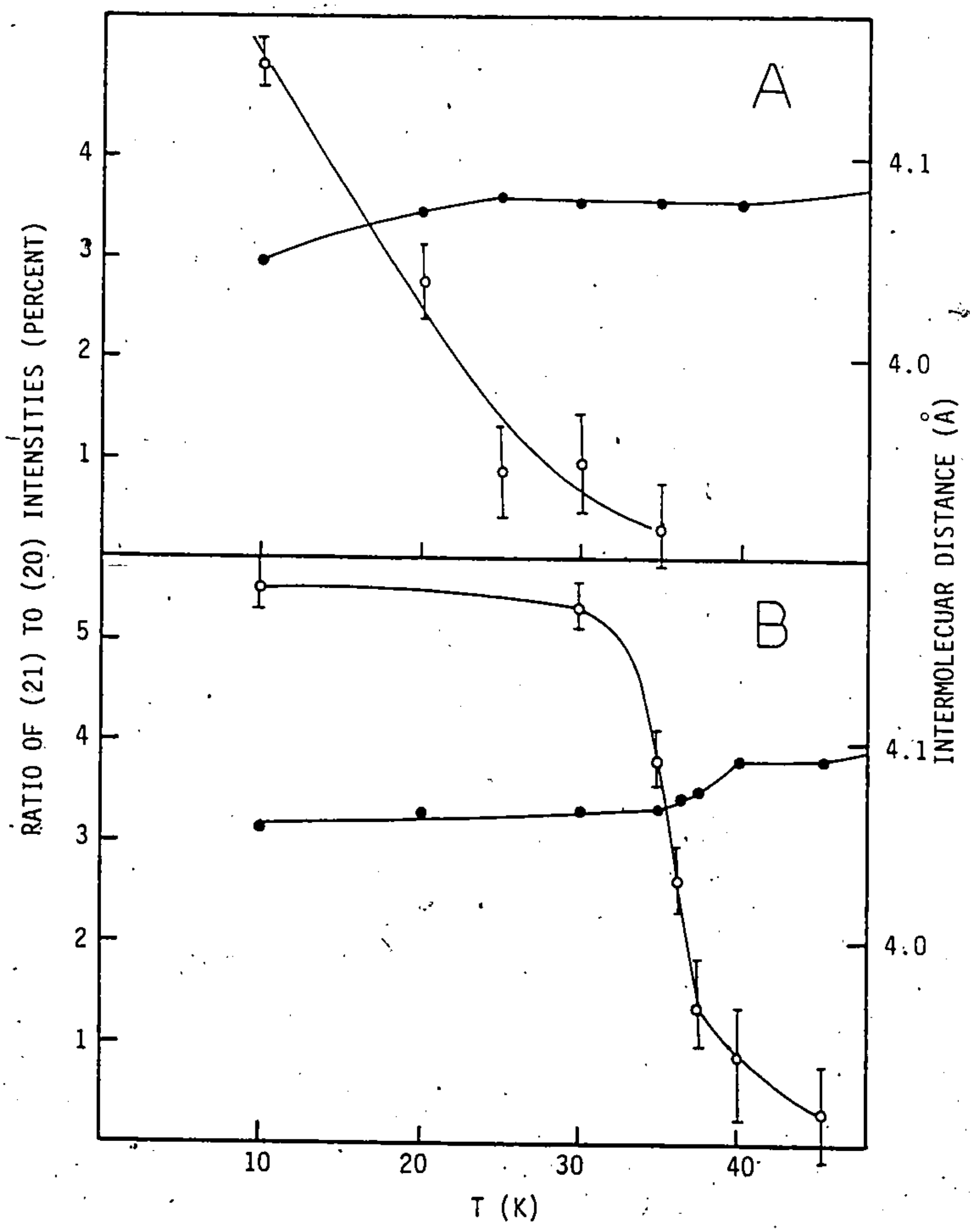
A
B
RATIO OF (21) TO (20) INTENSITIES (PERCENT)
INTERMOLECUAR DISTANCE (Å)
4
3
2
1
5
4
3
2
1
4.1
4.0
4.1
4.0
10
20
30
40
T (K)

LEED measurements at 1.13 commensurate monolayers have shown that CO has a pinwheel structure shown in Figure 5.13. Since the x-ray results gave no indication of pinwheels, the density might be lower than the 1.12 commensurate monolayers tenatively suggested.

Three calculations have been made on the N_2/graphite system (80-82) which place the transition at ∿ 30 K. The system of O'Shea and Klein was a fixed triangular lattice of point quadrupoles whereas Mouritsen and Berlinsky used an ideal quadrupole Hamiltonian for 10,000 centres, also fixed on a triangular lattice. They found the transition to be 1st order.

Talbot et al used the molecular dynamics method on a smaller system of 96 molecules but a more realistic N_2-N_2 potential. Their model was an atom-atom 6-12 potential ($\sigma = 3.32$ Å, $\varepsilon = 35$ K) with 3 charges on the atomic site and centre of mass. The 6-12 parameters were taken from Chung and Powles (69) and were developed by fitting to several properties of the 3D liquid. The 3 point charges reproduced the experimental quadrupole moment. They did not include substrate mediated effects. The molecule-graphite potential used was the same as the one used in Sec. 4.8 to calculate the integral heat but the parameters were not scaled to fit the experimental value of 10.4 kJ Mol^{-1} (this datum was not available at that time). The order-disorder (rotator) transition was found to be at 35 K, i.e., 8 K higher than in the experiment. An important result of the work was the finding that the transition is accompanied with an increased tendency for the molecules to tilt from the surface. To help to understand these results, Monte Carlo simulations of CO and N_2 were performed at densities of 1.00 and

Figure 5.13. An incommensurate pinwheel structure.

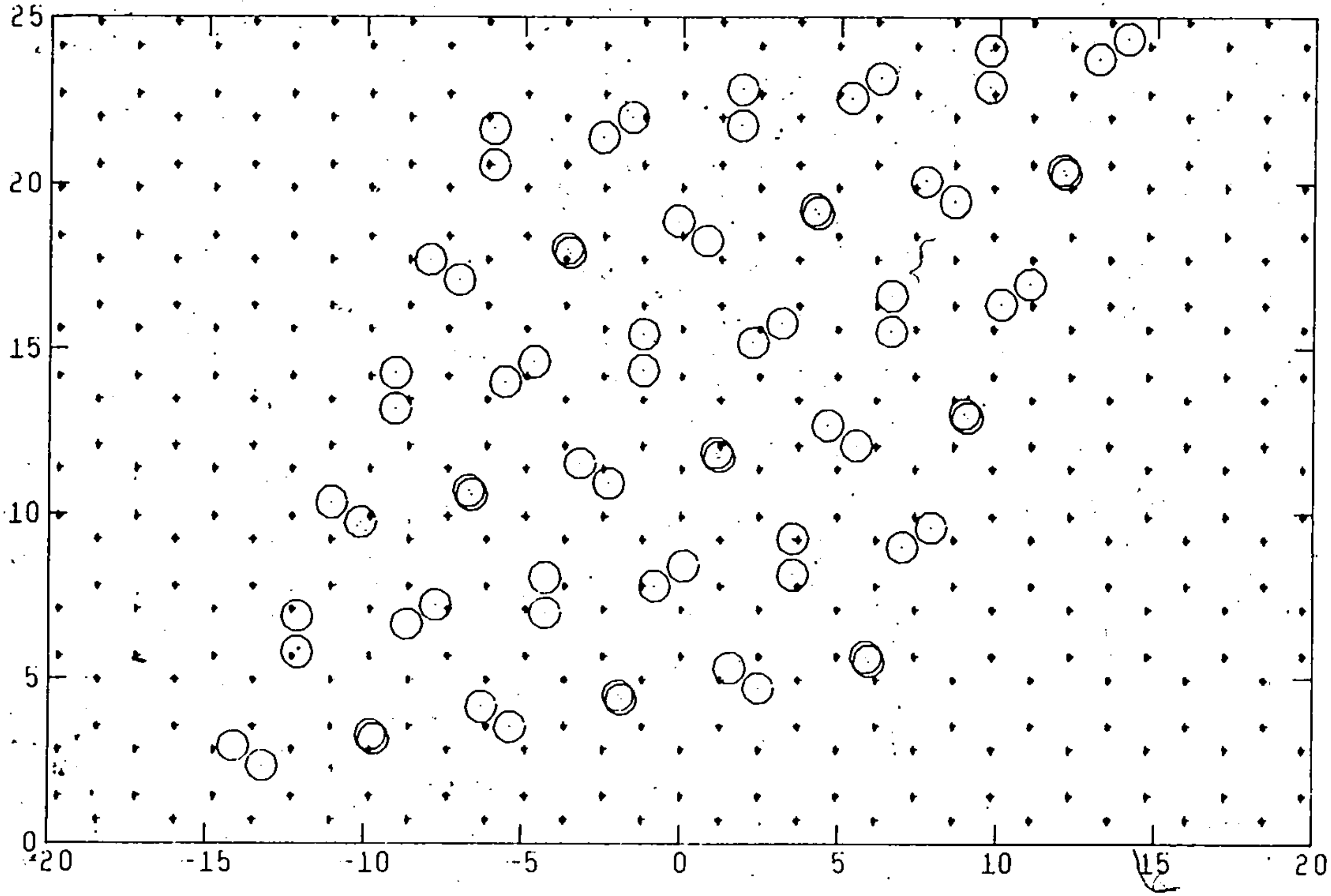
25
20
15
10
5
0
-20
-15
-10
-5
0
5
10
15
20

1.09 commensurate monolayers and temperatures up to 80 K. Simulations at densities up to 1.25 monolayers were also made to determine the zero temperature structures. The potentials used were the van der Avoird (N_2) and Mirsky (CO) models with a molecule-surface interaction which fitted the experimental values of q_{st} at zero coverage (Sec. 5.11).

$\underline{N_2}$

It was important to know at the outset the zero temperature structure predicted by the van der Avoird model. The 4 molecule and the 64 molecule systems both yielded the commensurate 1x$\sqrt{3}$ herringbone lattice with the molecules lying flat on the surface as is depicted in Figure 5.10 at 10 K. This is in agreement with the x-ray and LEED data.

The structures at densities of 1.09, 1.13 and 1.16 1x$\sqrt{3}$ commensurate monolayers were found at 5 K using the 4 molecule system at a fixed area. The results at densities of 1.09 and 1.13 were the same as at 1.00 but with an uniaxial distortion in the x-direction (Figure 5.10). LEED data of Fain and Diehl (83) have shown such an uniaxial distortion for a density of 1.05 commensurate monolayers but at higher densities, a triangular lattice with the molecules tilted from the surface was formed.

At the density of 1.16 1x$\sqrt{3}$ monolayers the pinwheel structure of Figure 5.13 was created. It is very similar to the (111) plane of the bulk phase and was predicted for N_2 on graphite by Harris and Berlinsky (77) from their mean field calculations.

The Monte Carlo simulations of the orientational order-disorder phase transition were performed with a small system consisting of 64 molecules in periodic boundaries. In other simulations the effect of small system sizes has been shown to be a broadening of the phase transition (81). Such an effect would be expected here.

A small system was used as a compromise between an attempt to test many different potential models and to obtain accuracy in the simulations. In typical simulations of the phase transition, 16,000 steps were made but in transition regions up to 32,000 steps were occasionally necessary to obtain sufficient accuracy. The molecule-molecule interaction was taken to be the complete potential in Table 4.1 up to a centre of mass separation of 8.0 Å. Between 8.0 Å and 12.0 Å the molecule-molecule 6-12 potential was used as in the simulation of q_{ST} vs. coverage in Sec. 5.11.

To characterize the system several order parameters were calculated. The average potential energy, E, can be used to calculate the heat capacity either through $C_V = dE/dT$ or from the fluctuations

$$C_V = \frac{<E^2> - <E>^2}{kT^2}.$$

Very good statistics are necessary to find C_V because small differences are involved. The average angle of the tilt of the molecular axis from the surface $<\theta>$ was useful in studying the out-of-plane order. The herringbone (in-plane) order was monitored with the quantity $\sum_i \cos(2\theta_i)$ where θ_i is the angle from a reference position for molecule 'i'. For all of the runs the reference was a snapshot of the low temperature (10 K) structure. The centre of mass order was followed by calculating the mean square displacements of each molecule from a reference position.

The results of the simulation are presented in Figure 5.14A, B. The in-plane order parameter shows a clear transition centred at 28 K

Figure 5.14. Results of the simulations of the orientational order-disorder transition in the commensurate phase of N_2 on graphite

● - energy

○ - heat capacity

● - orientational order parameters <cos2θ>

○ - angle of tilt from the surface

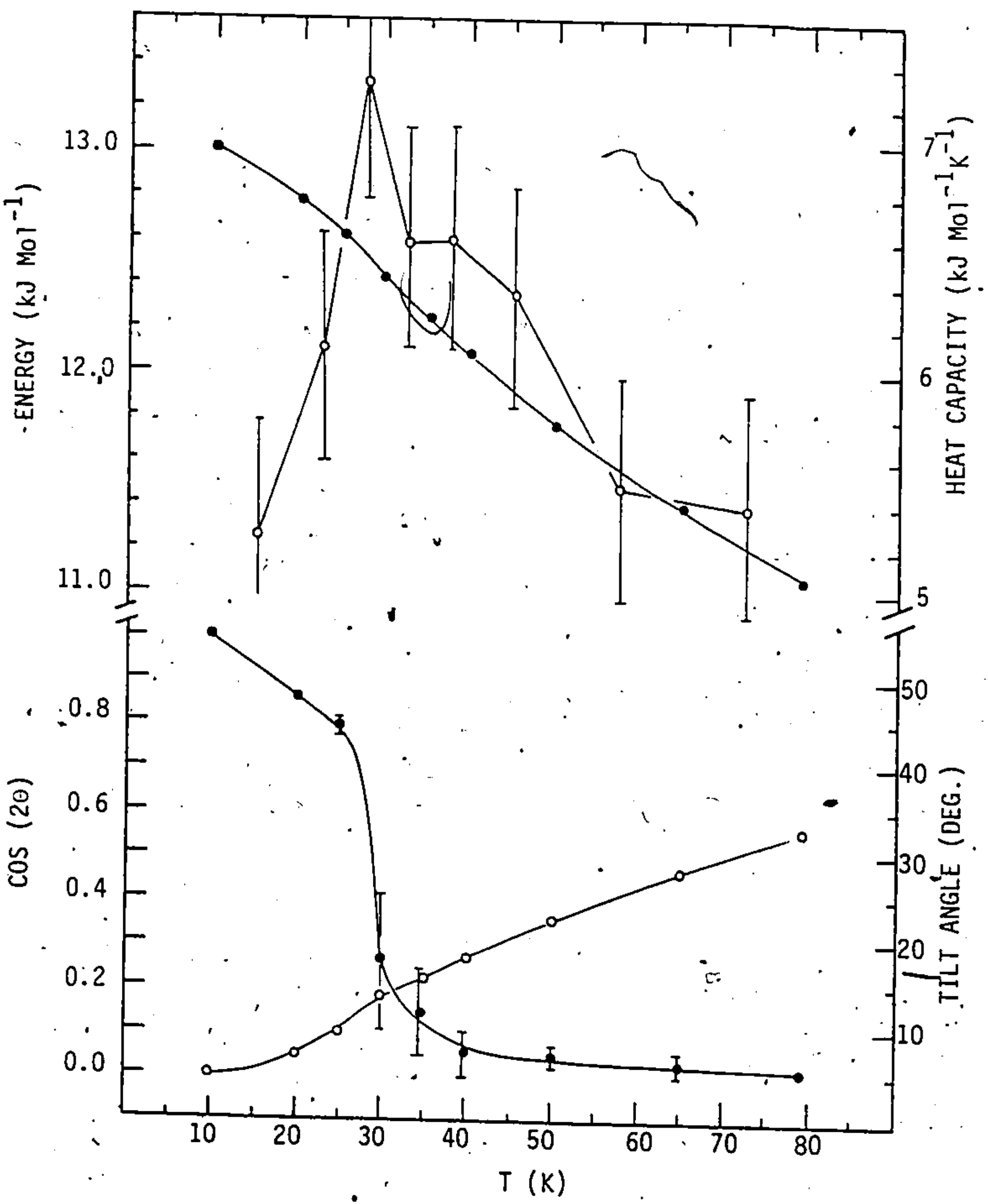
-ENERGY (kJ Mol^{-1})
13.0
12.0
11.0
HEAT CAPACITY (kJ Mol^{-1}K^{-1})
7
6
5
COS (2Θ)
0.8
0.6
0.4
0.2
0.0
TILT ANGLE (DEG.)
50
40
30
20
10
10
20
30
40
50
60
70
80
T (K)

in agreement with experiment. There is also a peak in the heat capacity as calculated from dE/dT and a change in the tilt angle at this temperature. The agreement with experiment (Figure 5.11) is somewhat better than in the calculations of Talbot et al (82). The difference probably lies in the lower quadrupole moment in the Van der Avoird potential model. The monolayer remained solid up to 80 K which was the melting point as detected by the x-ray measurements, but the simulations do not allow for lattice expansion (fixed boundaries) and therefore one can expect the melting temperature to be raised.

Because of this success, a simulation at 1.09 $1 \times \sqrt{3}$ monolayer was tried. The choice of this surface density was determined by the requirement to maintain commensurate periodic boundaries. Only particular densities could be used if the number of molecules was to be kept constant. To achieve a density of 1.09 the commensurate monolayer was distorted uniaxially to be consistent with the 4 molecule structure calculation at this density. The results are in Figure 5.15A,B and should be compared to those of the x-ray experiment in Figure 5.12A, B. We should note that the x-ray measurements showed a broadening of the transition starting at a very low temperature. The in-plane order parameter (Figure 5.15B) shows a sudden drop at 15 - 20 K and another at 35 K. The transition is completed by T = ∿40 K which is about 5 K higher than the transition temperature found experimentally.

The heat capacity also shows a broadening of the transition with a shoulder on the low temperature side of a peak at 31.5 K. Again, the x-ray experiments indicated a slight decrease in density (increase in

Figure 5.15. Results of the simulations of the orientational order-disorder transition in the incommensurate phase of N_2 on graphite.

● - energy

○ - heat capacity

● - orientational order parameter $\langle\cos 2\theta\rangle$

○ - angle of tilt from the surface

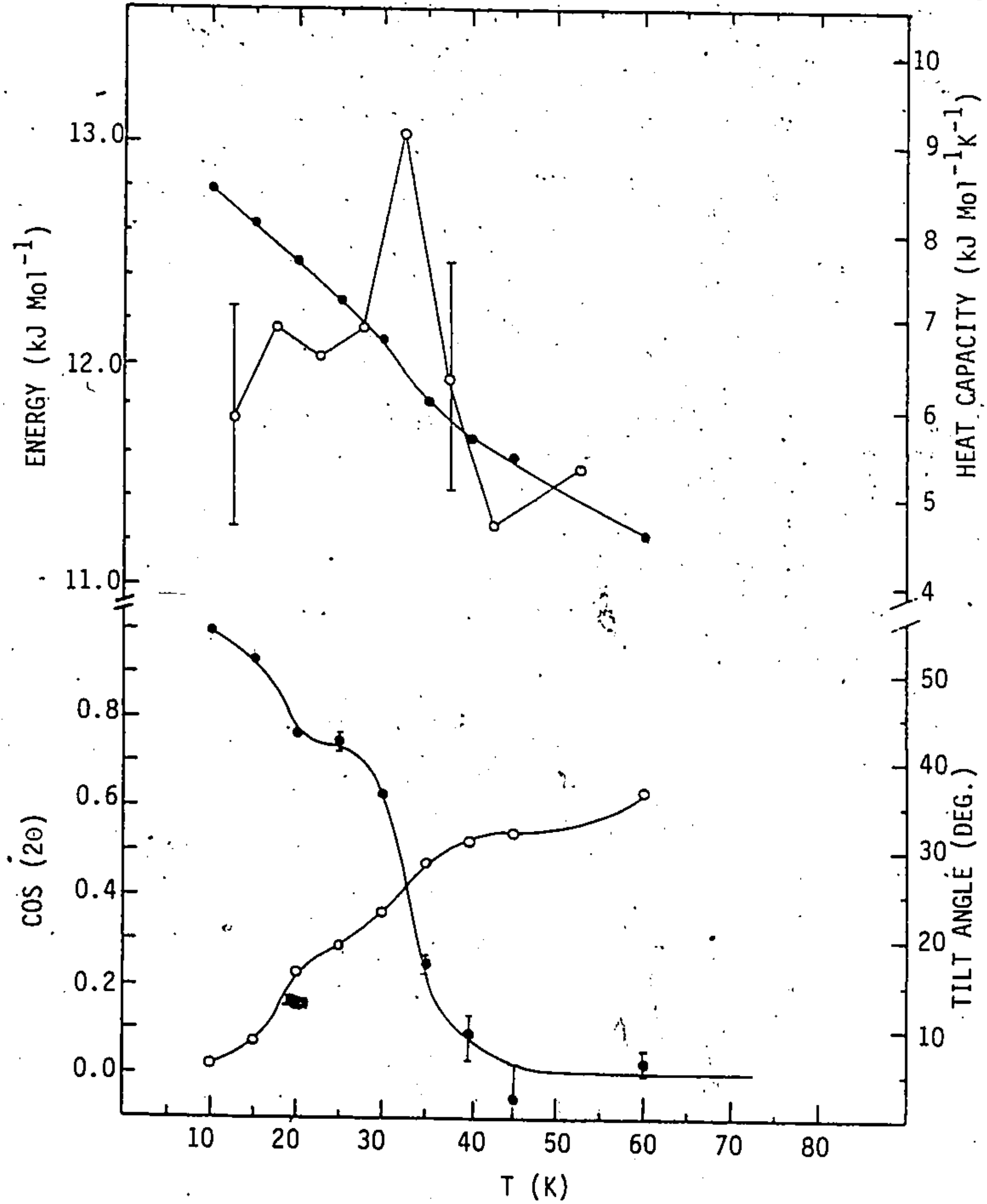

ENERGY (kJ Mol^{-1})
13.0
12.0
11.0
HEAT CAPACITY (kJ Mol^{-1}K^{-1})
10
9
8
7
6
5
4
COS (2Θ)
0.8
0.6
0.4
0.2
0.0
TILT ANGLE (DEG.)
50
40
30
20
10
10
20
30
40
50
60
70
80
T (K)

lattice parameter) (Figure 5.12B) through the transition but the simulation was performed at constant density. The effect of that restriction on the orientational order is difficult to determine, but the change in density was quite small and so, hopefully, would be its effect.

The shoulder in the heat capacity and the first decrease in the in-plane order parameter ($\langle\cos 2\theta\rangle$) is accompanied by a large increase in the tilt angle $\langle\theta\rangle$ at T = 17.5 K. A snapshot of a typical configuration at T = 20 K is shown in Figure 5.16. There are 8 molecules standing vertically to form local pinwheel structures. By contrast at T = 10 - 15 K the molecules were lying flat (no pinwheels).

When the solid was cooled from 20 K to 15 K, the number of molecules standing on the surface was reduced to 3 but the structure seemed to be frozen-in and the energy did not quite return to the original value at 15 K. Hysterisis in low temperature simulations is very common. The solid seemed to relieve the pressure brought on [illegible] the increased density and temperature by the formation of pinwheels. At a density of 1.16 $1\times\sqrt{3}$ monolayers at 0 K, the structure was an ordered system of pinwheels. The creation of isolated pinwheels would then account for the broadening of the rotator transition at increased densities which was seen in the x-ray experiments.

CO

For CO the same approach was used. The three CO-CO potentials of Table 4.3 were tried with the molecule-graphite potential which

Figure 5.16. A snapshot of the simulated structure of incommensurate N_2 on graphite projected onto the surface.

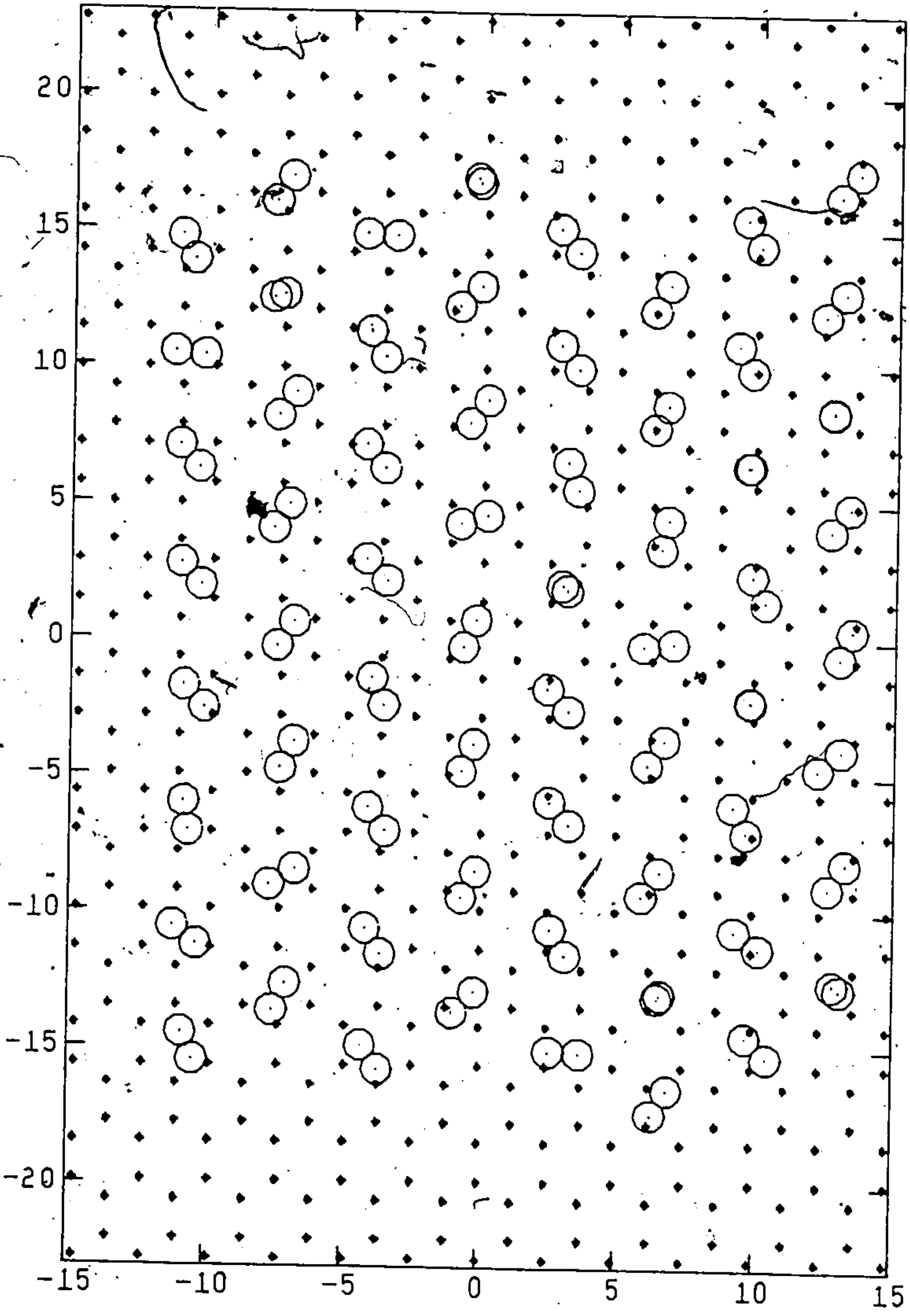
20
15
10
5
0
-5
-10
-15
-20
-15
-10
-5
0
5
10
15

fitted both Q(0) and the Henry's Law constant (Sec. 5.7).

The first potential (I in Table 4.3) did not give an ordered herringbone structure when 64 molecules were placed in periodic boundaries at the commensurate density. The structure consisted of small patches of herringbone with many isolated pinwheels. In a larger system it is conceivable that these patches would become domains of herringbone with pinwheel walls, or domains of both pinwheel and herringbone structures. This model also gave a much too large value of the integral heat of adsorption.

Potential model II without the substrate mediated interactions gave an ordered commensurate $1\times\sqrt{3}$ herringbone when 64 molecules were placed in periodic boundaries, but it also corresponded to a value of the integral heat of adsorption which was too large. A quick (poor statistics) investigation of the orientational order-disorder transition showed it to occur at T = ∿ 35 K, which was about 15° higher than was observed in the experiment. The difference is probably due to the large attractions in the model but, when the substrate mediated interaction was added, the low temperature structure became, as in model I, a mixture of herringbone and isolated pinwheels.

This left only the Mirsky model potential which when used in the 4 molecule method at a fixed commensurate density, yielded no obviously ordered state at low temperature. With 64 molecules in periodic boundaries, the result was a badly disordered herringbone structure with patches of herringbone and orientational glassy structure. When, in the 4 molecule method, the density was allowed to change, the structure at 5 K was an ordered incommensurate herringbone structure at a density of 1.085 monolayers. Therefore, it appears that the molecule which corresponds to the Mirsky potential is too small. There has been a suggestion (86) that the corrugation in the Fourier sum method [illegible] the molecule surface potential is as much as a factor of 2 too sma[illegible]. Doubling the corrugation in the calculation with the Mirsky p[illegible] did not decrease the density significantly. This was not pursued further. When 64 molecules were placed in a commensurate $1 \times \sqrt{3}$ herringbone structure with periodic boundaries the system remained stable up to T = 25 K at which point it transformed into the stable orientational glassy structure with only small patches of herringbone as is shown in Figure 5.17. The energy of the glassy structure was lower than that of the ordered herringbone structure. The glass was cooled to 15 K and heated to 80 K. The results for E, C_V, $\langle\theta\rangle$ and R are displayed in Figures 5.18A, B. Experimentally, the transition from an ordered herringbone to a free rotator phase was observed to be very broad - between 20 and 35 K. Because of the glassy state, an orientational order parameter was not calculated. The heat capacity seemed to have a broad transition between 30 and 60 K with a peak at 50 K. There appeared also to be a broad shoulder on the low temperature side which is also seen in the change of the tilt angle (Figure 5.18B). The reason is clarified when the mean square deviations from ideal commensurate sites are examined Figure 5.18B. Up to 45 K the layer remained solid but at 50 K eleven molecules jumped to neighbouring solid sites followed by three other molecules at 55 K. At 60 K the monolayer was

Figure 5.17. A snapshot of the simulated structure of commensurate CO in a glass-like state. The shaded circles represent the oxygen atom.

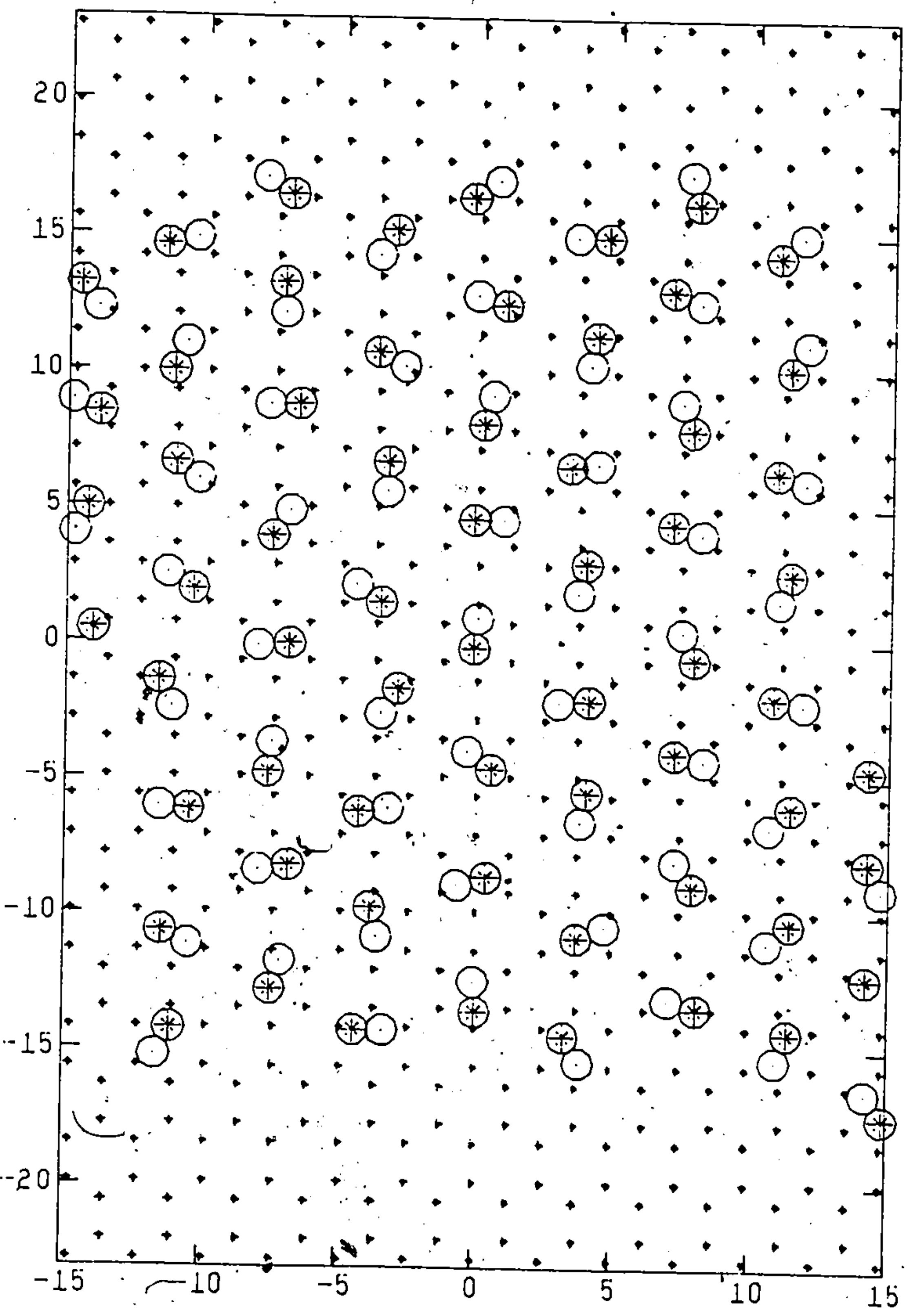
20
15
10
5
0
-5
-10
-15
-20
-15
-10
-5
0
5
10
15

Figure 5.18. Results of the simulations of the orientational order-disorder transition in the commensurate phase of CO on graphite.

● - energy

○ - heat capacity

● - root mean square deviations from ideal sites

○ - angle of tilt from the surface

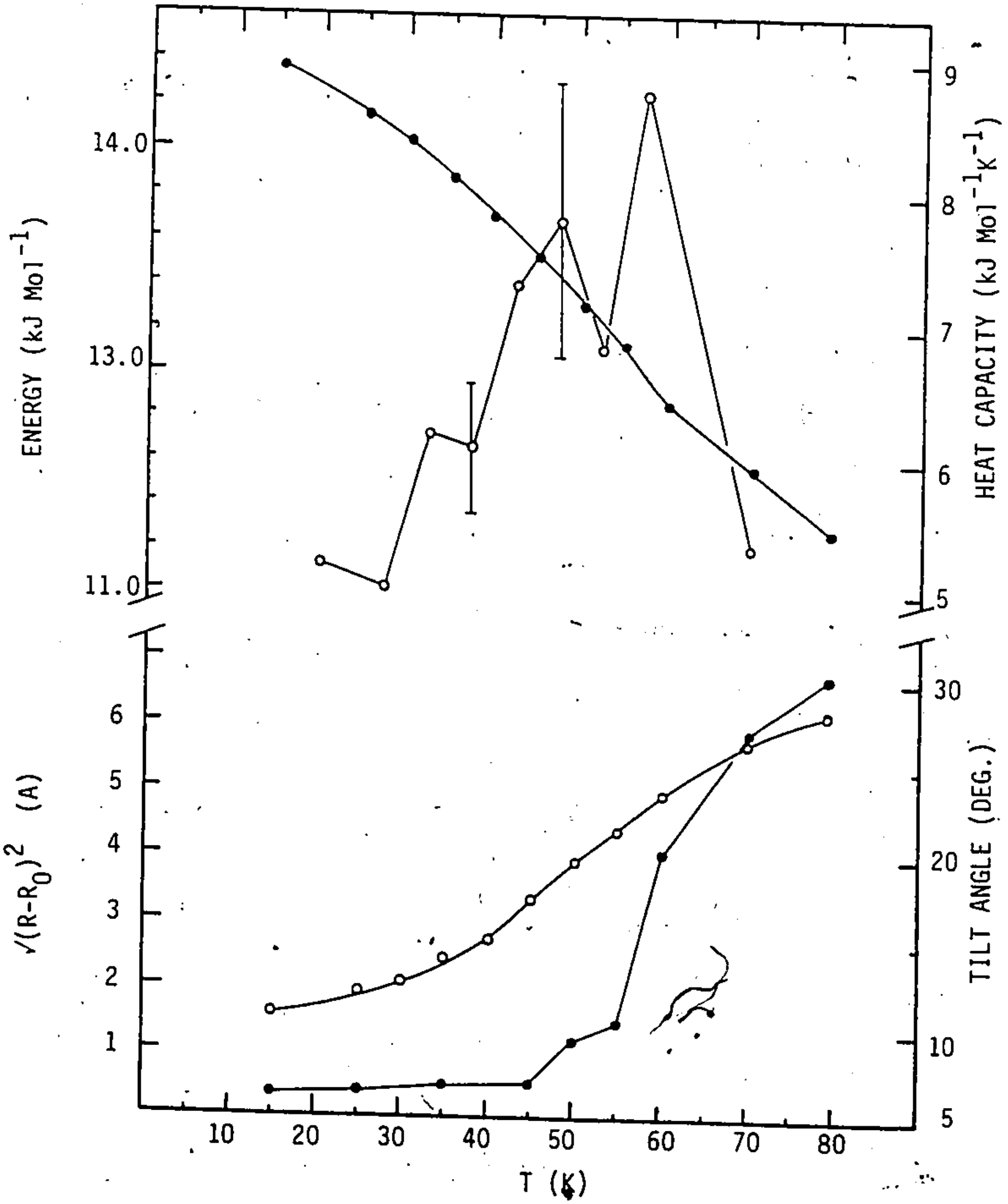
ENERGY (kJ Mol^{-1})
14.0
13.0
11.0
HEAT CAPACITY (kJ Mol^{-1}K^{-1})
9
8
7
6
5
$\sqrt{(R-R_0)^2}$ (A)
6
5
4
3
2
1
TILT ANGLE (DEG.)
30
20
10
5
10
20
30
40
50
60
70
80
T (K)

liquid. Thus, melting occurs between 50 - 60 K, which explains the origin of the peak in the heat capacity. The x-ray measurements showed the melting point to be T = 80 K but, since the monolayer in the simulation is being maintained at a commensurate density (it wants to be higher) by the periodic boundaries, it is effectively at a negative pressure, which reduces the melting temperature. The shoulder in the heat capacity therefore could be due to a transition to a free rotor phase just prior to melting.

The simulations at 1.09 monolayers were started from the structure determined by the 4 molecule method at 5 ~~K.~~ This was an uniaxially distorted commensurate herringbone. The head-to-tail ordering of the CO molecules was investigated in the LEED experiment only at the commensurate density and no order was found. This does not mean that order does exist at higher densities. There are many ways of setting up a herringbone if head-to-tail order is considered. The two primary ones are shown below. The energy of structure II was found

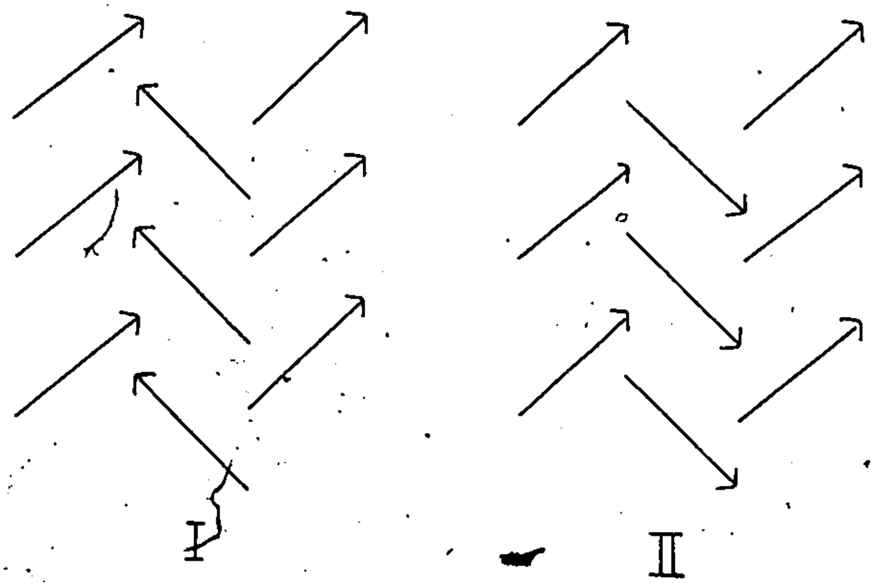

Figure 5.19. Results of the simulations of the orientational order-disorder transition in the incommensurate phase of CO on graphite.

● - energy

○ - heat capacity

● - orientational order parameter $\langle \cos 2\theta \rangle$

○ - angle of tilt from the surface

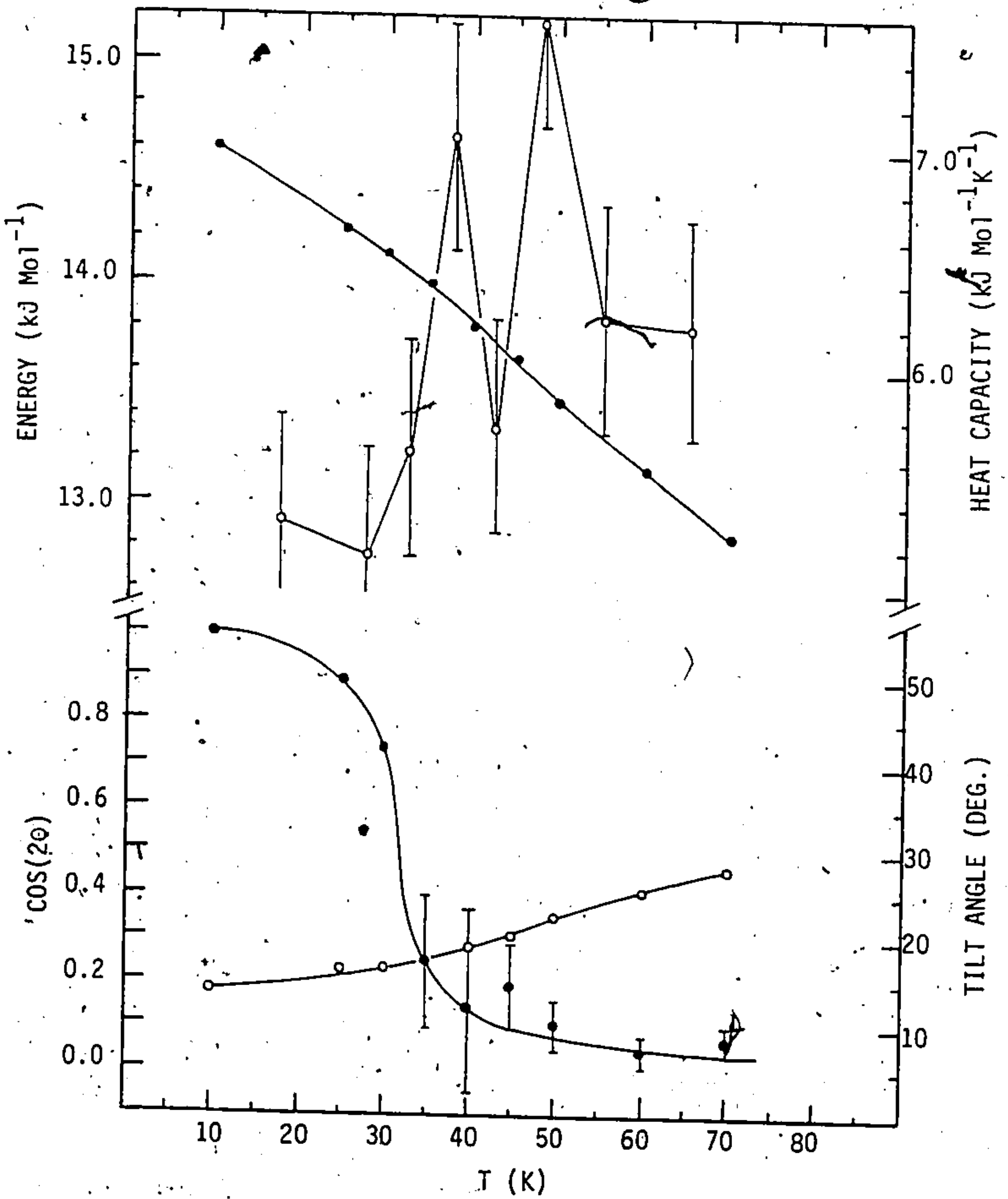
ENERGY (kJ Mol^{-1})
15.0
14.0
13.0
HEAT CAPACITY (kJ Mol^{-1}K^{-1})
7.0
6.0
COS(2Θ)
0.8
0.6
0.4
0.2
0.0
TILT ANGLE (DEG.)
50
40
30
20
10
10
20
30
40
50
60
70
80
T (K)

to be lower than that of I in the Mirsky model at a density of 1.09 $1 \times \sqrt{3}$ monolayers by only 11 K. The former structure was used as the starting point in the simulations. The results in Figure 5.19A, B should be compared to the x-ray results of Figure 5.12. The order-disorder transitions in both occur at 35 K but the simulation shows a slightly broader transition. As in other simulations, the loss of in-plane order is accompanied by a loss of the out of plane order (79,82). A possible reason for this is that the herringbone structure makes tilting unfavourable but when the order is lost only the surface interaction is left to hold the molecules flat against the surface. The x-ray data showed a small change in the lattice parameter at the transition but, as before the boundary conditions prevent lattice expansion. There was no evidence of melting of the solid up to the highest temperature investigated, T = 70 K.

Although there is good agreement between the calculated and experimental results it must be remembered that the monolayer in the simulation was not subjected to pressure due to the small size of the molecule in the model. A compensating factor may be that the uniaxially distorted structure is the experimental structure, as was found in the case of N_2.

The behaviour of the model at the still higher densities of 1.13, 1.16, 1.25 $1 \times \sqrt{3}$ monolayer was investigated at 5 K with the 4 molecule method. At densities of 1.13 and 1.16 $1 \times \sqrt{3}$ monolayers, the structure was a uniaxially distorted herringbone but, at the density of 1.25 $1 \times \sqrt{3}$ monolayers the pinwheel structure was found. LEED experiments found evidence for the pinwheel structure at a density of only 1.13 monolayers. If one uses the zero pressure density of 1.09 $1\times\sqrt{3}$ monolayers as the reference, then the density of 1.25 is reduced to 1.15 monolayers in the calculations. It is possible that pinwheels may appear at an even lower density in the calculations, but this was not investigated.

Simulations were performed on a hybrid potential model consisting of the electrostatic interaction of CO and the atom-atom parameters of N_2 in an attempt to distinguish the effects of the electrostatic and atom-atom asymmetries. The results pertaining to the structures at densities of 1.00, 1.04, 1.13, 1.16 monolayers were essentially the same as those obtained for N_2 which indicates that the major differences in the behaviour of CO and N_2 are to be ascribed to the dispersion and exchange terms.

The effect of an image force on these results should be addressed. With the three point charge distribution of the CO models and an image plane raised above the nuclear centres, the charge on the carbon atom end touches its own image. A model for the charge distribution which consists of three centres and multipoles up to the octopole at each centre (87) also results in this catastrophe, but point multipoles placed on the centre of mass are stable. The quadrupole-image quadrupole interaction is greater by a factor of 8/3 if the molecular axis is perpendicular to the surface than if it is parallel to it. This anisotropy increases the probability of a pinwheel structure. Calculations employing the 4 sublattice method did show a tendency to increase the tilt angle slightly in the case of CO and to a lesser extent in N_2. The effect of this interaction was still being pursued at the time of this writing. The energy differences involved are small and large amounts of computer time are required to reach equilibrium.

The conclusion of this section must be that a satisfactory potential model for CO has still to be found. It appears that the properties of CO are more sensitive to details of the potential than are those of N_2.

CHAPTER 6

SUMMARY AND CONCLUSIONS

To help understand the behaviour of the simple linear molecules CO, N_2 and C_2H_2 adsorbed on a graphite surface and the interaction potentials involved, vapour pressure isotherm measurements and classical Monte Carlo simulations were performed.

With the use of standard interaction potentials, the Monte Carlo calculations of C_2H_2/graphite revealed two solid structures: an incommensurate square-tee at low density and a commensurate $1 \times \sqrt{3}$ herringbone at higher densities. Both of these structures were shown to be in agreement with existing diffraction data but differed from those proposed in the literature. It was found that several combinations of molecule-molecule and molecule-surface potentials could produce these structures.

Henry's Law constants were used to study the interaction of a single molecule with the surface. It was found that in the case of CO a simple 10-4 potential model could be used to fit the values of Henry's Law constants but for C_2H_2 no fit could be found with reasonable parameters. An explanation for this was given in terms of image forces, but quantitative estimates of the image force resulted in the molecule being pushed so close to the surface as to touch its own image. The theory used in these calculations employed an image plane raised above the surface (defined by the nuclear centres) by 1.7 Å. It was the position of this plane which caused the catastrophe. The concept of an image plane can be used at large distances but close to the surface it is perhaps better to consider the interaction as an electrostatic induction interaction between parts of the molecule and the corrugated surface. One could then include the anisotropic polarizability of the surface which cannot be done in an image plane model. Calculations of this nature are underway and considerable improvement has been found but these calculations are much more expensive in terms of computer time.

Simulations of the order-disorder transition in N_2 adsorbed on graphite were found to be in agreement with the x-ray experiments. The broadening of the transition was found to be caused by the formation of isolated pinwheel structures. Because this transition (at higher densities) is accompanied by an increase in the lattice parameter, it would be better to use a constant pressure simulation technique rather than the constant area method used here.

In the case of CO adsorbed on graphite the agreement was not as good. The molecule-molecule potential employed seemed to correspond to a molecule which was too small. The zero pressure monolayer density was 9% too large when compared to experiment. More work is needed to properly describe the CO molecule-molecule potential.

REFERENCES

1. Phase Transitions in Surface Films, Ed. J.G. Dash and J. Ruvald, Plenum Press, New York, 1979; Films on Solid Surfaces, J.G. Dash, Academic Press, New York, 1975.
2. Acetylene, its Properties, Manufacture and Uses, S.A. Miller, Academic Press, New York, 1965.
3. Spectra of Diatomic Molecules, G. Herzberg, van Nostrand, New York, 1950.
4. T.A. Scott, Phys. Rep., 27C (1976) 89.
5. R.D. Amos and J.H. Williams, Chem. Phys. Lett., 66 (1979) 471.
6. S.F. [illegible]'Shea, unpublished (1983).
7. A.D. Buckingham, R.L. Disch and D.A. Dunmur, J. Am. Chem. Soc., 90 (1968) 3104.
8. F.M. Mulder, G. Van Dijk and A. van der Avoird, Mol. Phys., 39 (1980) 407.
9. Molecular Theory of Gases and Liquids, J.O. Hirschfelder, C.F. Curtis and R.B. Bird, Wiley, New York, 1954.
10. H.K. Koski and E. Sandor, Acta. Cryst. B31 (1975) 350.
11. I.N. Krupskii, A.I. Prokhvatilov, A.I. Ehrenburg and L.D. Yantsevich Phys. Stat. Sol (a), 19 (1973) 519.
12. A.F. Schuch and R.L. Mills, J. Chem. Phys., 52 (1970) 6000.
13. G.J.H. van Nes, Doctoral Thesis, University of Groningen (1978).
14. J.O. Clayton and W.F. Giauque, J. Am. Chem. Soc., 54 (1932) 2610.
15. G. Filippini, C.M. Gramacciolo and M. Simonetta, J. Chem. Phys., 73 (1980) 1376.
16. Z. Gamba and H. Bonadeo, J. Chem. Phys., 76 (1982) 6215.

17. F.L. Hirshfeld and K. Mirsky, Acta. Cryst., A35 (1979) 366.

18. T. Aoyama, O. Matsuoka and N. Nakagawa, Chem. Phys. Lett., 67 (1979) 508.

19. J. Menaucourt, A. Thomy and X. Duval, J. Chem. Phys., 77 (1980) 959.

20. P. Thorel, C. Marti, G. Bomchil and J.M. Alloneau, Suppl. de Le Vide, Les Couches Minces, 201, vol. I, (1980) 119.

21. E.K. Gill and J.A. Morrison, J. Chem. Phys., 45 (1966) 1585.
J.C. Burford and G.M. Graham, Can. J. Phys., 47 (1969) 23.
T. Atake, H. Suga and H. Chihara, Chem. Lett., (1976) 567.

22. J. Walton, J. Brookman and A. Rigamonti, Phys. Rev., B28 (1983) 4050.

23. K. Morishigé, C. Mowforth and R.K. Thomas, Surf. Sci. in press (1984).

24. H. You and S.C. Fain Jr., Surf. Sci. in press (1984).

25. B. Genot, J. Chem. Phys., 67 (1970) 1320.

26. I. Yasumoto, J. Phys. Chem., 84 (1980) 589.

27. A. Terlain and Y. Larher, Surf. Sci., 125 (1983) 304.

28. A. Terlain and Y. Larher, Surf. Sci., 93 (1980) 64.

29. J.H. Quateman and M. Bretz, Phys. Rev. B 29, (1984) 1159.

30. H.K. Kim and M.H.W. Chan, Phys. Rev. Lett., 53 (1984) 170.

31. Ordering in Two Dimensions, R.J. Birgeneau, E.M. Hammons, P. Heiney, P.W. Stephen and P.M. Ham, ED. S.K. Sinha, North-Holland, p. 29 (1980).

32. M.D. Chinn and S.C. Fain Jr., Phys. Rev. Lett., 39 (1977) 146.

33. J. Piper, J.A. Morrison, C. Peters and Y. Ozaki, J. Chem. Soc. Faraday Trans. 1, 79 (1983) 2863.

34. J. Piper, J.A. Morrison and C. Peters, Mol. Phys., in press (1984).

35. Theory of Intermolecular Forces, H. Margenau and N.R. Kestner, Pergamon Press, 1969.

36. Rare Gas Solids, eds. M.L. Klein and J.A. Venables, Academic Press, New York, 1976.

37. J.C. Raich, A.B. Anderson and W. England, J. Chem. Phys., 64 (1976) 5088.

38. R.M. Berns and A. van der Avoird, J. Chem. Phys., 72 (1980) 6107.

39. F. Mulder, G.F. Thomas and W.J. Meath, Mol. Phys., 41 (1980) 249.

40. F. Mulder, G. Van Dijk and A. van der Avoird, Mol. Phys., 39 (1980) 407.

41. G.D. Zeiss and W.J. Meath, Mol. Phys., 33 (1977) 1155.

42. M.S.H. Ling and M. Rigby, Mol. Phys., 51 (1984) 855.

43. D.E. Williams, J. Chem. Phys., 47 (1967) 4680, Acta Cryst., A30 (1974) 71.

44. A.I. Kitaigorodskii, Molecular Crystals and Molecules, Academic Press, New York (1973).

45. K.V. Mirshaya, Tetrahedron, 29 (1973) 679.

46. R.J. Bell, J. Phys., B3 (1970) 751.

47. B.M. Axilrod and E. Teller, J. Chem. Phys., 11 (1943) 299.

48. M.L. Klein, Y. Osaki and S.F. O'Shea, J. Phys. Chem., 88 (1984) 1420.

49. O. Sinanoglu and K.S. Pitzer, J. Chem. Phys., 32 (1960) 1279.

50. A.D. McLachlan, Mol. Phys., 7 (1964) 381.

51. E. Zaremba and W. Kohn, Phys. Rev., B13 (1976) 2270.

52. S. Rauber, J.R. Klein, M.W. Cole and L.W. Bruch, Surf. Sci., 123 (1982) 173.

53. G. Vidali and M.W. Cole, Surf. Sci., 110 (1981) 10.
54. E.M. Lifshitz, Sov. Phys. JETP, 2 (1956) 73.
55. W.A. Steele, J. de Phys., Coll., C4, (1977) 61.
56. L.W. Bruch, J. Chem. Phys., 79 (1983) 3148.
57. C.S. Murthy, K. Singer, M.L. Klein and I.R. McDonald, Mol. Phys., 41 (1980) 1387.
58. T. Luty and G.S. Pawley, Chem. Phys. Lett., 28 (1974) 593.
59. T. Luty, A. van der Avoird and R.M. Berns, J. Chem. Phys. 73 (1980) 5305; B. Kutchta and T. Luty, J. Chem. Phys., 78 (1983) 1447.
60. K. Mirsky, Acta Cryst., A32 (1976) 199.
61. G. Taddei, R. Righini and P. Manzelli, Acta Cryst., B33 (1977) 626.
62. A.D. Crowell, J. Chem. Phys., 29 (1958) 446.
63. G. Zumafen and K. Dressler, J. Chem. Phys., 64 (1976) 5198.
64. Pier Francessco Fracassi and M.L. Klein, Chem. Phys. Lett., 108 (1984) 359.
65. K. Mirsky, Chem. Phys., 46 (1980) 445.
66. A.I. Kitaigorodskii, K.V. Mirskaya and V.V. Nauchitel, Sov. Phys. Cryst., 14 (1970) 769.
67. B.L. Jhanwar and M.J. Meath, Chem. Phys., 67 (1982) 185.
68. R.D. Amos, Chem. Phys. Lett., 70 (1980) 613.
69. P.S.Y. Cheung and J.G. Powles, Mol. Phys., 32 (1976) 1383.
70. B.O. Hall and H.M. James, Phys. Rev., B13 (1976) 3590.
71. Statistical Mechanics A, ED. B.J. Berne, Plenum Press, New York.
72. Monte Carlo Methods in Statistical Physics, ED. K. Binder, Springer-Verlag, New York, 1979.
73. N. Metropolis, A.W. Metropolis, M.N. Rosenbluth, A.H. Teller and E. Teller, J. Chem. Phys., 21 (1953) 1079.

74. F.E. Abraham, W.E. Rudge, D.J. Auerbach and S.W. Koch, Phys. Rev. Lett., 52 (1984) 445.

75. S. Goldman, J. Chem. Phys., 79 (1983) 3989.

76. K.C. Ng, W.J. Meath and A.R. Allnat, Mol. Phys. 33 (1977) 699.

77. A.B. Harris and A.J. Berlinsky, Can. J. Phys., 57 (1979) 1852.

78. R.D. Diehl and S.C. Fain Jr., Surf. Sci., 125 (1983) 116.

79. A.D. Migone, H.K. Kim, M.H.W. Chan, J. Talbot, D.J. Tildesley, and W.A. Steele, Phys. Rev. Lett., 51 (1983) 192.

80. S.F. O'Shea and M.L. Klein, Chem. Phys. Lett., 66 (1979) 381.

81. O.G. Mouritsen and A.J. Berlinsky, Phys. Rev. Lett., 48 (1982) 181.

82. J. Talbot, D.J. Tildesley and W.A. Steele, Mol. Phys., 51 (1984) 1381.

83. R.D. Diehl and S.C. Fain Jr., Phys. Rev. B, 26 (1982) 4785.

84. A.V. Kiselev and D.P. Poshkus, J. Chem. Soc. Far. II, 72 (1976) 950.

85. J. Piper and J.A. Morrison, Phys. Rev., B30 (1984) 3486.

86. B. Joos, B. Bergersen and M.L. Klein, Phys. Rev., B28 (1983) 7219.

87. A.J. Stone, unpublished.

88. K. Sakai, A. Koide and T. Kihara, Chem. Phys. Lett., 47 (1977) 416.